

Magnetohydrodynamic duct and channel flows at finite magnetic Reynolds numbers

Dissertation

zur Erlangung des akademischen Grades

Doktoringenieur

(Dr.-Ing.)

vorgelegt der

Fakultät für Maschinenbau der
Technischen Universität Ilmenau

von Herrn

M.Tech. Vinodh Kumar Bandaru

geboren am 15.01.1984 in Sriharikota, Indien

Tag der Einreichung: 27.11.2015

Datum der wissenschaftlichen Aussprache: 23.02.2016

Gutachter: 1. Priv.-Doz. Dr. Thomas Boeck
 2. Univ.-Prof. Dr.-Ing. Claus Wagner
 3. Prof. Bernard Knaepen

Abstract

Magnetohydrodynamic duct flows have so far been studied only in the limit of negligible magnetic Reynolds numbers (R_m). When R_m is finite, the secondary magnetic field becomes significant, leading to a fully coupled evolution of the magnetic field and the conducting flow. Characterization of such flows is essential in understanding wall-bounded magnetohydrodynamic turbulence at finite R_m as well as in industrial applications like the design of electromagnetic pumps and measurement of transient flows using techniques such as Lorentz force velocimetry. This thesis presents the development of a numerical framework for direct numerical simulations (DNS) of magnetohydrodynamic flows in straight rectangular ducts at finite R_m , which is subsequently used to study three specific problems.

The thesis opens with a brief overview of MHD and a review of the existing state of art in duct and channel MHD flows. This is followed by a description of the physical model governing the problem of MHD duct flow with insulating walls and stream-wise periodicity. In the main part of the thesis, a hybrid finite difference-boundary element computational procedure is developed that is used to solve the magnetic induction equation with boundary conditions that satisfy interior-exterior matching of the magnetic field at the domain wall boundaries. The numerical procedure is implemented into a code and a detailed verification of the same is performed in the limit of low R_m by comparing with the results obtained using a quasistatic approach that has no coupling with the exterior.

Following this, the effect of R_m on the transient response of Lorentz force is studied using the problem of a strongly accelerated solid conducting bar in the presence of an imposed localized magnetic field. The response time of Lorentz force depends linearly on R_m and shows a good agreement with the existing experiments. For sufficiently large values of R_m , the peak Lorentz force is found to show an R_m^{-1} dependence.

After this, the phenomenon of dynamic runaway due to magnetic flux expulsion in a two-dimensional channel flow is studied. Comparison with an existing one-dimensional model shows a close agreement for the Hartmann regime and the bifurcation location but the model overpredicts the core velocities in the Poiseuille regime significantly. Parametric studies indicate the importance of the streamwise wavenumber of the imposed magnetic field on the bifurcation point.

Finally, turbulent Hartmann duct flow is investigated at moderate values of R_m . A higher R_m is found to delay the onset of relaminarization to a higher value of Hartmann number. Large scale turbulence is induced at moderate R_m and the effect increases with R_m . Between the core and the Shercliff layers, Reynolds stresses decrease with increase in R_m , leading to larger mean velocities in that region.

Zusammenfassung

Magneto hydrodynamische Kanalströmungen (MHD-KS) wurden bisher nur bei vernachlässigbar kleiner magnetischer Reynoldszahl R_m untersucht. Bei endlichem R_m wird das sekundäre Magnetfeld signifikant, was zu einer gekoppelten Entwicklung von Magnetfeld und leitfähiger Strömung führt. Die Charakterisierung solcher Strömungen ist essentiell für das Verständnis von wandbegrenzter MHD-Turbulenz und in Anwendungen wie z.B. elektromagnetischen Pumpen und der induktiven Strömungsmessung. Die Dissertation stellt ein Verfahren für die direkte numerische Simulation (DNS) von MHD-KS bei endlichem R_m vor, welches dann auf drei Probleme angewendet wird.

Am Anfang der Arbeit steht eine kurze Übersicht zur MHD und zum Stand des Wissens zu MHD-KS. Danach folgt eine Beschreibung des physikalischen Modells für die MHD-KS mit elektrisch isolierenden Wänden. Im Hauptteil der Arbeit wird ein hybrides Berechnungsverfahren entwickelt und implementiert, das auf finiten Differenzen sowie dem Randintegralverfahren basiert. Es dient zur Lösung der Induktionsgleichung mit Randbedingungen, die für einen stetigen Anschluss des Magnetfelds auf den Gebietsrändern zwischen Innen- und Außenraum sorgen. Eine detaillierte Verifikation des Codes wird durch Vergleich mit der quasistatischen Näherung vorgenommen.

Anschliessend wird das Zeitverhalten der Lorentzkraft bei beschleunigter Bewegung einer leitfähigen rechteckigen Stange in einem lokalisierten Magnetfeld untersucht. Die Zeitantwort der Lorentzkraft hängt linear von R_m ab und stimmt gut mit Experimenten überein. Für große R_m sind die Maximalwerte der Lorentzkraft umgekehrt proportional zu R_m .

Im weiteren wird das dynamische "Weglaufen" der Geschwindigkeit infolge von magnetischer Flussverdrängung in einer zweidimensionalen MHD-KS untersucht. Der Vergleich mit einem eindimensionalen Modell zeigt eine gute Übereinstimmung für das sogenannte Hartmann-Regime und den Bifurkationspunkt zum sogenannten Poiseuille-Regime, bei dem allerdings die Geschwindigkeit vom Modell überschätzt wird. Die Wellenlänge des Magnetfelds ist für den Bifurkationspunkt entscheidend.

Abschliessend wird die turbulente Hartmannströmung untersucht. Bei endlichem R_m verschiebt sich die Relaminarisierung zu größeren Hartmannzahlen und es wird großskalige Turbulenz angeregt. Zwischen den Shercliff-Schichten und dem Strömungskern verringern sich die Reynoldsspannungen mit steigendem R_m , was zu höherer mittlerer Geschwindigkeit und flacheren Geschwindigkeitsprofilen führt.

Contents

Abstract	i
Zusammenfassung	iii
Contents	v
1 Introduction	1
1.1 Magnetohydrodynamics - a brief overview	1
1.2 Magnetohydrodynamic flow in ducts and channels - state of the art . .	3
1.3 Scope of the thesis	5
2 Mathematical model	7
2.1 The MHD approximation	7
2.2 Physical model and governing equations	10
2.3 Jump conditions at the wall boundaries	12
2.4 The quasistatic approximation - a brief note	14
3 Numerical procedure	15
3.1 The problem of magnetic boundary conditions	15
3.2 Numerical procedure	17
3.2.1 The interior problem	17
3.2.2 Boundary integral equation and the coupled numerical procedure	20
3.2.3 Treatment of the zero mode ($k = 0$)	29
3.3 Verification and comparative study	31
3.3.1 Verification of BEM implementation with analytical solution .	31
3.3.2 Convergence of the coupled FD-BEM iterative procedure . . .	32
3.3.3 Verification in the limiting case of low R_m	34
3.3.4 Comparison with pseudo-vacuum boundary conditions	39
3.4 Explicit procedure for the induction equation	40
3.5 Permeation of an exterior magnetic field into a conductor - finite R_m effects	42
3.5.1 Pure diffusion into a stationary conducting bar	42
3.5.2 Simultaneous advection-diffusion in a laminar duct flow . . .	44
4 Transient response of Lorentz force at finite magnetic Reynolds numbers	49
4.1 Overview and problem setup	49
4.2 Physical model	50

CONTENTS

4.2.1	Magnetic field of the Halbach array	51
4.3	Results and comparison with experiments	55
5	Magnetic flux expulsion and bifurcations in a plane channel flow	61
5.1	Introduction	61
5.2	Problem setup and governing equations	62
5.2.1	Problem formulation and full governing equations	62
5.2.2	Numerical Procedure	65
5.2.3	One-dimensional approximate model of Kamkar and Moffatt (KM82)	66
5.3	Results and comparison	67
5.3.1	Hartmann regime	68
5.3.2	Poiseuille regime	69
5.3.3	Comparison with the predictions of KM82	74
5.3.4	Effect of parameters ε , β and κ	76
6	Turbulence in Hartmann duct flow at low and moderate Reynolds numbers	81
6.1	Turbulence at low Reynolds number	81
6.1.1	Relaminarization threshold	82
6.1.2	Turbulence at lower Hartmann number	83
6.2	Turbulence at moderate Reynolds number	86
6.2.1	Parameters and grid sensitivity	87
6.2.2	Flow structure at different values of R_m	88
6.2.3	Integral characteristics	89
6.2.4	Mean flow quantities, Reynolds stresses and turbulence intensities	92
6.2.5	Anisotropy	94
7	Summary and Outlook	97
A	Uniqueness of the current density field when $j_n = 0$	101
B	Effective wavenumbers for Fast Fourier transformation	103
C	Sensitivity of Lorentz force time response	105
	Author Publications	107
	References	109
	Erklärung	117
	Acknowledgements	119

Chapter 1

Introduction

1.1 Magnetohydrodynamics - a brief overview

Magnetohydrodynamics (MHD) is the theory of the macroscopic interaction between magnetic fields and the flow of electrically conducting non-magnetic fluids. Fluids that come under the ambit of this definition fall broadly into the category of liquid metals, electrolytes and plasmas. The field of MHD concerns a wide range of applications ranging from astro- and geophysical phenomena to the manipulation and control of liquid metal flows in the metallurgical industry. The subject is not of a recent origin but rather considered to have gained momentum during the 1930s and 40s, although sporadic ideas and contributions occurred right from the days of Michael Faraday. Of important mention concerning early work are the 1832 experiment of William Ritchie in which he could propel a fluid into motion electromagnetically (Ritchie [1832]) and Faraday's speculation attributing the frequent changes in earth's magnetic field to ocean currents. From these modest beginnings, MHD has come a long way in the last 180 years.

That MHD was relevant in the astrophysical context was apparent only by the early 20th century, when it was realized that plasmas and magnetic fields were ubiquitous in the cosmos, which was first suggested by Kristian Birkeland (it is now estimated that about 99% of the known universe is plasma). Subsequently in 1919, Larmor proposed that the sun's magnetic field was the result of a dynamo action (Larmor [1919]), followed later by the discovery of Alfvén waves in 1942 which was a significant milestone (Alfvén [1942]). Today, after decades of continued research, significant progress has been made in our understanding of MHD phenomena in nature. It is now fairly well established that magnetohydrodynamic interactions are primarily responsible for the formation of stars from interstellar matter, for the generation and sustenance of magnetic fields of the sun, the earth and other planets by the dynamo action, and for

phenomena such as sunspots and solar flares, to name a few. Yet, a number of open questions continue to remain and are a subject of ongoing research. For example, the exact details of the mechanism of geodynamo have some missing links till date.

On the other hand, industrial/engineering applications of MHD began rather late only by around the 1960s. It started due to the need to pump liquid Sodium that was used as a coolant in fast breeder reactors and to enable confining plasma (stably) which was necessary to perform controlled thermonuclear fusion for power generation. Subsequently, the metallurgical industry is considered to have been through a ‘boom’ period in the 1970s, driven by economic factors. During this period, many traditional processes related to metal casting were revisited and were modified/replaced in ways that involved utilizing magnetic fields in order to improve process efficiency and product quality. Continuous casting of steel also started during the same time. As a result, pumping of liquid metal using electromagnetic pumps, stirring of molten metal using rotating magnetic fields during the casting process to obtain better and homogenous ingots, damping of molten metal flow using static magnetic fields to prevent surface contamination occurring due to entrainment, and magnetic levitation to melt highly reactive metals like Titanium, have become some of the common processes in the metallurgical industry that take advantage of magnetohydrodynamic phenomena. Controlled silicon crystal growth using magnetic fields (see e.g. Langlois [1985]) and non-intrusive flow measurement techniques are a few more applications of recent interest. Currently, the engineering applications of MHD are myriad and it is possible to mention only a few important ones here for reasons of brevity. A detailed overview of the industrial applications of MHD and the physics involved in some of the processes can be found in Davidson [1999] and Davidson [2001] .

It is already easy to see that magnetohydrodynamic flows span a wide spectrum and in general, it is useful to broadly distinguish them on the basis of a non-dimensional parameter, the magnetic Reynolds number defined as

$$R_m = \frac{UL}{\lambda}, \quad (1.1)$$

where U and L are the characteristic velocity and length scales in the flow and λ is the magnetic diffusivity of the fluid given by $\lambda = (\mu_0\sigma)^{-1}$, μ_0 and σ being the magnetic permeability of free space and the electrical conductivity of the fluid respectively. R_m is a measure of the relative magnitude of advection to the diffusion of magnetic field in the flow. Astrophysical MHD and the geodynamo fall into the category of advection dominated high R_m flows ($R_m \gg 1$) whereas most industrial and laboratory flows involve moderate to low magnetic Reynolds numbers.

The focus of this work is on MHD flows in duct and channel geometries at finite

R_m . A detailed background and motivation for the same will follow next.

1.2 Magnetohydrodynamic flow in ducts and channels - state of the art

The study of MHD flows in rectangular ducts and channels have been of significant interest during the last 80 years. Due to their potential applicability in liquid metal cooling blankets in fusion reactors, these flow continue to attract a lot of scientific research even today. The study of such flows started with the first mercury flow experiments by Hartmann and Lazarus in 1937 in ducts and pipes with an imposed wall normal magnetic field (Hartmann & Lazarus [1937]). These experiments were performed at rather low flow Reynolds numbers $Re < 5000$ ($Re = UL/\nu$, ν being the kinematic viscosity of the fluid) but yielded some important results. It was observed through the measurements of pressure loss that the imposition of magnetic field lead to the formation of very thin velocity boundary layers at the two walls perpendicular to the magnetic field (which are now known as Hartmann layers) with relatively flat velocity profile away from these walls and the suppression of turbulence (partly/wholly) if any was present. It was also shown that the pressure drop initially decreases with increase in magnetic field and then increases when the flow has laminarized. This was attributed to the combined effect of the two independent effects of turbulence suppression and Hartmann flattening.

Very few experiments were conducted in the next few decades with continued focus on the effect of magnetic field on the flow pressure drop and to identify the critical parameter space at which turbulence-laminar transition occurred. Notable are Murgatroyd's experiments on mercury flows at $Re \sim 10^5$ in a duct with 15:1 aspect ratio which can be considered as a channel. He found that the skin friction factor was an increasing function of $R = Re/Ha$, the Reynolds number based on the Hartmann layer thickness and that the laminar-turbulence transition occurred at $R \approx 225$ (Murgatroyd [1953]). Brouillette & Lykoudis [1967] confirmed these results and in addition noted that in the turbulent regime, the flattening effect at the Hartmann walls is more pronounced than the turbulence suppression effect, due to which the skin-friction increases with R . Meanwhile, several analytical studies were carried out on steady laminar Hartmann duct flows (see e.g. Shercliff [1953], Williams [1963] and Hunt [1965]). Boundary layers on the walls parallel to the magnetic field were identified (now known as Shercliff layers or side layers) that were quite different from the Hartmann layers and the effect of insulating/perfectly conducting wall boundary conditions on the flow profiles were understood.

Measurements of turbulent fluctuations in shear flow MHD started only in the 1970s, with pipe flow experiments of Gardner & Lykoudis [1971] and studies of channel flow by Reed & Lykoudis [1978]. By this time, it was clear that turbulent fluctuations in the side layers are the last to get suppressed due to the magnetic field whereas they are strongly suppressed in the core/middle region. Furthermore, the magnetic field suppressed the Reynolds stress more effectively than the individual fluctuations contributing to the stress. Although direct numerical simulations (DNS) of MHD turbulence in 3D periodic boxes started already by this time (see e.g. Schumann [1976]), such simulations of MHD duct/channel flows started only in the nineties. These studies were motivated by the idea that near-wall streamwise vortices that are considered to be the reason for high Reynolds stresses, could be inhibited by a magnetic field applied either in the streamwise or spanwise direction (Crawford & Karniadakis [1997], Lim *et al.* [1998]). Since then, a number of DNS studies have been conducted mostly in channel geometries (e.g. Lee & Choi [2001], Boeck *et al.* [2007], Krasnov *et al.* [2008]) and a lot has been unravelled on the structure of turbulence and the stability of the boundary layers. However, very few DNS studies exist for MHD duct flows, infact the only ones being Kobayashi [2008], Chaudhary *et al.* [2010], Shatrov & Gerbeth [2010], and Krasnov *et al.* [2013]. All these studies have been performed in the low R_m limit. There exists no study of MHD duct flows in the case when R_m becomes finite and the effect of magnetic field on turbulence in such a scenario is unknown. This is the primary motivation of the present work.

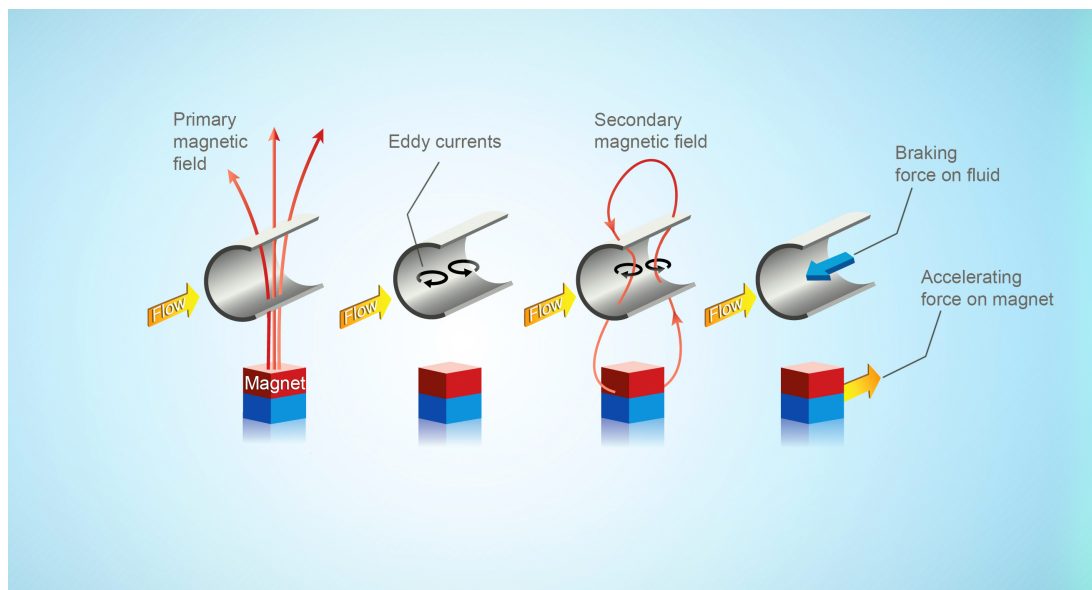


Figure 1.1: Schematic showing the principle of Lorentz Force Velocimetry (LFV).

As mentioned earlier, there exist contactless flow measurement techniques, which have gained attention in the past decade. The need for these arise from the fact that

optical methods are unsuitable for flows involving liquid metals due to their opacity, whereas traditional flow measuring probes cannot withstand the environment of hot and chemically aggressive melts. Some of such recent measurement methods that are promising are the contactless inductive flow tomography (CIFT) (Stefani *et al.* [2004]), Lorentz force velocimetry (LFV) (Thess *et al.* [2006]) and the rotary flow meter (Pride *et al.* [2011]). Although each of these techniques have their own pros and cons, here we limit our scope only to LFV, the fundamental principle of which is to reconstruct velocity fields in conducting flows by measuring the Lorentz force that acts on a permanent magnet (or magnet systems) placed in the vicinity of the flow (see Fig. 1.1). For quite some time, this technique has been mostly limited to measuring integral quantities like volume flow rates in channels, but has recently been shown to be feasible for local single-component velocity measurements (Heinicke [2013]). Today, three-dimensional velocity vectors fields are already being mapped, with the use of high precision multi-component force and torque sensors (Hernández *et al.* [2015]). However, currently it is only possible to measure steady flows through LFV. This is because, in a strongly transient flow, the magnetic Reynolds number becomes finite, as a consequence of which, the Lorentz force will no more be a linear function of the velocity and an additional time lag will occur between the flow velocity and the measured force signal. Such a behavior is currently not well understood as there exist no studies that quantify the response of Lorentz force to time-varying/finite R_m flows. This is the second motivating factor for the present work. We now move on to define the scope of the present work and the questions that it intends to answer.

1.3 Scope of the thesis

The aim of the present work is to develop a numerical framework to perform direct numerical simulations (DNS) and study magnetohydrodynamic flows in straight rectangular ducts and channels at finite magnetic Reynolds numbers. As mentioned in the previous section, this has never been attempted before, primarily due to the complexities involved in incorporating the non-trivial magnetic boundary conditions that arise at finite R_m . Numerical procedures and the corresponding code are developed for this purpose on the basis of an existing DNS code that uses the low R_m approximation. The code is used to study three specific finite R_m MHD problems, namely, a) Lorentz force response in a solid conducting bar strongly accelerating in the presence of a localized magnetic field, b) the phenomenon of dynamic runaway in MHD channel flow, and c) turbulent Hartmann duct flow at moderate R_m . Wherever necessary, the code is customized to the needs of the specific problem being studied. The work aims to answer

the following general questions

1. Is it feasible to perform DNS of magnetohydrodynamic duct flow at finite R_m with fully consistent treatment of the exterior magnetic field ? If so, what numerical procedures are best suited ? How good are the often used pseudo-vacuum magnetic boundary conditions ?
2. What is the response of the integral Lorentz force in LFV, when R_m becomes finite due to strongly transient motions. How does the time delay between the velocity and Lorentz force depend on R_m ?
3. What is the nature of flux expulsion and the associated bifurcations that occur in an MHD channel flow ? How do they depend on the hydrodynamic and magnetic Reynolds numbers ?
4. Are the statistically steady states of Hartmann duct flow very different at finite R_m as compared to the case of low R_m ? What kind of fundamental differences arise in the structure of the flow ?

The thesis is structured as follows. In the next chapter, we describe the physical model that governs the problem being considered. In chapter 3, we develop the computational procedures necessary for the solution of the full set of governing equations. In chapter 3 we also present detailed studies of verification of the numerical implementation and the study of how an external magnetic field permeates into a conducting medium that is either stationary or in a state of laminar flow. Later on, in chapter 4, the study of Lorentz force transient response at finite R_m is presented, in the context of an accelerating solid bar. This is followed by the study of magnetic flux expulsion and runaway in MHD channel flow, in chapter 5. After that, we take up the study of turbulent Hartmann duct flow at moderate magnetic Reynolds numbers in chapter 6. Finally, in chapter 7, the conclusions arising out of the present work are summarized with a brief outlook towards future work.

Chapter 2

Mathematical model

2.1 The MHD approximation

As mentioned earlier, the theory of magnetohydrodynamics is a subdiscipline of plasma physics and is related to it in the same way as classical hydrodynamics is related to the kinetic theory of fluids. It is a macroscopic theory and hence all field variables including charge distributions are described as spatially continuous. Due to this, some of the fundamental equations of electromagnetism applicable for single charges cannot be used as it is in the context of MHD and hence suitable continuum forms of the equations must be obtained. Several facts and assumptions are taken into account in doing this. The aim of this section is to briefly describe how, starting from the basic laws, the particular forms of the electrodynamic equations that govern MHD are obtained. It must be mentioned at the outset that the description given in this section is standard and is provided here for the sake of completeness. A comprehensive discussion of the same can be found in Shercliff [1965].

The force on a single charged particle i of charge q_i and moving with a velocity U_i in an environment with electric field E and magnetic flux density B_t is given by

$$f_i = q_i(E + U_i \times B_t) \quad (2.1)$$

and this force is known as Lorentz force in electromagnetism. The force on a unit volume containing such charged particles will be

$$f = \sum_{i=1}^{i=N} q_i E + \left(\sum_{i=1}^{i=N} q_i U_i \right) \times B_t = qE + J \times B_t, \quad (2.2)$$

where the summation is over all the charged particles N in the volume, q is the charge/unit volume and J is the electric current density. Now, the relative magnitudes of the

2. Mathematical model

two terms in the above equation can be estimated using a scaling argument with typical scales for the length, velocity and magnetic field as d , v and B respectively. From Gauss' law $\nabla \cdot \mathbf{E} = q/\epsilon_0$ and on the assumption that $E \sim vB$, one can see that $qE \sim \epsilon_0 B^2 v^2/d$, where ϵ_0 is the permittivity of free space. Furthermore, from Ampere's law, the current density can be taken to scale as $J \sim B/\mu d$, where μ is the permeability of the medium. It now follows that the ratio $qE/J \times \mathbf{B}_t \sim (\epsilon_0 B^2 v^2/d) (B^2/\mu d)^{-1} \sim v^2/c^2$, c being the speed of light in vacuum. Hence, the force is assumed to be comprised of only the magnetic part as

$$\mathbf{f} = \mathbf{J} \times \mathbf{B}_t, \quad (2.3)$$

which is customarily called as Lorentz force in MHD.

We now consider an electrical conductor (but non-magnetic) moving with a velocity \mathbf{V} , with free charges moving with a velocity \mathbf{U}_c relative to the conductor under the influence of an electric field \mathbf{E} and a magnetic field \mathbf{B}_t . In this case, one can assume that the inertia of the free charges are negligible. This means that irrespective of whether a free charge accelerates or not, the net force on the particle must vanish. The theory of electrical resistivity suggests that the electric forces are balanced by dissipative forces that are proportional to the velocity of the charge as

$$q_{c,i} [\mathbf{E} + (\mathbf{U}_{c,i} + \mathbf{V}) \times \mathbf{B}_t] = \kappa_{c,i} \mathbf{U}_{c,i}, \quad (2.4)$$

where the proportionality constant κ_i is specific to the particular free charge $q_{c,i}$. Again, adding these terms over a small element yields

$$q_c \mathbf{E} + \mathbf{J}_c \times \mathbf{B}_t + q_c \mathbf{V} \times \mathbf{B}_t = \sum \kappa_{c,i} \mathbf{U}_{c,i} \quad (2.5)$$

on a per unit volume basis. Here q_c is the charge/unit volume contributed by the free charges and $\mathbf{J}_c = \sum q_{c,i} \mathbf{U}_{c,i}$ is known as the conduction current. Furthermore, it is well known that the quantity $\sum_i (\kappa_{c,i} \mathbf{U}_{c,i})/q_c$ is proportional to the conduction current as $\sum_i (\kappa_i \mathbf{U}_i)/q_c = \mathbf{J}_c/\sigma$, σ being the electrical conductivity of the material. Using this, we obtain

$$\mathbf{E} + \frac{\mathbf{J}_c \times \mathbf{B}_t}{q_c} + \mathbf{V} \times \mathbf{B}_t = \frac{\mathbf{J}_c}{\sigma}. \quad (2.6)$$

At this juncture, a number of simplifications are made. At first, the second term of (2.6) known as the Hall effect, is neglected in the low-frequency approximation which is relevant for MHD (this is essentially due to the fact that q_c is relatively large due to

the large number density of free electrons in solid or liquid conductors). Furthermore, the total current density \mathbf{J} due to the motion of all kinds of charges (free and bound) can be expressed as

$$\mathbf{J} = q\mathbf{V} + \sum_{i=1}^{i=N} q_i \mathbf{U}_i = q\mathbf{V} + \sum_{i=1}^{i=N_b} q_{b,i} \mathbf{U}_{b,i} + \sum_{i=1}^{i=N_c} q_{c,i} \mathbf{U}_{c,i} = q\mathbf{V} + \frac{\partial P}{\partial t} + \mathbf{J}_c, \quad (2.7)$$

where the subscripts b and c represent bound and free charges respectively. The first and second terms on the right hand side represent convection and polarization currents respectively (P is the polarization density and the subscript b represents bound charges). The polarization current is due to the changing of the state of polarization (or separation) of charges within the molecules that comprise the conductor. It is interesting to note that the total charge density $q \sim \epsilon_0 \nabla \cdot \mathbf{E}$ and hence the ratio of convection current to the total current is $q\mathbf{V}/\mathbf{J} \sim (\epsilon_0 B v^2/d) (B/\mu d)^{-1} \sim v^2/c^2$ which is negligible. Further, the polarization current $\partial P/\partial t \sim \epsilon_0 \partial \mathbf{E}/\partial t$ is small compared to \mathbf{J} and is neglected. Hence, the total current density \mathbf{J} in MHD is taken to be equal to the conduction current density \mathbf{J}_c . Using these simplifications, (2.6) becomes

$$\mathbf{J} = \sigma (\mathbf{E} + \mathbf{V} \times \mathbf{B}_t), \quad (2.8)$$

which is essentially an equation of force balance on free charges and is known as Ohm's law in the context of continuous charge distributions (and in MHD as well).

Finally, we also see that neglecting the term $\epsilon_0 \partial \mathbf{E}/\partial t$ leads to simplified forms of the Ampère's law and Kirchoff's law as

$$\mu \mathbf{J} = \nabla \times \mathbf{B}_t, \quad (2.9)$$

$$\nabla \cdot \mathbf{J} = 0. \quad (2.10)$$

The Faraday's law retains its form and reads as

$$\frac{\partial \mathbf{B}_t}{\partial t} = -\nabla \times \mathbf{E}. \quad (2.11)$$

Equations (2.3), (2.8), (2.9), (2.10) and (2.11) represents the fundamental forms of electromagnetic laws as relevant to the study of magnetohydrodynamics. We now move on to describe the complete physical model that describes the main prototype problem that we are concerned with in this thesis, namely the MHD periodic duct flow.

2.2 Physical model and governing equations

We consider the flow of an incompressible and electrically conducting fluid (e.g., liquid metal or plasma) that is driven by a mean streamwise pressure gradient along a straight rectangular duct and is subjected to an externally imposed magnetic field $\mathbf{B}_0(\mathbf{x}, t)$ (see Fig. 2.1). The flow with a velocity field $\mathbf{V}(\mathbf{x}, t)$ crossing the imposed magnetic field lines induces eddy currents $\mathbf{J}(\mathbf{x}, t)$ in the fluid, which in turn produce a secondary (or induced) magnetic field $\mathbf{B}(\mathbf{x}, t)$. The resultant total magnetic field

$$\mathbf{B}_t = \mathbf{B}_0 + \mathbf{B} \quad (2.12)$$

interacts with the eddy currents to produce a Lorentz force that is proportional to $\mathbf{J} \times \mathbf{B}_t$ which affects the flow field. We are interested in the computation of the velocity and the magnetic fields in the interior of the duct through DNS. This means that the smallest scales, the Kolmogorov length and magnetic diffusion scales are resolved. Further, the mass flux through the duct is assumed to be constant and the direction along the mean flow - the streamwise direction - is assumed to be periodic.

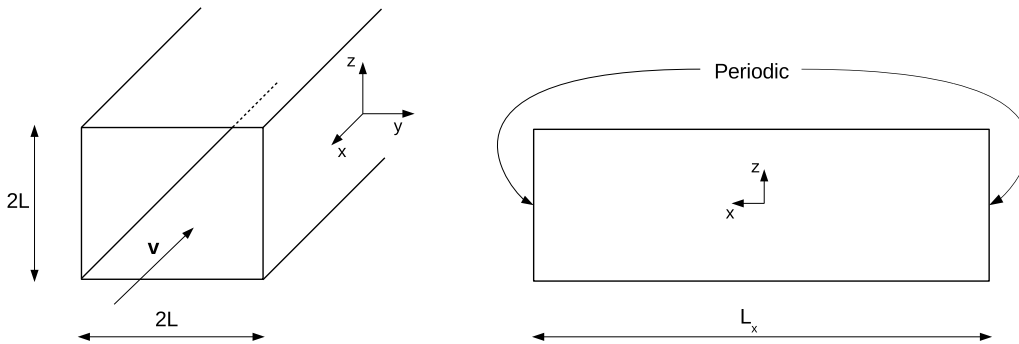


Figure 2.1: Schematic of the flow in a straight rectangular duct with periodic inflow and outflow. Throughout this study, $L_y = L_z = 2L$. x , y and z represent the streamwise, spanwise and the wall-normal directions respectively.

In the case of a flow at low magnetic Reynolds number ($R_m \ll 1$), the secondary magnetic field is assumed negligible when compared to the imposed magnetic field and hence the evolution of such MHD flows can be described by the so-called quasistatic or inductionless approximation (Roberts [1967]). However, when $R_m \sim 1$, the case that we consider, the induced magnetic field is comparable to the imposed magnetic field and it becomes necessary to model the time evolution of \mathbf{B} . The physics of the coupled evolution of the flow and magnetic fields is described by the Navier-Stokes equations and the magnetic field transport equations respectively, together with solenoidal constraints for both fields. We denote the half-channel width as L , the average streamwise velocity as U and the maximum value of the imposed magnetic field (generated from

electric currents in the exterior) on the duct walls as B_0 . Upon non-dimensionalization with the scales $L, U, L/U, \rho U^2, B_0$ and $\sigma U B_0$ for the length, velocity, time, pressure, magnetic field and current density respectively, and using small letters as the variable names for all the non-dimensional quantities, the system of governing equations in the interior of the duct Ω_i can be written as

$$\frac{\partial \mathbf{v}}{\partial t} + (\mathbf{v} \cdot \nabla) \mathbf{v} = -\nabla p + \frac{1}{Re} (\nabla^2 \mathbf{v} + Ha^2 (\mathbf{j} \times \mathbf{b}_t)), \quad (2.13)$$

$$\frac{\partial \mathbf{b}}{\partial t} + (\mathbf{v} \cdot \nabla) \mathbf{b}_t = (\mathbf{b}_t \cdot \nabla) \mathbf{v} + \frac{1}{R_m} \nabla^2 \mathbf{b}, \quad (2.14)$$

$$\nabla \cdot \mathbf{v} = 0, \quad (2.15)$$

$$\nabla \cdot \mathbf{b} = 0, \quad (2.16)$$

$$\mathbf{j} = \frac{1}{R_m} (\nabla \times \mathbf{b}), \quad (2.17)$$

$$\mathbf{v} = 0 \text{ on } \Sigma; \quad \mathbf{v}, \mathbf{b} \text{ periodic in } x\text{-direction} \quad (2.18)$$

where x, y and z denote the streamwise, spanwise and wall normal directions respectively. The standard no-slip and no penetration boundary conditions are assumed for \mathbf{v} on the wall boundaries Σ , along with periodicity in the streamwise direction. The duct walls Σ are considered to be electrically insulating ($\sigma = 0$ on Σ) which translates to vanishing wall normal current density $j_n = 0$.

The non-dimensional parameters involved in the system are the Reynolds number (Re), the Hartmann number (Ha) defined as

$$Re = \frac{UL}{\nu}, \quad Ha = B_0 L \sqrt{\frac{\sigma}{\rho \nu}} \quad (2.19)$$

and the magnetic Reynolds number (R_m). Here, ν and ρ represent the kinematic viscosity and the density of the fluid respectively. The magnetic Prandtl number relates the magnetic and hydrodynamic Reynolds numbers, and is defined as

$$Pr_m = \frac{R_m}{Re}. \quad (2.20)$$

However, we treat R_m as an independent parameter (instead of Pr_m) throughout this thesis.

The region outside the duct Ω_e is considered to be electrically insulating (e.g., air or vacuum). It is evident that the secondary magnetic field is not limited to the duct interior but extends across the duct walls and pervades the space outside the duct. This happens unless the duct walls are perfectly conducting, in which case the magnetic

field is bound within the interior of the duct. We denote the secondary magnetic field extending outside the duct as the exterior magnetic field. Although our primary interest is in the magnetic field inside the duct, a consistent treatment requires that the magnetic field is continuous across the duct walls. This is ensured by considering the magnetic field in the extended domain including the region outside the duct. Since electric currents cannot exist in the exterior, the magnetic field is curl free and hence can be expressed as the gradient of a magnetic scalar potential, $\mathbf{b} = -\nabla\psi$. Imposing the solenoidality condition (Gauss law, $\nabla \cdot \mathbf{b} = 0$) yields the following governing equations for the magnetic field in the exterior

$$\nabla^2\psi = 0, \quad \mathbf{b} = -\nabla\psi \quad \text{in } \Omega_e \cup \Sigma, \quad (2.21)$$

where Σ represents the duct wall boundary. In addition, it is assumed that no net streamwise current is applied, due to which the scalar potential ψ far away from the walls decreases faster than $\mathcal{O}(r^{-1})$ as $r \rightarrow \infty$, satisfying the far field condition, where r is the normal distance from the duct walls. Equations (2.13) to (2.18) together with (2.21) and the far field condition completely determine the physical system under consideration. However, since we are interested only in the solution of the magnetic field inside the duct, by means of the boundary integral approach, boundary conditions are obtained for the magnetic field that characterizes the matching of the exterior and interior fields at the wall boundary. This leads to non-local magnetic boundary conditions on the duct walls. A detailed discussion of the boundary integral procedure and the particular form of the non-local conditions will be given in the next chapter.

2.3 Jump conditions at the wall boundaries

As the electrical conductivity of the media changes across the wall boundaries of the domain, it is important to know the continuity properties of the electromagnetic field at the boundary in order to obtain consistent boundary conditions. Choosing the dimensional form of Maxwell's equations for the time being, the following equations are valid on both the sides of the interface Σ .

$$\frac{\partial \mathbf{B}_t}{\partial t} = -\nabla \times \mathbf{E}, \quad (2.22)$$

$$\mu_0 \mathbf{J} = \nabla \times \mathbf{B}_t. \quad (2.23)$$

A thin rectangular strip of area $l_y \times l_z$ across the interface is considered as shown in Fig. 2.2. Indicating the variables on the conducting and the insulating sides of the

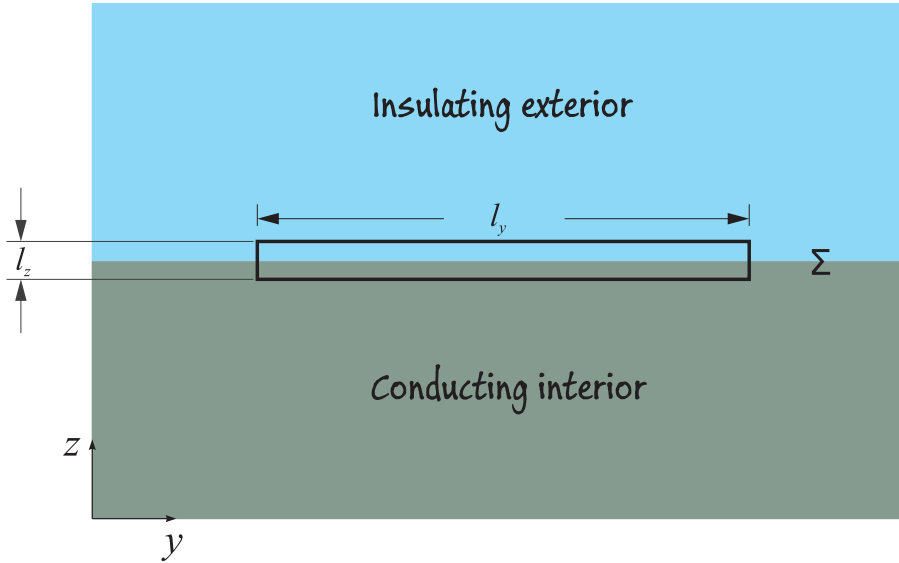


Figure 2.2: Schematic showing the rectangular area of integration extending slightly on both sides of the conductor-insulator interface Σ . The origin of the yz -coordinates shown in this figure is only representative and does not indicate the centre of the duct cross-section.

boundary by superscripts c and i respectively and integrating (2.22) over the area in the limit $l_z \rightarrow 0$, we get $E_y^c l_y - E_y^i l_y = 0$ or $E_y^c = E_y^i$. In other words, the tangential components of the electric field are continuous across the interface,

$$E_\tau^c|_\Sigma = E_\tau^i|_\Sigma \quad (2.24)$$

Similarly, integrating equation (2.23) over the strip yields the jump conditions for the tangential components of the magnetic field as

$$B_{i\tau}^c|_\Sigma = B_{i\tau}^i|_\Sigma \quad (2.25)$$

It must be noted that conditions (2.24) and (2.25) are valid for the general case of finite conductivity of the exterior medium. However, in the special case of insulating exterior, the condition (2.24) is not useful. In this case, integrating the dimensional version of (2.16) as in the previous cases, yields

$$B_{in}^c|_\Sigma = B_{in}^i|_\Sigma \quad (2.26)$$

for the wall normal component of the magnetic field. A detailed discussion of these conditions can be found in Shercliff [1965] and Iskakov & Dormy [2005]. To summarize, for the case of an insulating exterior, all the components of the magnetic field and only the tangential components of the electric field are continuous across the wall

boundaries. Advantage of this fact will be taken while obtaining proper boundary conditions for the magnetic field, which will be explained in the next chapter.

2.4 The quasistatic approximation - a brief note

In the case when the magnetic diffusivity is high or $R_m \ll 1$, the magnitude of the secondary magnetic field \mathbf{b} is small (and can be neglected), although the Lorentz forces are significant. In the limiting case of $R_m \rightarrow 0$, it is possible to obtain a simplified governing model which is approximate to the first order and get rid of dealing with the secondary magnetic field altogether. This is commonly known as the low- R_m or the quasistatic approximation in MHD. In fact, the value of R_m is very low in most industrial applications and laboratory experiments of MHD in which case the quasistatic approximation is fully justified and is commonly used. A very brief outline of the simplifications leading to the quasistatic approximation is as follows. The fact that \mathbf{b} is negligible means that the total magnetic field remains equal to \mathbf{b}_0 and does not vary with time. This implies that the electric field \mathbf{e} is curl-free and can be expressed as the gradient of a scalar potential ϕ as $\mathbf{e} = -\nabla\phi$. With this, the Ohm's law and its divergence will read as

$$\mathbf{j} = -\nabla\phi + \mathbf{v} \times \mathbf{b}_0, \quad (2.27)$$

$$\nabla^2\phi = \nabla \cdot (\mathbf{v} \times \mathbf{b}_0). \quad (2.28)$$

One can easily see that the main advantage of the quasistatic model (with respect to numerical treatment) lies in the fact that since \mathbf{j} is limited/bound to the conducting flow domain, simple boundary conditions arise, that does not require considering the exterior at all. For example, the condition of insulating walls translate to a Neumann boundary condition, $\partial\phi/\partial n$ on Σ .

Chapter 3

Numerical procedure

This chapter presents a coupled finite-difference/boundary integral numerical procedure that is implemented and used to perform direct numerical simulations (DNS) of turbulent magnetohydrodynamic duct flows at finite magnetic Reynolds numbers. Various levels of verification of the implementation of the numerical procedure are also presented hereby. The chapter ends with a brief study of magnetic field permeation into conductors/conducting flows at finite magnetic Reynolds numbers.

3.1 The problem of magnetic boundary conditions

The aim of this chapter is to present a computational procedure for direct numerical simulations (DNS) of MHD duct flow at finite magnetic Reynolds number. In this regime, as discussed in the previous chapter, the coupling between the flow and the magnetic field is significant and the effect of their interactions on turbulence is one of the primary motivations for this work. We choose the rectangular duct flow configuration for our study as it is frequently encountered in experimental studies of MHD and also in industrial applications.

Earlier studies of finite R_m MHD turbulence have mostly been performed in the periodic box setting (see e.g. Knaepen *et al.* [2004]; Oughton *et al.* [1994]). There are few existing studies of MHD turbulence at finite R_m that include the presence of a mean shear with wall boundaries (e.g., Hamba & Tsuchiya [2010]). The main challenge in the numerical computation of finite R_m MHD flows is the problem of magnetic boundary conditions that ensure proper matching of the magnetic field in the interior with that in the insulating exterior. This arises due to the fact that when R_m is finite, the secondary magnetic field is non-negligible and the equations governing it in the interior and exterior are different. In the case of spectral simulations in spherical geometries (as is the case with planets and stars), this problem is circumvented by poloidal-toroidal

3. Numerical Procedure

decomposition of the magnetic field and the use of expansions in spherical harmonics (Christensen *et al.* [2001]). Such a procedure leads to boundary conditions that are decoupled for each harmonic. Similar simplification of boundary conditions is possible in configurations with two periodic directions like that of a cylindrical pipe or plane channel flows. However such simplifying procedures cannot be employed for non-periodic geometries (e.g., a duct).

Several strategies have been adopted by prior studies to incorporate the effect of the exterior magnetic field. One of them is the vertical field or pseudo-vacuum boundary condition that has been used in several instances of astrophysical and dynamo simulations (Brandenburg *et al.* [1995]; Gailitis *et al.* [2004]; Hubbard & Brandenburg [2010]; Hurlburt & Toomre [1988]; Kenjereš & Hanjalić [2007]; Rüdiger & Zhang [2001]) particularly due to its simplicity. An alternative method that was used in the simulation of the Karlsruhe dynamo experiment (see Rädler *et al.* [1998, 2002]), was to immerse the conducting dynamo domain into a sphere, with the region between the sphere and the boundary of the conducting domain assumed to be filled with a material of low conductivity. However, both of these methods are associated with loss of solution accuracy. A rather straightforward procedure is to find a solution for the magnetic field in the exterior domain together with the interior (e.g. Kenjereš *et al.* [2006]; Stefani *et al.* [1999]). An approach similar to this but using the finite element method was proposed by Guermond *et al.* [2007, 2003] and subsequently applied for dynamo problems (see Guermond *et al.* [2009]; Nore *et al.* [2011]). This approach is however computationally demanding and is necessary only if one is interested in the solution of the exterior magnetic field.

An alternative and elegant formulation, the velocity-current formulation, was first proposed and rigorously analyzed by Meir *et al.* (Meir & Schmidt [1994, 1996, 1999]) for stationary MHD flows and was further extended to time dependent flows in Schmidt [1999]. This formulation takes advantage of the fact that the current density field is bounded within the domain (unlike the magnetic field) and instead of the induction equation for the magnetic field, an integro-differential transport equation for the current density is proposed. Subsequently Stefani *et al.* (Stefani *et al.* [2000]; Xu *et al.* [2004]) introduced similar formulations (the integral equation approach) to kinematic dynamo problems and used it to simulate the von Kármán Sodium and Riga dynamo experiments (Xu *et al.* [2008]). More recent developments and applications of this method can be found in Stefani *et al.* [2013]. Nevertheless, it has been suggested that this procedure too requires large computational resources (Giesecke *et al.* [2008]), primarily due to the volume integrals that have to be evaluated at every time step. Computationally more efficient is the coupled finite element-boundary integral approach that

has been traditionally used to solve pure electromagnetic problems (see e.g. Bossavit [1991]; Bossavit & V erit e [1982]). A finite-volume variant of this method was first proposed by Iskakov et al. (Iskakov *et al.* [2004]; Iskakov & Dormy [2005]) to solve the induction equation and subsequently applied to kinematic dynamo simulations by Giesecke *et al.* [2008].

Clearly, DNS of MHD duct flow at finite R_m with consistent treatment of the exterior domain has not been attempted in prior studies. In this chapter, the general approach of the coupled interior-exterior solution using the boundary integral procedure is applied to the problem of turbulent magnetohydrodynamic flow in rectangular ducts. Specific geometric features such as the existence of corners and two non-periodic directions along with the need to treat magnetic diffusion in an implicit manner (unlike the case of high R_m flows, where explicit schemes are typical) with integral boundary conditions, makes the problem computationally challenging. Here, we describe a divergence preserving semi-implicit hybrid finite-difference boundary integral numerical procedure for the problem of MHD duct flow with streamwise periodicity.

This chapter is organized as follows. In section 3.2, the general details of the numerical procedure adopted for the hydrodynamic part is briefly described followed by the elaboration of the boundary integral approach and the algorithm for the coupled numerical procedure adopted to solve for the magnetic field. In section 3.3, several test cases are presented in the limiting regime of low R_m to verify the numerical implementation of the magnetic boundary conditions. In section 3.4, an explicit version of the numerical procedure is briefly outlined. Finally, in section 3.5, study of magnetic field permeation in stationary conductors and laminar flow at finite R_m are presented.

3.2 Numerical procedure

3.2.1 The interior problem

The governing partial differential equations for the velocity and the magnetic fields inside the duct are solved numerically using the finite difference approach. The domain is discretized into a structured rectangular Cartesian grid and the solution variables are approximated at the grid points which correspond to the collocated grid arrangement. In duct MHD flows in a uniform external magnetic field, specific boundary layers with steep velocity gradients and high current densities are formed near the walls (M uller & B uller [2001]). These correspond to the Hartmann layers at the walls normal to the imposed magnetic field and the Shercliff layers at the walls aligned with the initial magnetic field \mathbf{b}_0 . In order to resolve the thin boundary layers, the grid in the cross

3. Numerical Procedure

section is stretched to obtain a non-uniform grid with high grid clustering near the walls. The non-uniform grid in both wall-normal directions is obtained by a coordinate transformation from the uniform-grid coordinates (ζ, η) according to

$$y = L \frac{\tanh(S_y \zeta)}{\tanh(S_y)} , \quad z = L \frac{\tanh(S_z \eta)}{\tanh(S_z)} , \quad (3.1)$$

where S_y, S_z correspond to the degree of stretching in the y - and z - directions respectively. However, a uniform grid in the x -direction is considered so as to take advantage of the periodicity through Fourier decomposition. In order to keep the chapter self contained, we now briefly describe the computational procedure adopted for the solution of velocity field from the Navier-Stokes equations. The time discretization is performed by a second-order backward difference scheme using the 3 time levels $n - 1, n, n + 1$ when marching from time level n to $n + 1$ as

$$\frac{\partial \mathbf{v}}{\partial t} \approx \frac{3\mathbf{v}^{n+1} - 4\mathbf{v}^n + \mathbf{v}^{n-1}}{2\Delta t}. \quad (3.2)$$

The viscous term can be treated using either an explicit or implicit procedure, whereas the non-linear advective term and the Lorentz force term are treated explicitly using the Adams-Bashforth method. The advective, Lorentz force and viscous terms can be summed up into \mathbf{F}^n as

$$\mathbf{F}^n = -(\mathbf{v}^n \cdot \nabla) \mathbf{v}^n + \frac{Ha^2}{Re} (\mathbf{j} \times \mathbf{b}_t^n) + \frac{(1 - \theta)}{Re} \nabla^2 \mathbf{v}^n, \quad (3.3)$$

where binary factor θ assumes the values 0 and 1 for the explicit and implicit treatments respectively. The implicit treatment of the viscous term can be advantageous for the case of small Re . The velocity field is obtained by the well known projection method, wherein an intermediate velocity field \mathbf{v}^* is computed using

$$\frac{3\mathbf{v}^* - 4\mathbf{v}^n + \mathbf{v}^{n-1}}{2\Delta t} = 2\mathbf{F}^n - \mathbf{F}^{n-1} + \frac{\theta}{Re} \nabla^2 \mathbf{v}^*, \quad (3.4)$$

which leads to a Poisson-type equation for \mathbf{v}^* in the implicit case. The pressure field p^{n+1} is then computed from the continuity equation by solving another Poisson problem,

$$\nabla^2 p^{n+1} = \frac{3}{2\Delta t} \nabla \cdot \mathbf{v}^*. \quad (3.5)$$

Integrating (3.5) over the whole domain and applying the Gauss-divergence theorem will yield the boundary condition for pressure on Σ as

$$\frac{\partial p^{n+1}}{\partial n} = \frac{3}{2\Delta t} v_n^*, \quad (3.6)$$

where the subscript n refers to the wall normal component. Subsequently the intermediate non-solenoidal velocity field \mathbf{v}^* is projected onto a divergence-free velocity field \mathbf{v} at the time level $n + 1$ using the pressure field obtained from (3.5) as

$$\mathbf{v}^{n+1} = \mathbf{v}^* - \frac{2\Delta t}{3} \nabla p^{n+1}. \quad (3.7)$$

A Fourier transformation is applied in the x -direction to the discrete forms of the Poisson equations (3.4), (3.5) for the velocity and pressure. The transformed equations are then solved in the wavenumber space as a series of 2D (y - z plane) problems using the Fortran software package FISHPACK (Adams *et al.* [1999]) that uses a cyclic reduction algorithm (direct solver) for the solution of 2D elliptic equations. Further details of the numerical procedure for the hydrodynamic solution can be found in Krasnov *et al.* [2011].

We now turn our attention to the solution of the magnetic induction equation (2.14). A discretization procedure similar to that used for the implicit treatment of the momentum equation is followed with only the diffusive term treated implicitly. Unlike the momentum equation, the implicit treatment here is really essential due to the fact that the diffusive time scale in the case of $R_m \sim 1$ is comparable to the time scale of advection of the magnetic field. Discretization of the induction equation yields

$$\frac{3\mathbf{b}^{n+1} - 4\mathbf{b}^n + \mathbf{b}^{n-1}}{2\Delta t} = 2\mathbf{T}^n - \mathbf{T}^{n-1} + \frac{1}{R_m} \nabla^2 \mathbf{b}^{n+1} \quad (3.8)$$

for the secondary magnetic field \mathbf{b} at the $n+1$ level where \mathbf{T}^n includes the advective and the magnetic field stretching terms and is given by

$$\mathbf{T}^n = -(\mathbf{v}^n \cdot \nabla) \mathbf{b}_t^n + (\mathbf{b}_t^n \cdot \nabla) \mathbf{v}^n. \quad (3.9)$$

Further simplification of (3.8) leads to a Poisson-type equation for \mathbf{b}^{n+1} as

$$-f\mathbf{b}^{n+1} + \nabla^2 \mathbf{b}^{n+1} = -f\mathbf{q}, \quad (3.10)$$

where $f = \frac{3R_m}{2\Delta t}$ is a discretization coefficient and \mathbf{q} is the right hand side that retains the known terms from the time steps n and $n - 1$. The system being periodic in the

3. Numerical Procedure

streamwise direction, we now introduce a Fourier transformation in the x -direction as

$$\mathbf{b}(x, y, z) = \Re \left\{ \sum_{k=0}^{k=\frac{N_x}{2}-1} \hat{\mathbf{b}}_k(y, z) e^{i\alpha_k x} \right\}, \quad (3.11)$$

where \Re represents the real part, N_x is the number of grid intervals along the x -direction and α_k is the streamwise wavenumber defined as $\alpha_k = 2\pi k/L_x$, L_x being the length of the duct. Substituting (3.11) into (3.10) leads to a 2D elliptic equation in the yz -plane for the complex Fourier coefficients $\hat{\mathbf{b}}_k$ as

$$(-f - \alpha_k^2) \hat{\mathbf{b}}_k + \nabla_{yz}^2 \hat{\mathbf{b}}_k = -f \hat{\mathbf{q}}_k, \quad (3.12)$$

with $\hat{\mathbf{b}}_k = [\hat{b}_{xk}, \hat{b}_{yk}, \hat{b}_{zk}]$ and $\nabla_{yz}^2 = \partial_y^2 + \partial_z^2$ is the 2D Laplace operator. This step is essential as we reduce the complexity of matching the magnetic field of a three-dimensional interior (Ω_i) and an exterior (Ω_e) to a planar problem for each Fourier coefficient. Here, the superscript $n+1$ is dropped for the sake of simplicity. Solution of (3.12) requires proper boundary conditions for the magnetic field that matches the exterior field, which will be the subject of the following section.

3.2.2 Boundary integral equation and the coupled numerical procedure

In this section we will derive suitable boundary conditions (in the Fourier space) required for the closure of (3.12) and present a coupled iterative solution procedure to solve the resulting system. This is done through the boundary integral approach, by which the matching of the interior solution with the exterior solution at the boundary translates into non-local boundary conditions. The governing Laplace equation (2.21) for the exterior magnetic potential transforms to the 2D Helmholtz equation in the k -space as

$$(\nabla^2 - \alpha_k^2) \hat{\psi}_k = 0. \quad (3.13)$$

The Green's function or the fundamental solution of the 2D Helmholtz operator is denoted by $G_k(\mathbf{r}', \mathbf{r})$ that satisfies $(\nabla^2 - \alpha_k^2) G_k(\mathbf{r}', \mathbf{r}) = -\delta(\mathbf{r}' - \mathbf{r})$ where $\delta(\mathbf{r}' - \mathbf{r})$ is the Dirac delta function centered around the pole $\mathbf{r}' = y'\mathbf{j} + z'\mathbf{k}$, with \mathbf{j} and \mathbf{k} representing the unit vectors in the y and z directions respectively (see Fig. 3.1).

Considering \mathbf{r}' to be a point on the rectangular boundary Γ , we see that

$$\begin{aligned}
 & \int_{\Lambda_e} \nabla \cdot (\hat{\psi}_k(\mathbf{r}) \nabla G_k(\mathbf{r}', \mathbf{r}) - G_k(\mathbf{r}', \mathbf{r}) \nabla \hat{\psi}_k(\mathbf{r})) dA \\
 &= \int_{\Lambda_e} (\hat{\psi}_k(\mathbf{r}) \nabla^2 G_k(\mathbf{r}', \mathbf{r}) - G_k(\mathbf{r}', \mathbf{r}) \nabla^2 \hat{\psi}_k(\mathbf{r})) dA \\
 &= - \int_{\Lambda_e} \hat{\psi}_k(\mathbf{r}) \delta(\mathbf{r}' - \mathbf{r}) dA = 0,
 \end{aligned} \tag{3.14}$$

where the area of integration includes the exterior region between the big circle and the rectangular domain excluding a small semi-circle of radius ε in the vicinity of the pole \mathbf{r}' as shown in Fig. 3.1.

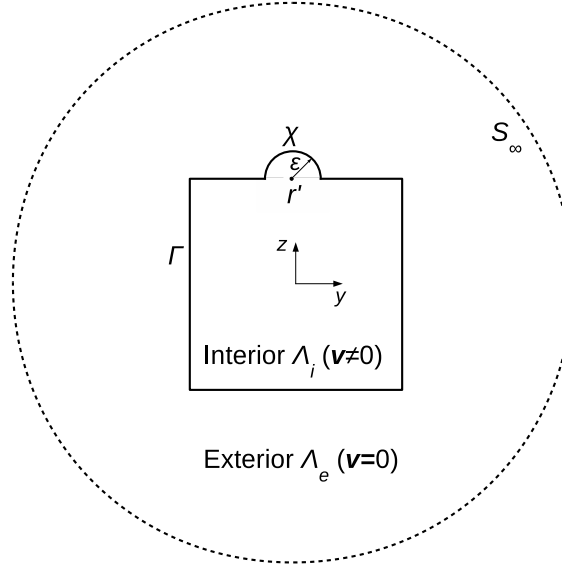


Figure 3.1: Region of integration between the rectangular boundary Γ and an outer circle S_∞ excluding a small semi-circle χ of radius ε . This part of the solution procedure is done in a plane. Thus Λ_i relates to Ω_i , Λ_e to Ω_e and Γ to Σ from the original 3D setting.

Using Gauss-divergence theorem, equation (3.14) can be rewritten as

$$\begin{aligned}
 & \int_{\Gamma} (\hat{\psi}_k(\mathbf{r}) \nabla G_k(\mathbf{r}', \mathbf{r}) - G_k(\mathbf{r}', \mathbf{r}) \nabla \hat{\psi}_k(\mathbf{r})) \cdot \mathbf{n} dl \\
 &+ \int_{\chi} (\hat{\psi}_k(\mathbf{r}) \nabla G_k(\mathbf{r}', \mathbf{r}) - G_k(\mathbf{r}', \mathbf{r}) \nabla \hat{\psi}_k(\mathbf{r})) \cdot \mathbf{n} dl \\
 &+ \int_{S_\infty} (\hat{\psi}_k(\mathbf{r}) \nabla G_k(\mathbf{r}', \mathbf{r}) - G_k(\mathbf{r}', \mathbf{r}) \nabla \hat{\psi}_k(\mathbf{r})) \cdot \mathbf{n} dl = 0,
 \end{aligned} \tag{3.15}$$

where \mathbf{n} is the local unit outward normal vector at \mathbf{r} on the boundaries and l is the arc length. The third term (integral over S_∞) vanishes as $\mathbf{r} \rightarrow \infty$. The second term (integral over χ) is simplified with the assumption that $\hat{\psi}_k$ and $\frac{\partial \hat{\psi}_k}{\partial n}$ do not vary within

3. Numerical Procedure

the half-circle χ as the radius ε is considered small:

$$\begin{aligned}
 \int_{\chi} \hat{\psi}_k(\mathbf{r}) \nabla G_k(\mathbf{r}', \mathbf{r}) \cdot \mathbf{n} dl &= \hat{\psi}_k(\mathbf{r}') \int_S \nabla^2 G_k(\mathbf{r}', \mathbf{r}) dS \\
 &= \hat{\psi}_k(\mathbf{r}') \int_S (-\delta(\mathbf{r}' - \mathbf{r}) + \alpha_k^2 G_k(\mathbf{r}', \mathbf{r})) dS \quad (3.16) \\
 &= -\frac{1}{2}(\mathbf{r}') \hat{\psi}_k(\mathbf{r}') + \alpha_k^2 \hat{\psi}_k(\mathbf{r}') \int_S G_k(\mathbf{r}', \mathbf{r}) dS,
 \end{aligned}$$

where l is the coordinate along χ and S represents the area bounded by the half-circle χ . Using the fact that $G_k(\mathbf{r}', \mathbf{r}) \sim \ln(|\mathbf{r}' - \mathbf{r}|)$ for small ε , the second term in the above equation vanishes as $\varepsilon \rightarrow 0$. In the case when \mathbf{r}' lies at one of the four corners of Γ , χ would correspond to a three-quarter circle. Furthermore,

$$\begin{aligned}
 \int_{\chi} -G_k(\mathbf{r}', \mathbf{r}) \nabla \hat{\psi}_k(\mathbf{r}) \cdot \mathbf{n} dl &= -\frac{\partial \hat{\psi}_k}{\partial n}(\mathbf{r}') \int_{\chi} G_k(\mathbf{r}', \mathbf{r}) dl \quad (3.17) \\
 &= -\frac{\partial \hat{\psi}_k}{\partial n}(\mathbf{r}') \ln(\varepsilon) 2\pi\varepsilon \rightarrow 0, \quad \varepsilon \rightarrow 0.
 \end{aligned}$$

With the above simplifications, the boundary integral equation in the general form can be written as

$$\beta(\mathbf{r}') \hat{\psi}_k(\mathbf{r}') = \text{P.V.} \oint_{\Gamma} [G_k(\mathbf{r}', \mathbf{r}) \hat{b}_{nk}(\mathbf{r}) + \hat{\psi}_k(\mathbf{r}) \frac{\partial G_k}{\partial n}(\mathbf{r}', \mathbf{r})] dl(\mathbf{r}), \quad (3.18)$$

where $\hat{b}_{nk}(\mathbf{r}) = -\frac{\partial \hat{\psi}_k}{\partial n}(\mathbf{r})$, $\beta(\mathbf{r}')$ is a constant that depends on the location of the pole \mathbf{r}' on the rectangular boundary Γ and is given by

$$\beta(\mathbf{r}') = \begin{cases} \frac{3}{4}, & \text{if } \mathbf{r}' \in \text{corner,} \\ \frac{1}{2}, & \text{otherwise,} \end{cases} \quad (3.19)$$

n being the local outward wall normal coordinate at \mathbf{r} . It should be mentioned that the integration along the rectangular contour Γ must be performed in the sense of a Cauchy principal value (CPV) (Bronshtein & Semendyayev [1997]). The boundary condition (3.18) is a Fredholm integral equation of the 2nd kind with a singular kernel. The singularity would be apparent from the specific form of the Green's function given by

$$G_k(\mathbf{r}', \mathbf{r}) = \frac{1}{2\pi} K_0(\alpha_k(|\mathbf{r}' - \mathbf{r}|)), \quad (3.20)$$

K_0 being the MacDonal function which corresponds to the complex valued Hankel

function of zero order H_0 (Stakgold [2000]). For numerical evaluation, the following series expansion formulae from Abramowitz & Stegun [1964] are particularly useful

$$K_0(x) = \begin{cases} -\ln\left(\frac{x}{2}\right)I_0(x) + \sum_{n=1}^7 C_n \left(\frac{x^2}{4}\right)^{n-1}, & \text{if } x \leq 2 \\ \frac{e^{-x}}{\sqrt{x}} \sum_{n=1}^7 D_n \left(\frac{x}{2}\right)^{n-1}, & \text{otherwise} \end{cases} \quad (3.21)$$

$$I_0(x) = 1 + \sum_{n=1}^6 E_n y^n, \quad y = \left(\frac{x}{3.75}\right)^2, \quad |x| < 3.75, \quad (3.22)$$

in which I_0 represents the modified Bessel function of the first kind and C_n, D_n, E_n are the series coefficients (Abramowitz & Stegun [1964]). It can be seen that for $x \rightarrow 0$, $K_0(x) \sim -\ln x$ which explains the logarithmic singularity at the pole.

Solution of (3.12) for the in-plane components \hat{b}_{yk} and \hat{b}_{zk} requires the normal and tangential components \hat{b}_{nk} and $\hat{b}_{\tau k}$ on the boundary Γ which are connected through the potential $\hat{\psi}_k$ given by (3.18). The normal component \hat{b}_n on the boundary can be evaluated from the Gauss's law as

$$\frac{\partial \hat{b}_{nk}}{\partial n} + \frac{\partial \hat{b}_{\tau k}}{\partial \tau} = -\alpha_k^2 \hat{\psi}_k \quad (3.23)$$

and the tangential component $\hat{b}_{\tau k}$ obtained from

$$\hat{b}_{\tau k} = -\frac{\partial \hat{\psi}_k}{\partial \tau}, \quad (3.24)$$

which closes the problem of evaluating the in-plane components \hat{b}_{yk} and \hat{b}_{zk} .

Equations (3.12), (3.23) and (3.24) are discretized by finite differences and equation (3.18) is discretized by the boundary element method and are solved together iteratively for the numerical solution of the two components. A coupled iterative procedure between the interior and the boundary has been adopted here. The discrete form of the elliptic equation (3.12) is used to update \hat{b}_{yk} and \hat{b}_{zk} in the strict interior by a Gauss-Seidel like method using boundary values from the previous iteration. The component of \hat{b}_{nk} on grid points adjacent to the boundary is then used to update \hat{b}_{nk} on Γ through (3.23). The updated \hat{b}_{nk} is used to update $\hat{\psi}_k(\mathbf{r}')$ on Γ through the discrete form of (3.18) which is subsequently used to evaluate $\hat{b}_{\tau k}$ from (3.24). This iterative procedure alternating between the interior and the boundary is performed until the required convergence criterion is met. The procedure for a single iteration is summarized below

- Compute \hat{b}_{yk} and \hat{b}_{zk} on Λ_i with $(-f - \alpha_k^2) \hat{\mathbf{b}}_k + \nabla_{yz}^2 \hat{\mathbf{b}}_k = -f \hat{\mathbf{q}}_k$

3. Numerical Procedure

- Compute \hat{b}_{nk} on Γ with $\frac{\partial \hat{b}_{nk}}{\partial n} + \frac{\partial \hat{b}_{\tau k}}{\partial \tau} = -\alpha_k^2 \hat{\psi}_k$
- Compute $\hat{\psi}_k$ on Γ with
$$\beta(\mathbf{r}') \hat{\psi}_k(\mathbf{r}') = \text{P.V.} \oint_{\Gamma} [G_k(\mathbf{r}', \mathbf{r}) \hat{b}_{nk}(\mathbf{r}) + \hat{\psi}_k(\mathbf{r}) \frac{\partial G_k}{\partial n}(\mathbf{r}', \mathbf{r})] dl(\mathbf{r})$$
- Compute $\hat{b}_{\tau k}$ on Γ with $\hat{b}_{\tau k} = -\frac{\partial \hat{\psi}_k}{\partial \tau}$.

It must be noted that although it is possible to use direct solvers to solve the discretized forms of equations (3.12), (3.23), (3.24) and (3.18), the iterative procedure is found to be computationally efficient mainly due to the very good initial guess obtained for the unknown variables from the previous time step.

We now turn to the discretization of the boundary integral equation (3.18) which forms the basis of the coupled iterative procedure just described. Equation (3.18) is

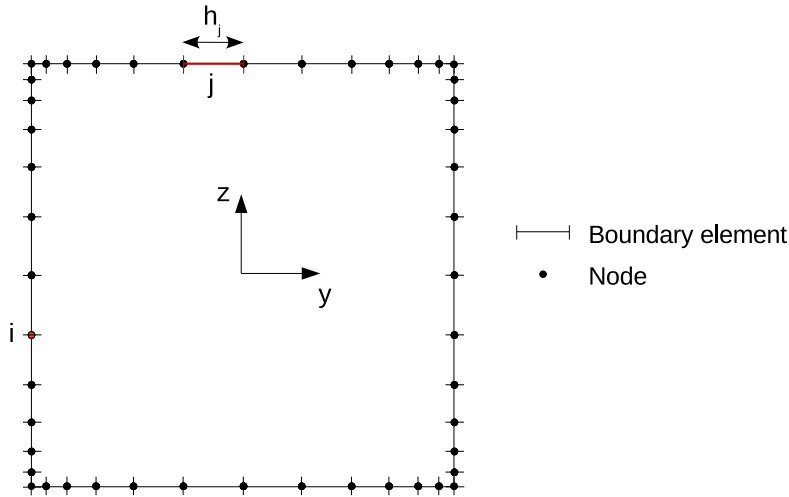


Figure 3.2: Representative discretization of the rectangular boundary Γ into nodes and boundary elements.

discretized to obtain a set of algebraic equations by the formalism of boundary element method (Brebbia & Walker [1978]). The rectangular boundary is divided into a number of small line segments called boundary elements and the contour integral along Γ is approximated as a sum of integrals along each of these elements. The solution variable $\hat{\psi}_k$ is approximated at the ends of the boundary elements which are denoted as nodes. The nodes are numbered with the variable i and the elements are numbered using the variable j . The locations of the boundary elements and nodes are shown in Fig. 3.2. This layout of the elements leads to a double node at each of the four corners of Γ which is essential in order to deal with the singularity that exists for the normal vector \hat{n} at the corners. A piecewise linear variation of $\hat{\psi}_k$ is assumed along each element. Denoting the length of the j^{th} element by h_j and temporarily omitting the subscript k

for simplicity of notation, the discrete version of (3.18) for node i at \mathbf{r}' can then be written as

$$\begin{aligned} \beta_i \hat{\psi}_i - \sum_{j=1}^{j=N_b} \int_0^{h_j} \left(\frac{\hat{\psi}_j (h_j - l) + \hat{\psi}_{j+1} l}{h_j} \right) \frac{\partial G}{\partial n}(\mathbf{r}'_i, \mathbf{r}_j) dl \\ = \sum_{j=1}^{j=N_b} \int_0^{h_j} \left(\frac{\hat{b}_{nj} (h_j - l) + \hat{b}_{nj+1} l}{h_j} \right) G(\mathbf{r}'_i, \mathbf{r}_j) dl \end{aligned} \quad (3.25)$$

for $1 \leq i \leq N_b$, N_b being the number of boundary nodes (see Fig. 3.2). The index i is considered to run in the clockwise direction starting from $i = 1$ at the lower left corner node to $i = N_b = 2(N_y + N_z)$ at the node next (on the right) to it. We now first focus on evaluating the summation of numerical integrals on the right hand side. The idea is to evaluate the integral along each element j using a 4-point Gauss-Legendre quadrature (Abramowitz & Stegun [1964]). Such a quadrature even within each element is important in order to be able to capture the steep gradients in the Green's function for the wide range of wavenumbers (α_k) involved. However, caution is necessary for the computation of the integral over those elements/panels j that contain the pole \mathbf{r}'_i (or the node i) as the function K_0 is singular at the pole. The logarithm poses a weak singularity and is dealt with analytical integration over the two elements ($j = i - 1$ and $j = i$) lying on either side of the node i which is possible since the integral is convergent (Christiansen [1971]). With this in mind, the right hand side term of (3.25), denoted as m_i hereafterwards, is decomposed as

$$\begin{aligned} m_i = \frac{1}{h_j} \sum_{\substack{j=1 \\ j \neq i-1 \\ j \neq i}}^{j=N_b} \int_0^{h_j} \left(\frac{\hat{b}_{nj} (h_j - l) + \hat{b}_{nj+1} l}{h_j} \right) G(\mathbf{r}'_i, \mathbf{r}_j) dl \\ + \frac{1}{h_j} \sum_{j=i-1}^{j=i} \int_0^{h_j} \left(\frac{\hat{b}_{nj} (h_j - l) + \hat{b}_{nj+1} l}{h_j} \right) G(\mathbf{r}'_i, \mathbf{r}_j) dl \\ = m_i^1 + m_i^2. \end{aligned} \quad (3.26)$$

Now, in order to accommodate for the general case of also including the corners (that has two different normal directions), we now introduce the notation $b_{nb,j}$ and $b_{nf,j}$ to represent the backward normal and forward normal directions with additional subscripts b and f respectively. It can be immediately seen that $b_{nb,j} = b_{nf,j}$ for all nodes j that are not corners. Using this and also denoting $G(\mathbf{r}'_i, \mathbf{r}_j)$ as $G_{i,j}$, the first term of (3.26)

3. Numerical Procedure

can be written as

$$\begin{aligned}
 m_i^1 &= \frac{1}{h_j} \sum_{\substack{j=1 \\ j \neq i-1 \\ j \neq i}}^{j=N_b} \int_0^{h_j} \left(\frac{\hat{b}_{nf,j}(h_j-l) + \hat{b}_{nb,j+1}l}{h_j} \right) G_{i,j} dl \\
 &= \sum_{\substack{j=1 \\ j \neq i-1 \\ j \neq i}}^{j=N_b} \hat{b}_{nf,j} \int_0^{h_j} G_{i,j} dl + \frac{1}{h_j} (\hat{b}_{nb,j+1} - \hat{b}_{nf,j}) \int_0^{h_j} G_{i,j} dl
 \end{aligned} \tag{3.27}$$

Choosing four Gaussian points within each element, denoting the value of $G_{i,j}$ at these locations as $G_{i,j,1}, G_{i,j,2}, G_{i,j,3}$ and $G_{i,j,4}$, the Gaussian weights as w_1, w_2, w_3 and w_4 and the locations of these points within the element as l_1, l_2, l_3 and l_4 , the above equation can be evaluated as

$$m_i^1 = \sum_{\substack{j=1 \\ j \neq i-1 \\ j \neq i}}^{j=N_b} \frac{h_j}{2} \hat{b}_{nf,j} \sum_{j'=1}^{j'=4} w_{j'} G_{i,j,j'} + \frac{1}{2} (\hat{b}_{nb,j+1} - \hat{b}_{nf,j}) \sum_{j'=1}^{j'=4} w_{j'} l_{j'} G_{i,j,j'} \tag{3.28}$$

The second term (m_i^2) of (3.26) that contains the kernel singularity can be evaluated as

$$\begin{aligned}
 m_i^2 &= \hat{b}_{nf,i-1} \int_0^{h_{i-1}} G(\mathbf{r}'_i, \mathbf{r}_{i-1}) dl + \frac{1}{h_{i-1}} (\hat{b}_{nb,i} - \hat{b}_{nf,i-1}) \int_0^{h_{i-1}} G(\mathbf{r}'_i, \mathbf{r}_{i-1}) dl \\
 &\quad + \hat{b}_{nf,i} \int_0^{h_i} G(\mathbf{r}'_i, \mathbf{r}_i) dl + \frac{1}{h_i} (\hat{b}_{nb,i+1} - \hat{b}_{nf,i}) \int_0^{h_i} G(\mathbf{r}'_i, \mathbf{r}_i) dl
 \end{aligned} \tag{3.29}$$

Using the specific form of the Green's function as in (3.21), we can analytically evaluate the integral over the panel i in the above equation as

$$\begin{aligned}
 \int_0^{h_i} G(\mathbf{r}'_i, \mathbf{r}_i) dl &= h_i \left[1 - \ln \left(\frac{\alpha_k h_i}{2} \right) \right] + \sum_{n=1}^{n=6} E_n \left(\frac{\alpha_k}{3.75} \right)^{2n} \frac{h_i^{2n+1}}{(2n+1)^2} \left[1 - (2n+1) \ln \left(\frac{\alpha_k h_i}{2} \right) \right] \\
 &\quad + \sum_{n=1}^{n=7} C_n \left(\frac{\alpha_k}{2} \right)^{2n-2} \frac{h_i^{2n-1}}{(2n-1)} = I_1(i).
 \end{aligned} \tag{3.30}$$

Additionally, it can be easily verified that

$$\int_0^{h_{i-1}} G(\mathbf{r}'_i, \mathbf{r}_{i-1}) dl = I_1(i-1). \quad (3.31)$$

Furthermore,

$$\begin{aligned} \int_0^{h_i} lG(\mathbf{r}'_i, \mathbf{r}_i) dl &= \frac{h_i^2}{4} \left[1 - 2 \ln \left(\frac{\alpha_k h_i}{2} \right) \right] + \sum_{n=1}^{n=6} E_n \left(\frac{\alpha_k}{3.75} \right)^{2n} \frac{h_i^{2n+2}}{(2n+2)^2} \\ &\left[1 - (2n+2) \ln \left(\frac{\alpha_k h_i}{2} \right) \right] + \sum_{n=1}^{n=7} C_n \left(\frac{\alpha_k}{2} \right)^{2n} \frac{h_i^{2n-1}}{2n} = I_2(i). \end{aligned} \quad (3.32)$$

With a little simplification, it can also be seen that

$$\int_0^{h_{i-1}} lG(\mathbf{r}'_i, \mathbf{r}_{i-1}) dl = h_{i-1}I_1(i-1) - I_2(i-1). \quad (3.33)$$

Now, using equations (3.30), (3.31), (3.32) and (3.33), equation (3.29) can be written in a condensed form as

$$\begin{aligned} m_i^2 &= \hat{b}_{nf,i-1} I_1(i-1) + \frac{1}{h_{i-1}} (\hat{b}_{nb,i} - \hat{b}_{nf,i-1}) [h_{i-1} I_1(i-1) - I_2(i-1)] + \hat{b}_{nf,i} I_1(i) \\ &+ \frac{1}{h_i} (\hat{b}_{nb,i+1} - \hat{b}_{nf,i}) I_2(i) \\ &= \hat{b}_{nb,i} I_1(i-1) + \frac{1}{h_{i-1}} (\hat{b}_{nf,i-1} - \hat{b}_{nb,i}) I_2(i-1) + \hat{b}_{nf,i} I_1(i) \\ &+ \frac{1}{h_i} (\hat{b}_{nb,i+1} - \hat{b}_{nf,i}) I_2(i). \end{aligned} \quad (3.34)$$

The terms on the left hand side of (3.25) will be evaluated as

$$\begin{aligned} \beta_i \hat{\psi}_i &- \sum_{j=1}^{j=N_b} \int_0^{h_j} \left(\frac{\hat{\psi}_j (h_j - l) + \hat{\psi}_{j+1} l}{h_j} \right) \frac{\partial G}{\partial n}(\mathbf{r}'_i, \mathbf{r}_j) dl \\ &= \beta_i \hat{\psi}_i - \sum_{j=1}^{j=N_b} \left[\hat{\psi}_j \int_0^{h_j} \frac{\partial G_{i,j}}{\partial n} dl + \frac{1}{h_j} (\hat{\psi}_{j+1} - \hat{\psi}_j) \int_0^{h_j} \frac{\partial G_{i,j}}{\partial n} l dl \right]. \end{aligned} \quad (3.35)$$

Choosing four Gaussian points within each element, denoting the value of $\frac{\partial G_{i,j,j'}}{\partial n}$ at these locations as $\frac{\partial G_{i,j,1}}{\partial n}$, $\frac{\partial G_{i,j,2}}{\partial n}$, $\frac{\partial G_{i,j,3}}{\partial n}$ and $\frac{\partial G_{i,j,4}}{\partial n}$, the above term can be further evalu-

3. Numerical Procedure

ated as

$$\beta_i \hat{\psi}_i - \sum_{j=1}^{j=N_b} \left[\frac{h_j}{2} \hat{\psi}_j \sum_{j'=1}^{j=4} w_{j'} \frac{\partial G_{i,j,j'}}{\partial n} + \frac{1}{2} (\hat{\psi}_{j+1} - \hat{\psi}_j) \sum_{j'=1}^{j=4} w_{j'} l_{j'} \frac{\partial G_{i,j,j'}}{\partial n} \right]. \quad (3.36)$$

The above term being applicable for all boundary nodes i , can be written in the matrix form as $S_{ii'} \hat{\psi}_i$ where

$$S_{ii'}(\mathbf{r}') = \begin{cases} \beta_i, & \text{if } i = i' \\ - \left[\frac{h_{i'}}{2} \sum_{j'=1}^{j'=4} w_{j'} \frac{\partial G_{i,i',j'}}{\partial n} + \frac{1}{2} \sum_{j'=1}^{j'=4} \left(w_{j'} l_{i'-1,j'} \frac{\partial G_{i,i'-1,j'}}{\partial n} - w_{j'} l_{i',j'} \frac{\partial G_{i,i',j'}}{\partial n} \right) \right], & i \neq i', \end{cases} \quad (3.37)$$

Through this procedure we obtain a linear system of equations for $\hat{\psi}_k$ as

$$S \hat{\psi}_k = \underline{m}. \quad (3.38)$$

The matrix S is fully occupied due to the non-local nature of the boundary conditions and vector $\underline{m} = \underline{m}^1 + \underline{m}^2$ contains the right hand side of (3.25). This concludes the numerical computation of the in-plane components \hat{b}_{yk} and \hat{b}_{zk} , and it remains to evaluate the streamwise component \hat{b}_{xk} which will be discussed next.

In principle, the streamwise Fourier coefficient \hat{b}_{xk} can be computed from the discrete form of the induction equation in k -space (3.12), with the Dirichlet condition $\hat{b}_{xk} = -i\alpha_k \hat{\psi}_k$ on the boundary Γ . However this raises the issue of preserving the divergence of the magnetic field ($\nabla \cdot \mathbf{b} = 0$) during the course of its evolution, due to the reason that equations (2.14) and (2.16) form an overdetermined system for the \mathbf{b} field. Maintaining $\nabla \cdot \mathbf{b} = 0$ numerically is a non-trivial issue and various strategies are often adopted to ensure solenoidality (see Tóth [2000] for a detailed discussion). The issue becomes even more challenging when a semi-implicit or a fully implicit procedure is used for the magnetic field along with non-local boundary conditions. The numerical source of generation of $\nabla \cdot \mathbf{b}$ can be understood as follows. Taking the divergence of (3.10) and rearranging the terms gives

$$D^{n+1} = \frac{1}{f} \nabla^2 D^{n+1} + D_q, \quad (3.39)$$

where $D^{n+1} = \nabla \cdot \mathbf{b}^{n+1}$ and $D_q = \nabla \cdot \mathbf{q}$. Although the initial fields \mathbf{v}^n and \mathbf{b}^n are divergence-free (hence the last term on the right hand side vanishes), the boundary conditions act as a source of D^{n+1} during the solution of the Poisson equation for D^{n+1} . This contaminates D^{n+1} on the interior points adjacent to the boundary and the divergence diffuses into the domain interior subsequently.

In order to preserve the solenoidality of the magnetic field, the streamwise component \hat{b}_{xk} is reconstructed from the in-plane components using

$$\hat{b}_{xk} = \frac{-1}{i\alpha_k} \left(\frac{\partial \hat{b}_{yk}}{\partial y} + \frac{\partial \hat{b}_{zk}}{\partial z} \right), \text{ for wavenumbers } k \neq 0. \quad (3.40)$$

This ensures a divergence-free magnetic field for all the non-zero Fourier modes.

3.2.3 Treatment of the zero mode ($k = 0$)

The reconstruction of b_x is however not possible for the zero mode due to the reason that when $k = 0$, the streamwise mean component \bar{b}_x is decoupled from the in-plane mean components \bar{b}_y and \bar{b}_z , where the overbar denotes averaging with respect to x . Hence we solve (3.12) for the mean component \bar{b}_x which can be written as

$$-f\bar{b}_x + \nabla_{yz}^2 \bar{b}_x = -f\bar{q}_x. \quad (3.41)$$

The boundary condition for this is obtained again from $\nabla \times \bar{\mathbf{b}} = 0$ which leads to the Dirichlet condition $\bar{b}_x = \text{constant}$ and the constant can be conveniently chosen to be zero,

$$\bar{b}_x = 0. \quad (3.42)$$

The discrete form of (3.41) is solved with the Dirichlet boundary condition using the Poisson solver similar to that of pressure.

Since reconstruction of \bar{b}_x is not possible when $k = 0$, satisfying $\nabla \cdot \bar{\mathbf{b}} = 0$ is not guaranteed with the usage of primitive variables. Therefore the mean in-plane components \bar{b}_y and \bar{b}_z are computed through the magnetic vector potential A which is defined by

$$\bar{b}_y = \frac{\partial A}{\partial z}, \quad \bar{b}_z = -\frac{\partial A}{\partial y}. \quad (3.43)$$

The governing equation for A is derived as follows. Averaging equation (2.14) along the x -direction and rewriting the advective and field stretching terms in the curl form gives

$$\frac{\partial \bar{\mathbf{b}}}{\partial t} = \overline{\nabla \times (\mathbf{v} \times \mathbf{b}_t)} + \frac{1}{R_m} \nabla_{yz}^2 \bar{\mathbf{b}}. \quad (3.44)$$

Further simplification yields the mean equations for the in-plane components as

$$\frac{\partial \bar{b}_y}{\partial t} = \frac{\partial}{\partial z} (\overline{v_y b_{zt} - b_{yt} v_z}) + \frac{1}{R_m} \nabla_{yz}^2 \bar{b}_y, \quad (3.45)$$

$$\frac{\partial \bar{b}_z}{\partial t} = -\frac{\partial}{\partial y} (\overline{v_y b_{zt} - b_{yt} v_z}) + \frac{1}{R_m} \nabla_{yz}^2 \bar{b}_z. \quad (3.46)$$

3. Numerical Procedure

Introducing the vector potential and integrating yields the following governing equation for A in the interior

$$\frac{\partial A}{\partial t} = \overline{v_y b_{zt} - b_{yt} v_z} + \frac{1}{R_m} \left(\frac{\partial^2 A}{\partial y^2} + \frac{\partial^2 A}{\partial z^2} \right) + \zeta(t), \quad (3.47)$$

where $\zeta(t)$ is a constant of integration that depends only on time.

In the exterior, $\overline{\nabla \times \mathbf{b}} = 0$ yields

$$\frac{\partial^2 A}{\partial y^2} + \frac{\partial^2 A}{\partial z^2} = 0, \quad (3.48)$$

for which the corresponding boundary integral form can be written as

$$\beta(\mathbf{r}') A(\mathbf{r}') = \text{P.V.} \oint_{\Gamma} [G_0(\mathbf{r}', \mathbf{r}) \frac{\partial A}{\partial n}(\mathbf{r}) + A(\mathbf{r}) \frac{\partial G_0}{\partial n}(\mathbf{r}', \mathbf{r})] dl(\mathbf{r}), \quad (3.49)$$

similar to equation (3.18), which is used as the boundary condition to solve (3.47). The constant $\zeta(t)$ is determined by integrating (3.48) in the exterior and applying the Gauss-divergence theorem to obtain the following constraint for A on Γ

$$\oint_{\Gamma} \frac{\partial A}{\partial n} dl = 0. \quad (3.50)$$

The above equation implies that the net mean streamwise current is zero. Equations (3.43), (3.47), (3.49) and (3.50) form the closure for the problem of computing the x -averaged in-plane components \bar{b}_y and \bar{b}_z .

The Fourier coefficient components \hat{b}_{xk} , \hat{b}_{yk} and \hat{b}_{zk} obtained for $k = 0, 1, 2, \dots, N_x/2 - 1$ are transformed back to the real space using an inverse FFT operation, which completes the computation of the secondary magnetic field evolution at a given time step. The \mathbf{b} field obtained is used to compute the \mathbf{j} field according to (2.17) and subsequently the Lorentz force term $\mathbf{j} \times \mathbf{b}_t$ in the momentum balance (2.13) for the computation of the velocity field at the next time step. The computational procedure described here is conducive for easy parallelization due to the fact that the numerical scheme is based on solution in the Fourier space. The computation of the Fourier coefficients in the k -space can be performed independently by distributing the k -modes among several processors. Our particular implementation of this numerical procedure for the solution of the induction equation with the integral boundary conditions was done through a FORTRAN code with hybrid MPI-OpenMP parallelization, starting with an existing quasistatic MHD code DUCAT (Krasnov *et al.* [2011]).

3.3 Verification and comparative study

Verification of the implementation of the numerical procedure has been performed at various levels, which are described in this section.

3.3.1 Verification of BEM implementation with analytical solution

At first, the specific implementation of the boundary element method (as a standalone problem) for the Fredholm integral equation (3.18) on a rectangular boundary is verified by comparing the numerical solution obtained so with a suitable analytical solution. In other words, it is intended to test if, given a function $\partial\hat{\psi}_k/\partial n$ on the rectangular boundary, the numerical solution using BEM produces the correct solution for $\hat{\psi}$. The idea here is to choose the known free space function $K_0(r)$ (r being the absolute distance from the centroid of the rectangle) and force the condition $\partial\hat{\psi}_k/\partial n = \partial K_0(r)/\partial n$. Now, since $\hat{\psi}_k$ itself satisfies the far field condition ($\hat{\psi}_k(r) \rightarrow 0$ as $r \rightarrow \infty$), ideally the numerical solution for $\hat{\psi}_k$ on the rectangular boundary must yield the free space function itself. This is tested by computing the numerical solution of (3.18) on a square boundary with grid sizes ranging from 32 grid points per edge to 512 grid points per edge. A typical comparison of the numerical solution to the analytical function is shown in Fig. 3.3.

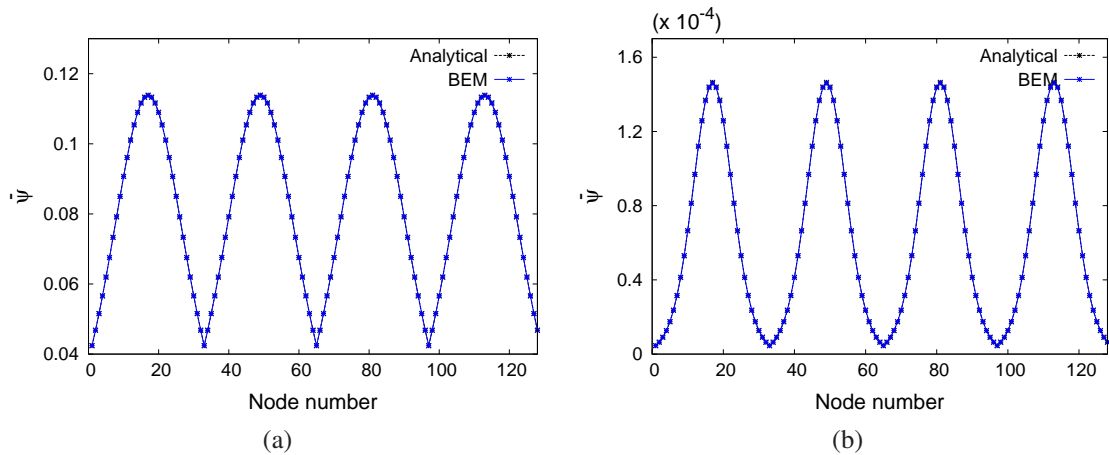


Figure 3.3: Magnetic potential $\hat{\psi}_k$ along the rectangular contour for wavenumbers a) $\alpha_k = 2.0$ and b) $\alpha_k = 8.0$. Node number runs clockwise starting from the bottom left corner. Grid: 32 elements/edge with a stretch factor of 2.0.

It can be seen that very accurate solutions are obtained even with a course grid of 32 elements per edge. This clearly shows that the numerical solution of (3.18) performed using BEM is consistent with the governing Helmholtz equation for $\hat{\psi}_k$ along with the far field condition.

3.3.2 Convergence of the coupled FD-BEM iterative procedure

It is important to ensure proper convergence of the coupled iterative scheme described in the previous section, that is used to numerically solve the Poisson equations for the components \hat{b}_{yk} and \hat{b}_{zk} in the interior along with the integral boundary conditions, at each time step of the DNS. For this purpose, the two-dimensional problem of expulsion of magnetic flux by a single rotating eddy in a square geometry is chosen. This problem dates back to Weiss [1966] when it was first studied numerically in the context of astrophysical MHD. The original problem setup consists of a two-dimensional square domain (in the y - z plane) with a uniform vertical magnetic field ($\mathbf{B} = B_0 \hat{\mathbf{k}}$) in the initial state (at $t = 0$), upon which a single conducting eddy is imposed to observe how the magnetic field undergoes twisting and reconnections leading to the final steady state. The idea is that, at high R_m the magnetic flux is expected to be expelled in most part of the domain due to the fact that flux cannot exist within the closed streamlines of an electrically conducting fluid. The problem is purely kinematic in the sense that the flow is assumed to be unaffected by the evolving magnetic field. The time-invariant velocity field of the eddy is represented by the streamfunction

$$\phi(y, z) = \frac{-1}{\pi} (1 - 4z^2)^4 \cos(\pi y), \quad (3.51)$$

the streamlines of which are shown in Fig. 3.4. The boundary conditions used by Weiss

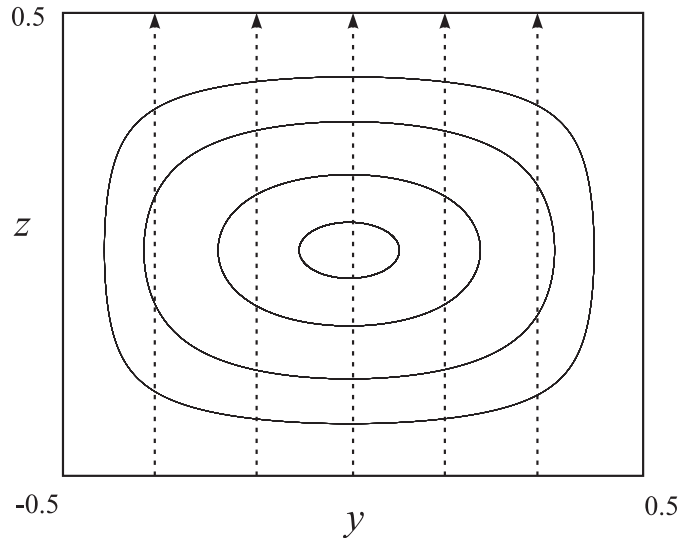


Figure 3.4: Two dimensional domain showing the velocity streamlines of the eddy (full lines) and the initial uniform magnetic field (dotted lines).

involved perfectly conducting top and bottom walls and mirror symmetry on the left and right walls. Both these conditions essentially lead to a vanishing normal component of the secondary magnetic field at the boundary, which are hereafter called idealized boundary conditions. The governing equation for the evolution of the secondary magnetic field $\mathbf{b}(y, z, t)$ and the corresponding boundary conditions can be summarized in the non-dimensional form as

$$\frac{\partial \mathbf{b}}{\partial t} = \nabla \times (\mathbf{v} \times \mathbf{b}_t) + \frac{1}{R_m} \nabla^2 \mathbf{b}, \quad (3.52)$$

$$\nabla \cdot \mathbf{b} = 0, \quad (3.53)$$

$$b_y(-0.5, z) = b_y(0.5, z) = b_z(y, -0.5) = b_z(y, 0.5) = 0. \quad (3.54)$$

As a first step, the above equations were numerically solved using second-order finite differences, which yielded results very similar to that of Weiss' as can be seen from the steady state magnetic field lines shown in Fig. 3.5. It must be noted here that there are no quantitative results available from Weiss and hence only a visual comparison is possible. Furthermore, the time dependent reconnection sequences leading to the expelled steady state were also observed to match very closely to that of Weiss', the details of which are not being shown here for the sake of brevity.

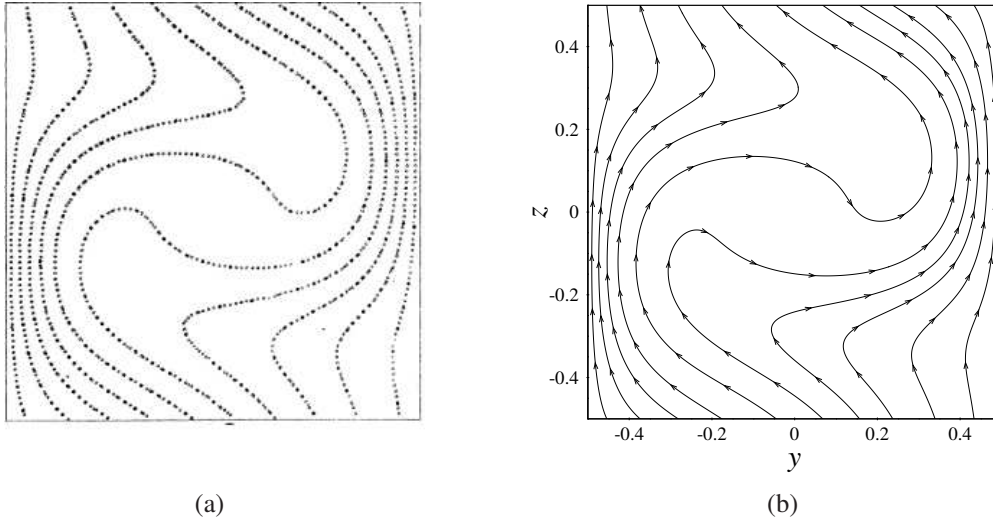


Figure 3.5: Magnetic field lines in the steady state for $R_m = 40$ obtained by a) Weiss (1966) and b) the present simulation.

In the next step, the idealized boundary conditions are replaced by integral boundary conditions and the iterative procedure is used to solve the system numerically. Fastest convergence rates were obtained when the updates of the solution variable is performed in the form of concentric squares starting from the middle of the domain

3. Numerical Procedure

and going outward towards the boundary and back. Figure. 3.6 shows the final state for the case of $R_m = 80$.

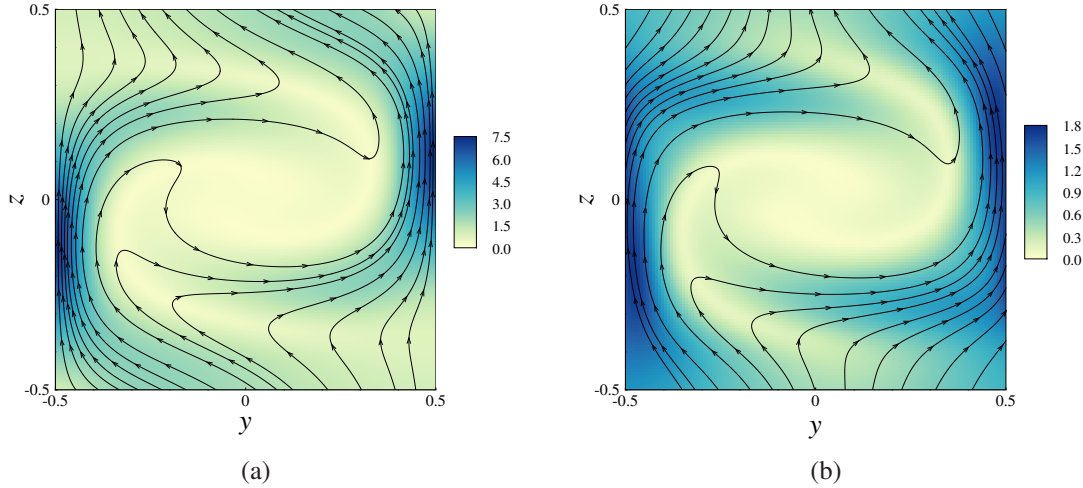


Figure 3.6: Steady state magnetic field lines for $R_m = 80$ obtained using a) idealized boundary conditions and b) fully consistent integral boundary conditions. Contours are colored by the total magnetic field magnitude $|\mathbf{b}_r|$.

One can clearly observe significant differences in both the cases. Apart from different field line slopes near the boundaries (where the flux is non-negligible), with the integral boundary conditions, a more realistic expulsion scenario is observed unlike the case of ideal boundary conditions where a huge piling up of magnetic field occurs near the boundaries. This can be readily seen from the upper limits of the contour scales. This is a first indication that a consistent treatment of magnetic boundary conditions might have significant effects on the overall solution.

Although the solution of this problem involves the boundary integral equation corresponding to the Laplace equation (special case of the Helmholtz equation for $k = 0$) in the exterior and the interior problem is formulated using the magnetic streamfunction, this case points to several useful conclusions regarding the iterative procedure. Firstly, the procedure shows very good convergence at various values of the magnetic Reynolds number (upto $R_m = 1000$ was tested). Further, iterative updates in cyclical pattern going in concentric squares significantly accelerates the rate of convergence.

3.3.3 Verification in the limiting case of low R_m

An ideal verification of the implementation of the computational procedure described in the previous section would involve comparison of numerical results at $R_m \sim 1$ and higher obtained from this procedure to those obtained using a full MHD numerical code that solves for the magnetic field on a grid covering an extended domain.

However, since this is not possible, we limit our scope rather to verification of the computational procedure in the quasistatic limit. In this section, we present results for the case when the magnetic Reynolds number is low i.e. $R_m \ll 1$ that aid as a verification of the implementation of the numerical procedure. As described in chapter 2, it is customary to describe magnetohydrodynamics at low R_m with the quasistatic or inductionless approximation. This will be referred as QS formulation hereafter. For easy reference, the QS formulation is briefly summarized below as

$$\mathbf{j} = -\nabla\phi + (\mathbf{v} \times \mathbf{b}_0), \quad (3.55)$$

$$\nabla^2\phi = \nabla \cdot (\mathbf{v} \times \mathbf{b}_0) \quad \text{Boundary condition: } \frac{\partial\phi}{\partial n} = 0, \quad (3.56)$$

$$\mathbf{f}_L = \frac{Ha^2}{Re} (\mathbf{j} \times \mathbf{b}_0), \quad (3.57)$$

where \mathbf{f}_L is the Lorentz force source term in the Navier-Stokes equation (2.13) and the boundary condition corresponds to perfectly insulating walls. An alternative formulation of the quasistatic approximation is the induced electric current based formulation that uses the current density \mathbf{j} as the primary variable instead of the electric potential ϕ (see Smolentsev *et al.* [2010]).

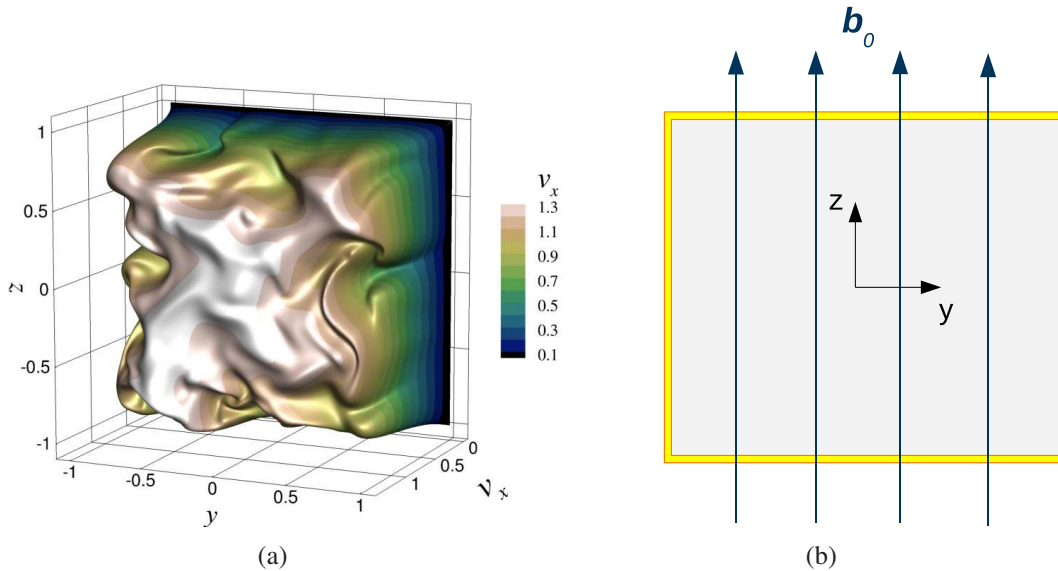


Figure 3.7: (a) Contour of the x -component of the initial turbulent velocity field at $Re = 2000$ and (b) imposed magnetic field $\mathbf{b}_0 = b_0\mathbf{k}$, shown at the cross-section $x = L_x/2$; $Ha = 15$.

Furthermore, when R_m is low, the secondary magnetic field is nevertheless finite and its evolution can be described by another formulation of the quasistatic approximation based on the induced magnetic field rather than on the electric potential. This is the so-called quasistationary formulation (referred to as QST formulation hereafter).

3. Numerical Procedure

The QST formulation can be obtained as follows. Approximating the electromagnetic fields by $\varpi = \varpi^0 + \varepsilon \varpi^1$ where $\varepsilon = R_m$ is considered to be a small value and $\varpi = [\mathbf{b}, \mathbf{e}, \mathbf{j}]$ denoting the magnetic, electric and the current density fields respectively, the induction equation can be rewritten as

$$\varepsilon \frac{\partial}{\partial t} (\mathbf{b}^0 + \varepsilon \mathbf{b}^1) = \varepsilon \nabla \times (\mathbf{v} \times (\mathbf{b}^0 + \varepsilon \mathbf{b}^1)) + \nabla^2 (\mathbf{b}^0 + \varepsilon \mathbf{b}^1). \quad (3.58)$$

Equating terms of the same order of ε and assuming the imposed magnetic field \mathbf{b}^0 to be time-independent, we obtain

$$\nabla^2 \mathbf{b}^1 = (\mathbf{v} \cdot \nabla) \mathbf{b}^0 - (\mathbf{b}^0 \cdot \nabla) \mathbf{v}, \quad \mathbf{j}^1 = \nabla \times \mathbf{b}^1, \quad (3.59)$$

with the same integral wall boundary conditions for the magnetic field as described in the previous sections. Through (3.59), the magnetic field is parametrically dependent on time and evolves as a passive vector field that depends on the velocity field. It can be shown that $\nabla \times \mathbf{e}^1 = \partial \mathbf{b}^0 / \partial t = 0$, making the electric field expressible as $\mathbf{e}^1 = -\nabla \phi$, through which the exact equivalence between the QS and QST formulations is established (see Boeck [2010]). Due to this equivalence, the current densities \mathbf{j} computed by the QS formulation and the resulting secondary magnetic field must match with those computed by the QST formulation.

In the particular case that we consider, a uniform magnetic field along the z -direction is imposed on a fully turbulent 3D velocity field at $Re = 2000$ (see Fig. 3.7) in a duct of length $L_x = 4\pi$ and a square cross-section $L_y = L_z = 2$ and the numerical computation is performed for a single time step with both the QS and the QST procedures. A grid resolution of 256^3 is used for this computation. In order to perform the inductionless computations, the quasistatic MHD code DUCAT (DNS code based on finite differences) was used which has been extensively validated (see Krasnov *et al.* [2011]). The resulting components of current densities from the two methods are compared at a particular cross section ($x = L_x/2$) as shown in Fig. 3.8(a) and (b) and a close match between the two methods is observed. However, it must be mentioned that a good agreement of current densities is only a necessary requirement for the correctness of the quasistationary procedure with BEM but not a sufficient one. This is attributed to the fact that in the case of low magnetic Reynolds number, when $j_n = 0$ is ensured on the wall, the current density field \mathbf{j} in the interior is uniquely determined. Due to this reason, the current densities will match even if a simplified approach, the so-called pseudo-vacuum magnetic boundary conditions (explained in the next subsection), are applied to the quasistationary formulation. This is shown in Fig. 3.8(c), where the component j_z shows a good agreement between the QS, QST and the QST

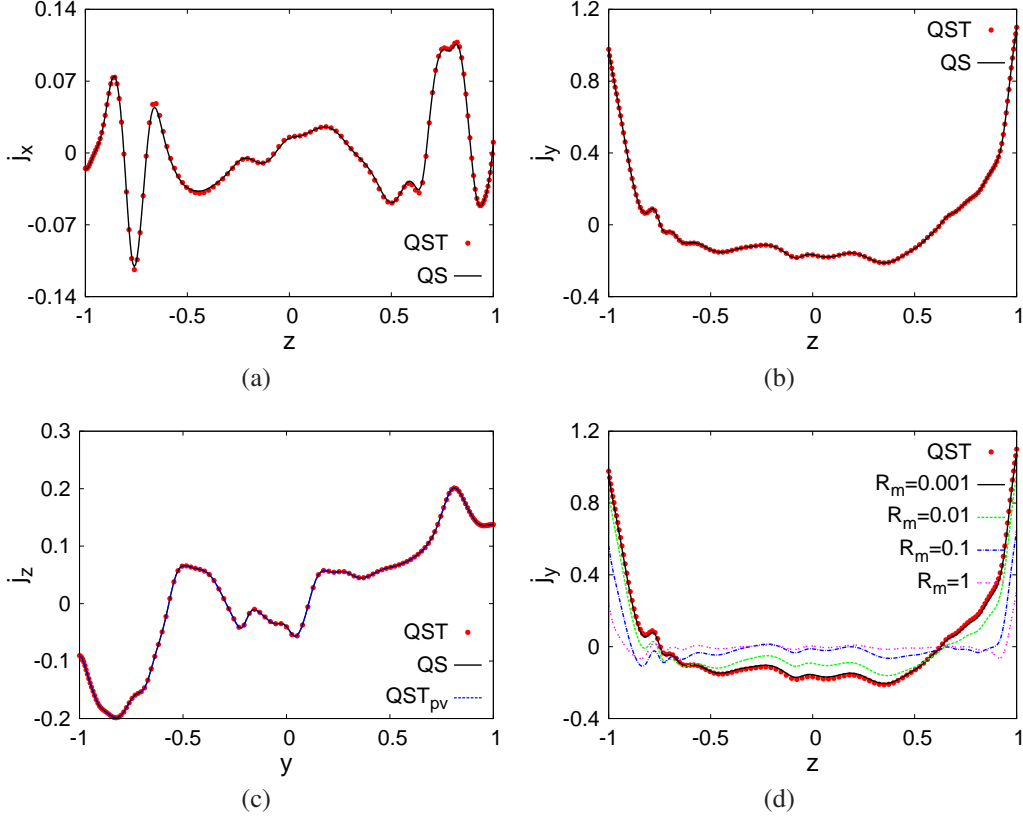


Figure 3.8: Current density components plotted at the cross-section $x = L_x/2$. (a) j_x and (b) j_y along the line $y = 0$; (c) j_z along the line $z = -0.5$; (d) j_y from full MHD. Grid: $256 \times 256 \times 256$, $Re = 2000$, $Ha = 15$.

with pseudo-vacuum BCs which is denoted as QST_{pv} in the legend. A proof for the uniqueness of \mathbf{j} in the case of $j_n = 0$ is provided in Appendix A.

Of particular interest is the order of R_m at which the validity of the quasistatic approximation really holds. For this purpose, the full MHD system (the induction equation) with the integral boundary conditions was used to compute the \mathbf{b} field for a single time step at various orders of R_m . The resulting current component j_y is compared with that obtained from the QST formulation. It can be seen (from Fig. 3.8(d)) that a convergence to the quasistatic limit occurs when $R_m \sim 10^{-3}$.

To complement the verification, a comparison is made for the secondary magnetic field in the exterior of the duct. Therefore, the current density field \mathbf{j} obtained from the quasistatic computation is used to compute the secondary magnetic field in the duct exterior through the Biot-Savart law

$$\mathbf{b}(\mathbf{r}') = \frac{1}{4\pi} \int \frac{\mathbf{j}(\mathbf{r}) \times (\mathbf{r}' - \mathbf{r}) dV}{(|\mathbf{r}' - \mathbf{r}|)^3}, \quad (3.60)$$

which is evaluated numerically using a trapezoidal quadrature. The corresponding

3. Numerical Procedure

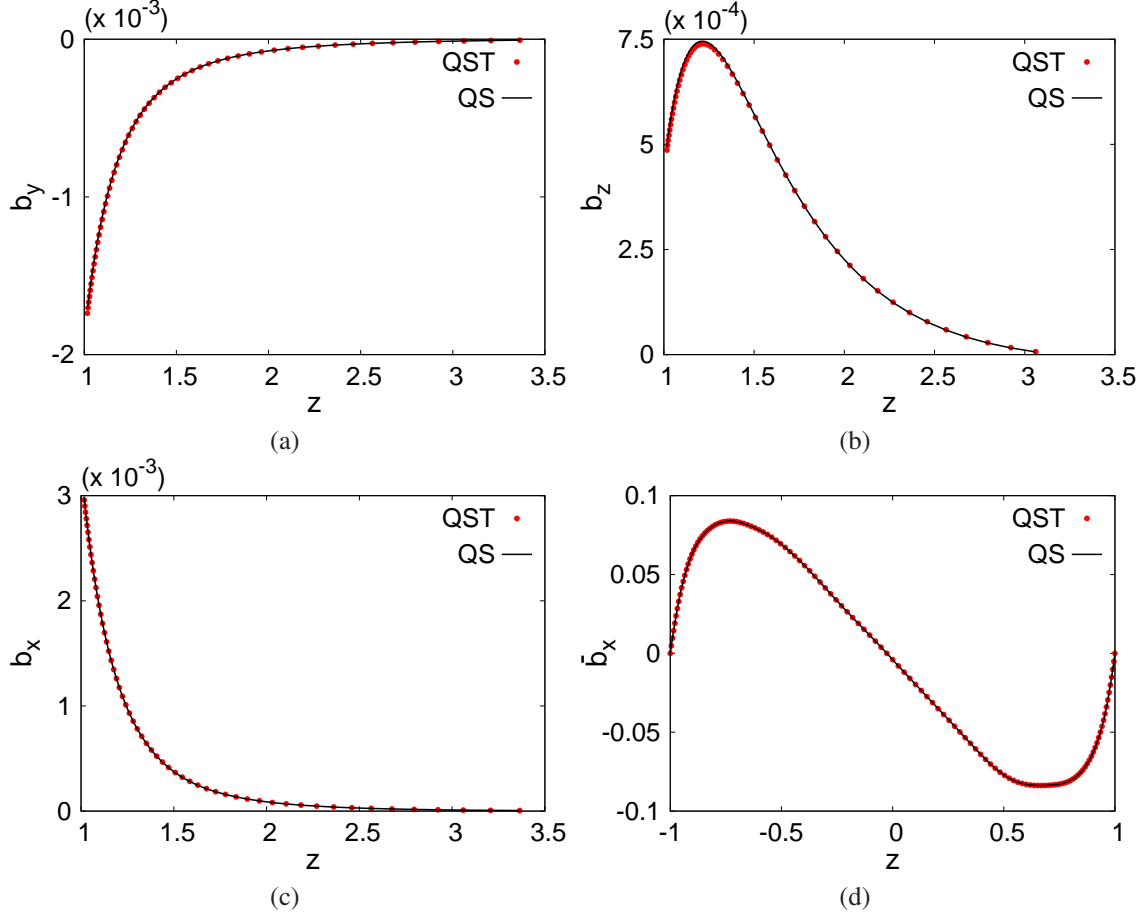


Figure 3.9: Secondary magnetic field components in the exterior (a) b_y , (b) b_z and (c) non-zero modes of b_x ($k \neq 0$), at the streamwise location $x = L_x/2$. The exterior corresponds to $z > 1$. (d) Mean streamwise component of the secondary magnetic field b_x ($k = 0$) in the interior of the duct; Grid: $256 \times 256 \times 256$, $Re = 2000$, $Ha = 15$.

magnetic field from the quasistationary computation is obtained by evaluating the scalar potential $\hat{\psi}_k$ in the duct exterior using equation (3.18) from the known values of $\hat{\psi}_k$ and \hat{b}_{nk} at the boundary but with $\beta(\mathbf{r}') = 1$. A comparison of the exterior field components b_y and b_z along the line $y = 0$, $z > 1$ is shown in Fig. 3.9(a) and (b) respectively.

The streamwise component b_x is decomposed into $b_x(k \neq 0)$ and $b_x(k = 0)$ that contain the non-zero modes and the zero mode respectively for which the comparison is shown in Fig. 3.9(c) and (d). Since the mean component \bar{b}_x vanishes in the exterior, its comparison is made only in the interior of the duct. This concludes the verification of the numerical procedure adopted to model the magnetic boundary conditions for the induction equation.

3.3.4 Comparison with pseudo-vacuum boundary conditions

As mentioned in section 3.1, finite/high R_m MHD simulations are often conducted using the so-called pseudo-vacuum magnetic boundary conditions, which can be summarized as below,

$$\text{Pseudo-vacuum BCs : } \mathbf{b}_{\parallel} = 0, \frac{\partial b_n}{\partial n} = 0 \text{ at } y, z = \pm 1, \quad (3.61)$$

where the subscript \parallel refers to the two wall tangential directions. This formulation

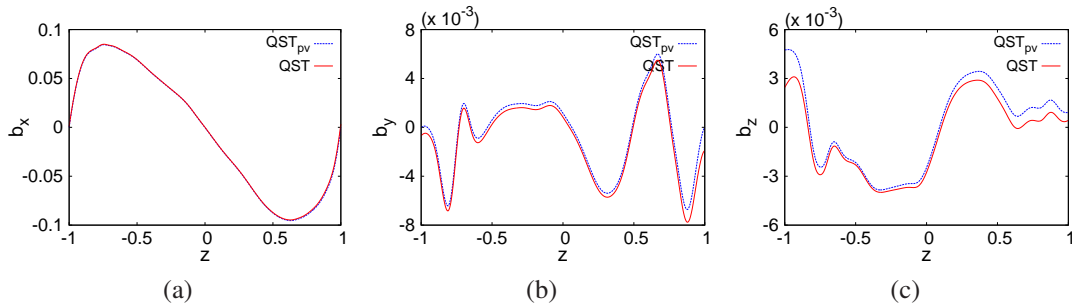


Figure 3.10: Secondary magnetic field components (a) b_x (b) b_y and (c) b_z along the line $y = 0$ on the cross-sectional plane $x = L_x/2$; Grid: $256 \times 256 \times 256$, $Re = 2000$, $Ha = 15$.

achieves vanishing wall normal currents j_n through the assumption of zero tangential magnetic field, a trivial solution of $(\nabla \times \mathbf{b}_{wall}) \cdot \mathbf{n} = 0$, and leads to considerable simplification of the computational procedure. However, numerical solutions obtained with this simplified model can result in significant loss of accuracy in the near wall velocity and magnetic fields. This becomes particularly important for wall-bounded MHD flows at transitional regimes, since instabilities are triggered in the thin boundary layers (either Shercliff layers that appear near the walls parallel to the magnetic field or Hartmann layers that appear near the walls perpendicular to the magnetic field). Here, differences that arise using the pseudo-vacuum conditions are quantified for the case of low R_m . In Fig. 3.10 magnetic field components in the duct interior computed using the boundary integral procedure are compared to those computed using the pseudo-vacuum conditions.

It is observed that the primary streamwise magnetic field component b_x matches very well. However the secondary components b_y and b_z show significant differences (especially near the walls) in both the cases. In this particular case of low R_m , the Lorentz force being proportional to $\mathbf{j} \times \mathbf{b}_0$, these differences do not impact the flow field. However, at finite/high R_m , the effect of these differences on the velocity field can be significant.

3.4 Explicit procedure for the induction equation

As described earlier, the semi-implicit numerical procedure outlined in section 3.2 requires at every time step, the solution of a Poisson equation each for \hat{b}_{yk} and \hat{b}_{zk} in the strict interior of the domain, together with the boundary integral equation. The discrete linear systems arising out of the two Poisson equations and the integral equation is sparse to most extent and reasonably occupied for the rest. There are no known fast solvers available to solve such linear systems, due to which it was preferred to use the coupled iterative procedure. However, the iterative procedure is sometimes not estimated to be fast enough to perform DNS on larger grid sizes within reasonable time periods. Due to this, the explicit procedure can be very useful especially in cases when the R_m is higher, leading to faster DNS runtimes. Hence, such a procedure has also been implemented in the code. A brief outline of this procedure and some of its features are presented in this section.

An explicit treatment of all the source terms of the induction equation leads to

$$\frac{3\mathbf{b}^{i+1} - 4\mathbf{b}^i + \mathbf{b}^{i-1}}{2\Delta t} = - \left[2(\nabla \times \mathbf{e})^i - (\nabla \times \mathbf{e})^{i-1} \right], \quad (3.62)$$

where \mathbf{e} is the electric field given by $\mathbf{e} = \mathbf{j} - \mathbf{v} \times \mathbf{b}_t$ and i represents the time level. In addition, since the boundary normal component of $\nabla \times \mathbf{e}$ is continuous across the wall boundaries, the discrete form of the induction equation can be applied only for the normal component of the secondary magnetic field b_n as

$$\frac{3b_n^{i+1} - 4b_n^i + b_n^{i-1}}{2\Delta t} = - \left[2(\nabla \times \mathbf{e})_n^i - (\nabla \times \mathbf{e})_n^{i-1} \right]. \quad (3.63)$$

Transforming only b_n on the wall boundaries into the Fourier space and representing the Fourier coefficient by \hat{b}_{nk} , the discrete linear system of the boundary integral equation for each wavenumber k can be written as

$$\underline{S\hat{\psi}_k^{i+1}} = \underline{m}^{i+1}. \quad (3.64)$$

The tangential components are a function of $\hat{\psi}_k^{i+1}$ as

$$\hat{b}_{xk}^{i+1} = -i\alpha_k \hat{\psi}_k^{i+1}, \quad \hat{b}_{\tau k}^{i+1} = -\frac{\partial \hat{\psi}_k^{i+1}}{\partial \tau}. \quad (3.65)$$

Solving equations (3.62), (3.63), (3.64) and (3.65) completes the computation of \mathbf{b} at each time step.

There are two main advantages in using this scheme. Firstly, the computation of

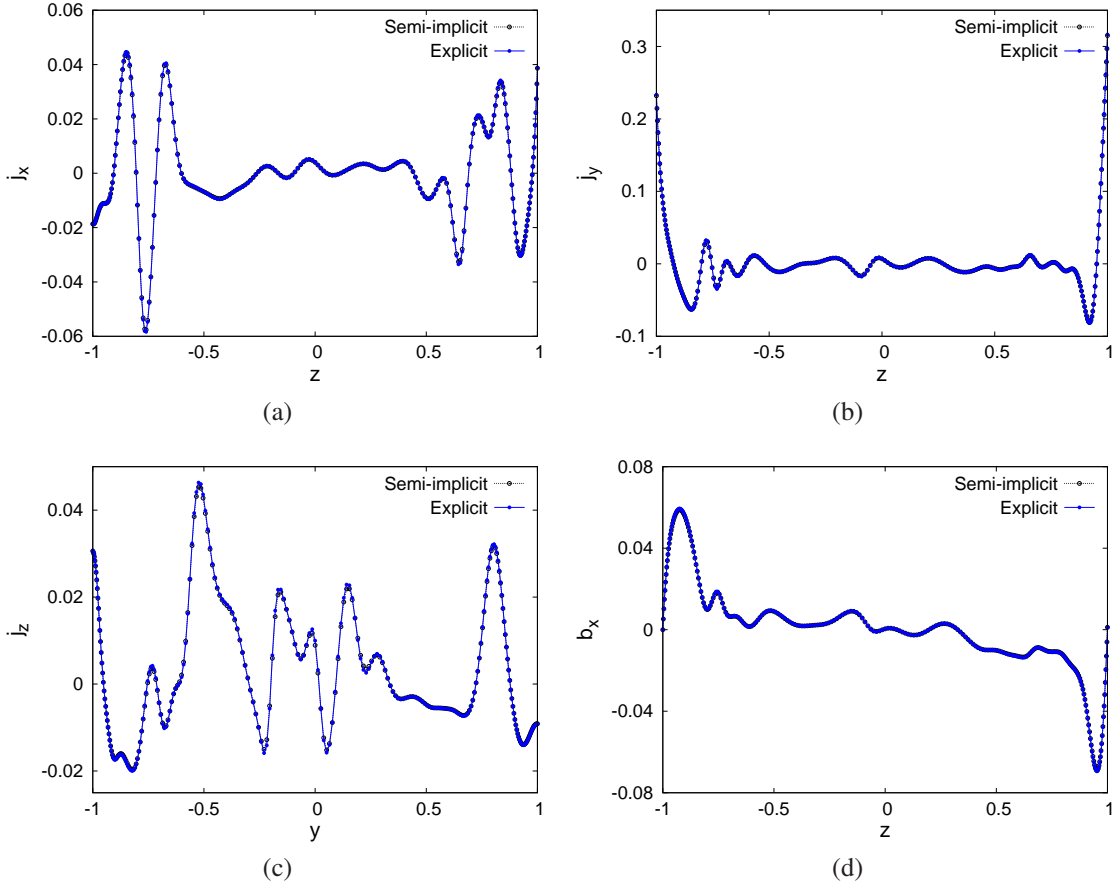


Figure 3.11: Current density field components a) j_x , b) j_y , c) j_z and the d) secondary magnetic field component b_x along the line $y = 0$ on the cross-sectional plane $x = L_x/2$; Grid: $256 \times 256 \times 256$, $Re = 2000$, $Ha = 15$, $R_m = 10$.

\mathbf{b} in the strict interior is decoupled from the boundary integral equation. Due to this, the computation time per time step is much smaller, as the integral equation simplifies to the inversion of a much smaller fully occupied linear system of equations. The matrix inverse for each wavenumber k is precomputed and stored before the start of the simulation, which reduces the computation overhead at each time step to a simple matrix-vector multiplication ($S^{-1}\underline{m}^{i+1}$, S being known beforehand as it is a pure function of the geometry of the problem). In addition, since \mathbf{b} on the interior and b_n on the wall boundary are computed using equations (3.62) and (3.63) in the real space itself, the problem of zero-mode ($k = 0$) divergence does not arise at all. Due to this any special treatment of the zero-mode is obviated. However, the main disadvantage of this scheme is clearly the fact that a much lower integration time step is required (for numerical stability) when R_m is low. Only at much higher R_m can the shorter time per time step of the explicit scheme over weigh the effect of smaller time step width.

As a verification of the implementation of the explicit scheme in the code, a simple test was performed as follows. Starting with a statistically steady turbulent velocity

field in the duct (obtained from a hydrodynamic simulation), as the initial state, both the explicit and the semi-implicit versions of the code were run for the same amount of time (0.01 convective units) for the Hartmann case with the parameters $R_m = 10$, $Re = 2000$ and $Ha = 15$. The results obtained at the end were compared, some of which are shown in Fig. 3.11. Clearly, the equivalence of the results of both the schemes is confirmed.

3.5 Permeation of an exterior magnetic field into a conductor - finite R_m effects

When an external electric current source is switched on near the flow of a conducting fluid, the magnetic field due to the currents do not permeate the fluid instantaneously but take a finite time to ‘seep’ through. The time it takes for this process depends on R_m of the flow under consideration, higher the R_m the longer is this transient state. In the case of modelling low R_m flows, with the quasistatic approximation, one assumes that this proceeds instantaneously which is indeed the case. Hence the externally imposed magnetic field is assumed to be present throughout the flow from time $t = 0$. However, in finite R_m flows such an assumption is not realistic for obvious reasons. Here, the external magnetic field is initially present only on the flow boundaries and will be simultaneously distorted by the flow as it penetrates. In other words, the external magnetic field never manifests within the flow in its ‘original’ (as if there is no conductor) form. Taking this into account can become very important in the case of wall bounded MHD turbulence at finite R_m . The key point here is that when R_m is finite, the effect of the magnetic field is felt first only in the boundary layers and only subsequently (and gradually) the core region of the flow will ‘see’ the magnetic field. This affects the way turbulence evolves as compared to the scenario when the external field is assumed to be present throughout the flow in the initial state. Although statistically steady states might not be affected by this phenomenon, transition and flow instabilities can be very sensitive to this circumstance. This motivates to study the exact details of the transient process in rather simpler cases of a uniform magnetic field imposed on a stationary conducting bar and a laminar flow in a duct.

3.5.1 Pure diffusion into a stationary conducting bar

At first, the problem of a uniform magnetic field ($B_0 = B_0 \hat{k}$) from an external current source imposed on a stationary ($v = 0$) straight bar of square cross-section is considered. Choosing L as the half width and B_0 , $B_0/\mu_0 L$ and L^2/λ as the scales for the

magnetic field, current density and time, the non-dimensional form of the governing equations will be

$$\frac{\partial \mathbf{b}}{\partial t} = -\nabla \times \mathbf{j}, \nabla \cdot \mathbf{b} = 0, \quad (3.66)$$

$$\mathbf{j} = \nabla \times \mathbf{b}. \quad (3.67)$$

As is evident, there are no parameters involved in this problem. Furthermore, the problem is essentially two-dimensional due to the uniform magnetic field and there being no reason for any gradients of the field variables along the x -direction. Nevertheless, it is solved as a 3D problem with periodic boundary conditions in the x -direction. On the y and z boundaries, integral magnetic boundary conditions are used as detailed earlier in this chapter. Choosing consistent initial conditions for the magnetic field is very essential and is done as follows. The background field $\mathbf{b}_0 = \hat{k}$ in the initial state is considered to be present everywhere in the domain and the secondary magnetic field \mathbf{b} is set to ensure that the total magnetic field in the strict interior and the boundary normal component of the total magnetic field vanishes. This involves predetermining the tangential component of \mathbf{b} at time $t = 0$ using the boundary integral procedure. These initial conditions can be summarized as

$$\mathbf{b} = -\mathbf{b}_0 \text{ in } \Omega_i \text{ at } t = 0, \quad (3.68)$$

$$b_n = -b_{n0}, \psi = F(b_n), b_\tau = -\frac{\partial \psi}{\partial \tau} \text{ on } \Sigma \text{ at } t = 0, \quad (3.69)$$

where the function F represents the non-local relation of ψ on b_n . These initial conditions ensure that the total magnetic field is strictly tangential on the boundary as if the magnetic lines flow around the square cross-section from the bottom to the top (see Fig. 3.12(a)).

The governing equations are solved numerically using the explicit scheme outlined in the previous section on a cross-sectional grid size of 128×128 . It should be noted that only the mode $k = 0$ is relevant here and $b_x = j_y = j_z = 0$. Magnetic field lines in the cross-section at various instants during the diffusion process are shown in Fig. 3.12. The vertical component of the field diffuses gradually in the y -direction and in about $t \sim 1$ a steady state is reached with a uniform vertical magnetic field across the domain. Also, it is interesting to see how a large streamwise current density j_x on the surface at $t = 0$ (see Fig. 3.13(a)) leads to a secondary magnetic field that ensures that the net/total magnetic field is zero within the domain. In our case, the maximum current density on the boundary $|j_{x,t=0}|^{max} \sim 1073$. The streamwise currents diffuse into the domain (see Fig. 3.13) with a very quick decay in their magnitude and finally vanish

throughout the domain in the steady state with the magnetic field becoming curl-free.

3.5.2 Simultaneous advection-diffusion in a laminar duct flow

Here, we consider a similar problem as in the previous subsection, but with the uniform field being imposed on a fully developed laminar duct flow instead of a stationary conductor. This becomes the well known Hartmann duct flow but with the exception of a finite R_m . The full governing equations including the Navier-Stokes system are used here along with the initial magnetic conditions mentioned in the previous subsection. The parameters $Re = 4000$ and $R_m = 50$ are chosen for this study. As can be seen from Fig. 3.14, the streamwise velocity in the initial stages is affected only in the boundary layers (see Fig. 3.14(c)) with the core velocity still not yet decelerated. With time, the Lorentz forces diffuse, to start affecting the core flow leading to the final steady state with the steep Hartmann and Shercliff boundary layers. Correspondingly, the primary component of the secondary magnetic field b_x shows a peak before returning to the steady state with the maximum b_x in the Hartmann layers. This means that the field lines are stretched significantly to about $b_x \sim 5.3$ and subsequently relax back without showing any oscillatory behavior.

During the same time, the various configurations visited by the cross-sectional current density streamlines are shown in Fig. 3.15.

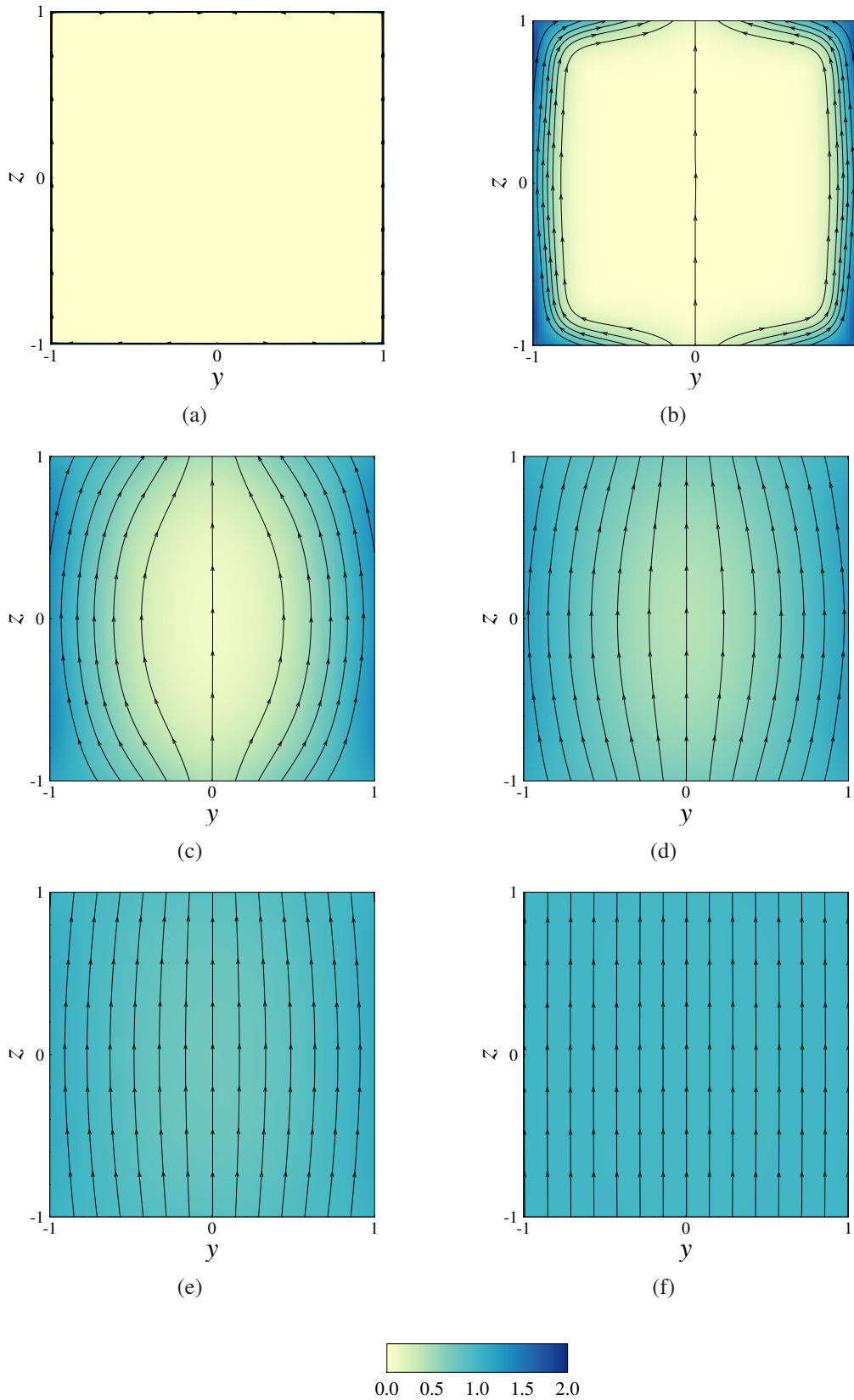


Figure 3.12: Streamlines of the total magnetic field in the cross-section at time a) $t = 0$, b) $t = 0.01$, c) $t = 0.1$, d) $t = 0.22$, e) $t = 0.4$ and f) $t = 1.0$; Contour coloring is done with respect to the magnitude of the magnetic field. $|\mathbf{B}|_{max}$ is out of the coloring bounds and is ≈ 6.76 for the first figure. Grid size in the plane: 128×128 .

3. Numerical Procedure

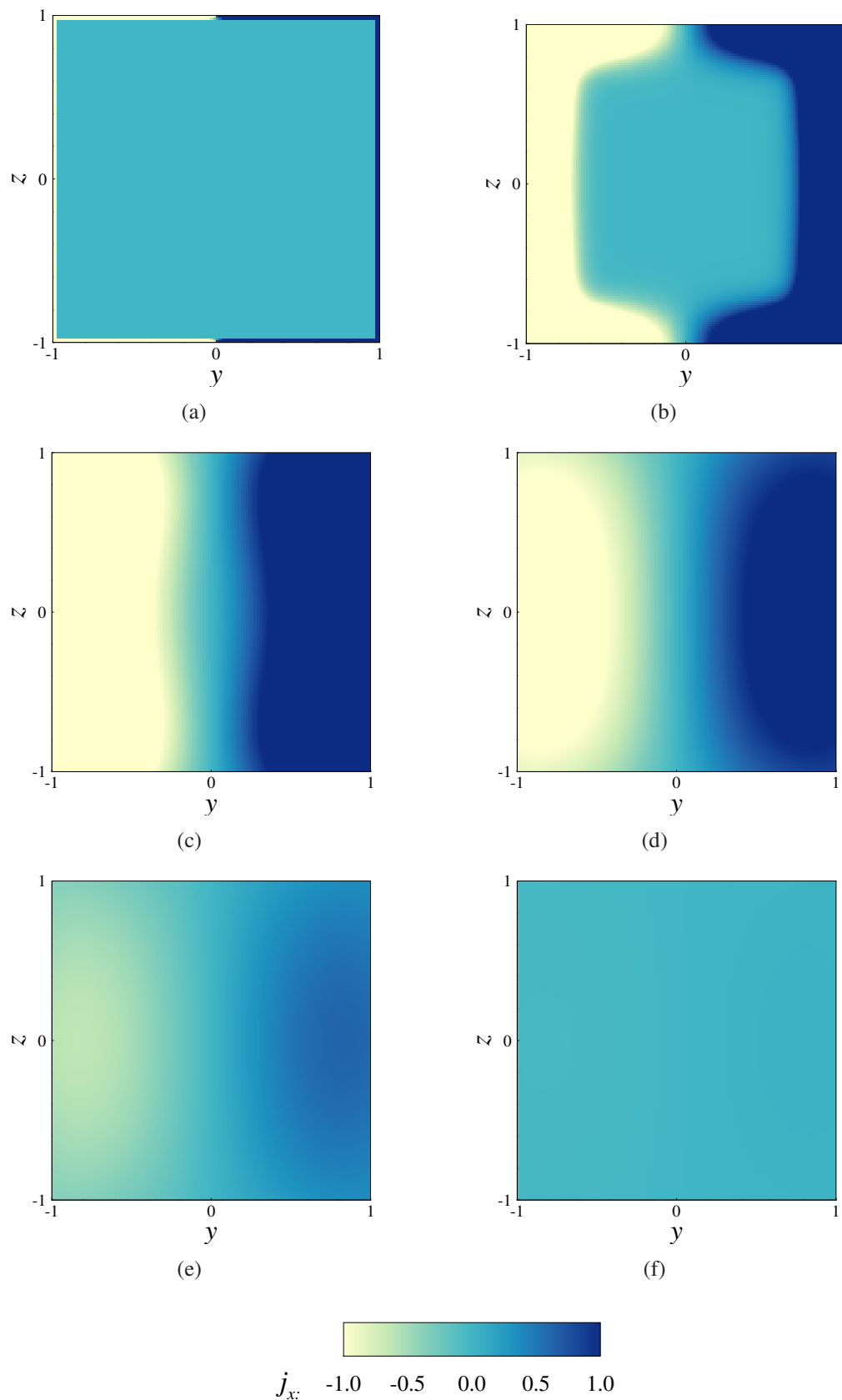


Figure 3.13: Cross sectional contour of the current density component j_x at time a) $t = 0$, b) $t = 0.01$, c) $t = 0.1$, d) $t = 0.22$, e) $t = 0.4$ and f) $t = 1.0$; $|j_{x,max}|$ is out of the coloring bounds and is 1073.0, 12.8, 2.5 and 1.4 respectively for the first four figures. Grid size in the plane: 128×128 .

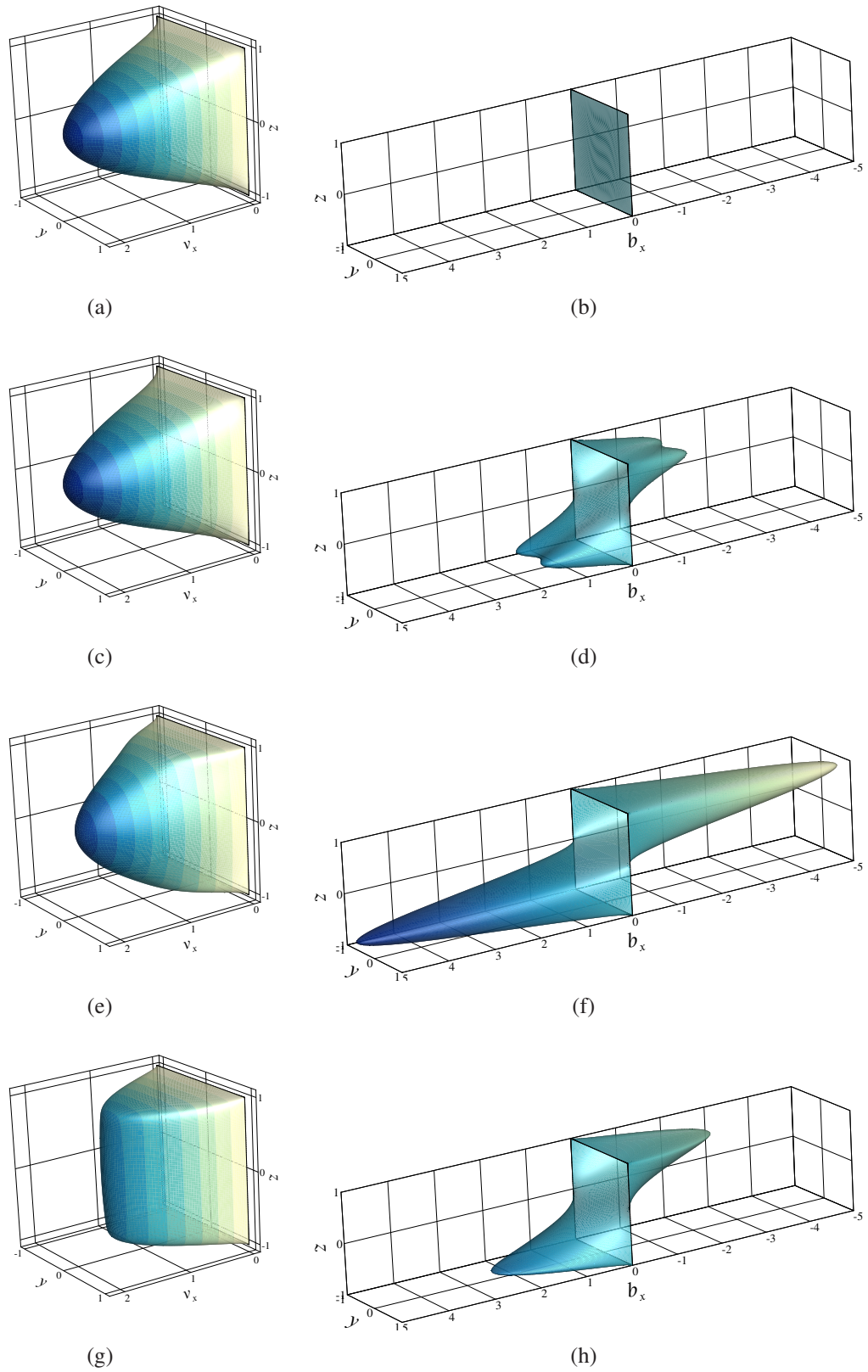


Figure 3.14: Contours of streamwise velocity v_x (left panel) and secondary magnetic field b_x (right panel) in the cross-section at time a),b) $t = 0$, c),d) $t = 5.7$, e),f) $t = 19.2$ and g),h) $t = 51.84$; Parameters are $R_m = 50$, $Re = 4000$ and $Ha = 25$; Grid size in the plane: 128×128 .

3. Numerical Procedure

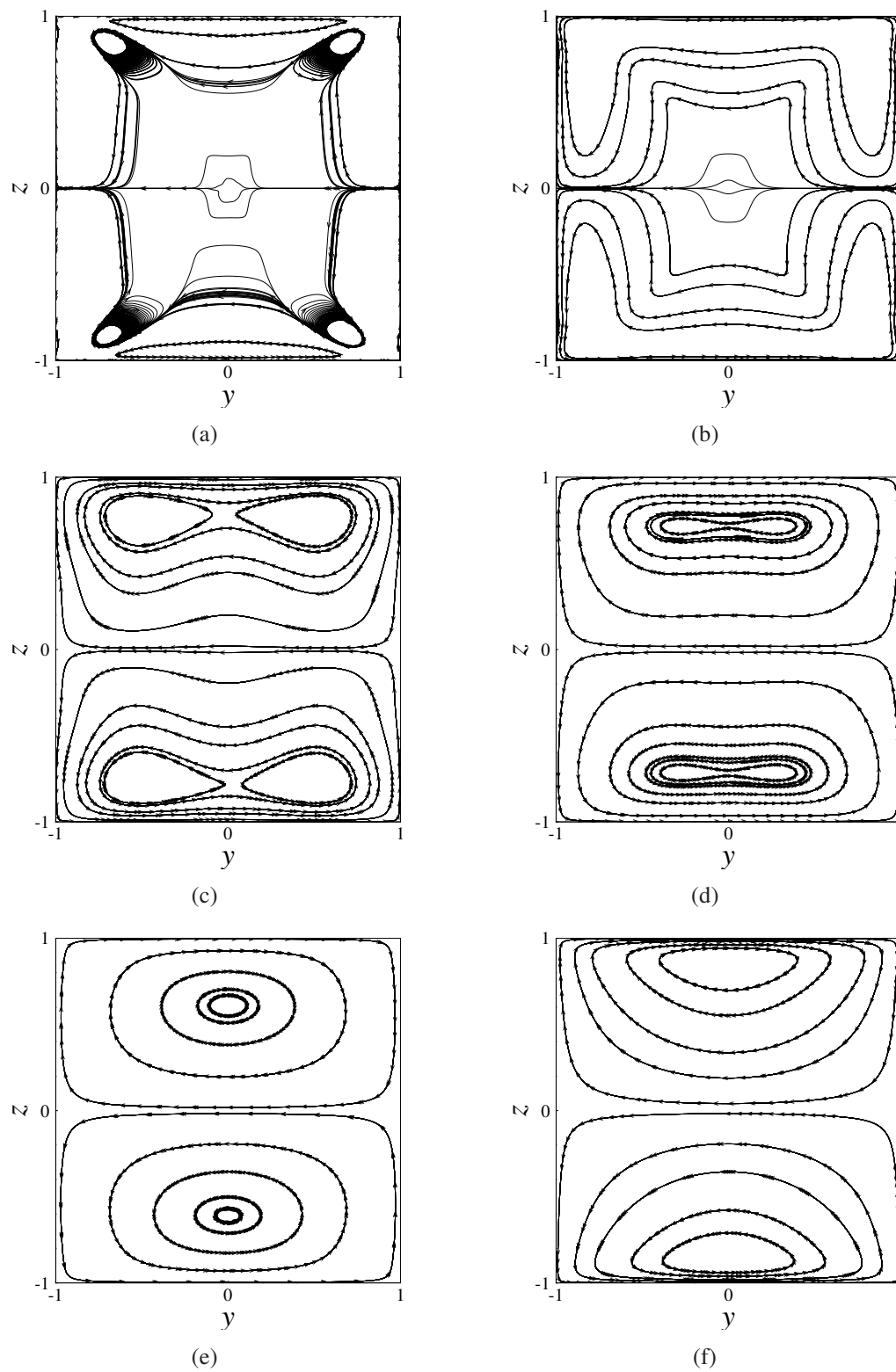


Figure 3.15: Streamlines of current density in the cross-section at time a) $t = 0.27$, b) $t = 0.81$, c) $t = 4.59$, d) $t = 7.56$, e) $t = 19.44$ and f) $t = 51.84$; Parameters are $R_m = 50$, $Re = 4000$ and $Ha = 25$; Grid size in the plane: 128×128 .

Chapter 4

Transient response of Lorentz force at finite magnetic Reynolds numbers

This chapter presents the study of the effect of magnetic Reynolds number on the time response of Lorentz force in a quickly accelerated solid conducting bar in the presence of a localized magnetic field. The results are compared with existing laboratory experiments on the subject.

4.1 Overview and problem setup

As mentioned in Chapter 1, finite R_m phenomena can occur not only due to large conductivities, length scales or velocities, but also due to relatively small advective time scales. This particular case is especially relevant in the context of LFV, where sudden changes in the fluid velocities can lead to finite R_m effects. Hence, it is important to understand the effects qualitatively and also to quantify finite R_m effects on Lorentz forces. This is done in this chapter by studying the problem in the simpler case of the motion of a solid conductor under an applied localized magnetic field. The configuration is based on recent experiments that were conducted by Sokolov *et al.* [2014] and hence wherever possible, comparison is made between the results of simulations and experiments.

The problem setup consists of a straight conducting bar of length 1 m and square cross-section upon which a strong magnetic field (up to 0.2 T) is imposed only on a short section of the bar. The magnetic field is produced by placing a set of six equisized permanent magnets of size 30 mm \times 30 mm \times 70 mm (three on either side of the bar) forming a linear Halbach array. The Halbach configuration is used so as to effectively channelize the resultant magnetic field from all the six magnets normal to the bar. The bar is accelerated very quickly from rest, along its length. Typical accelerations

4. Lorentz force transient response

considered here range from 0.4 m s^{-2} to 4 m s^{-2} . The setup is shown in Fig. 4.1, which is very similar to that of the experimental setup of Sokolov *et al.* [2014] except for the difference that rods of circular cross-section were used in the experiments.

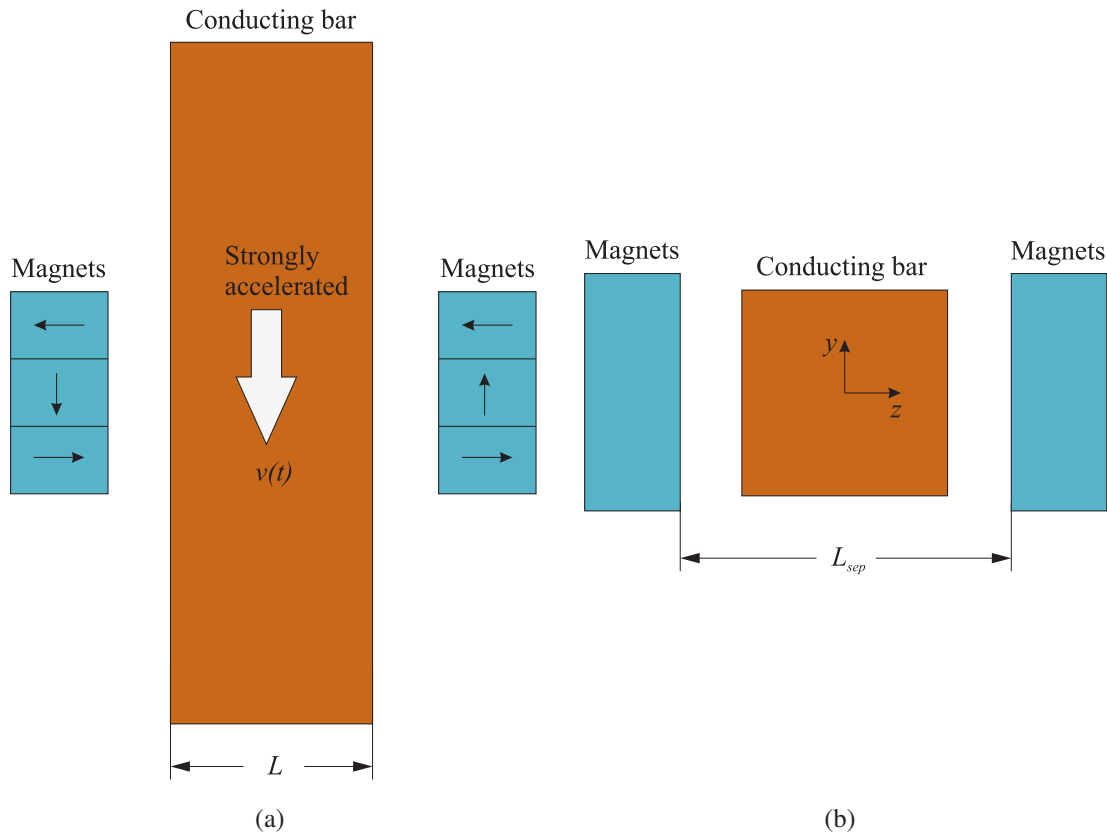


Figure 4.1: a) Schematic of the problem setup showing the strongly accelerated conducting bar with three magnets placed on either side forming a linear Halbach configuration. The black arrows indicate the direction of magnetization of the individual magnets. b) the top view of the same configuration.

A typical acceleration profile is shown in Fig. 4.2, that shows a rise in bar velocity from rest to $\approx 136 \text{ mm s}^{-1}$ in a time of $\approx 0.07 \text{ s}$ and then settles to an approximately constant speed that is close to the peak velocity. The profile has been chosen to be the same as that generated by the motor accelerating the rods in the experiments. This explains why the curve is not smooth. We now turn to the physical modelling of the problem in the next section.

4.2 Physical model

The magnetic field from the Halbach array is completely diffused into the bar before it is accelerated. Hence the initial magnetic field distribution inside the bar is taken to be the same as it would be without the bar. The advective time scale is chosen to be the typical time that it takes to accelerate the bar from rest to its peak velocity, which is

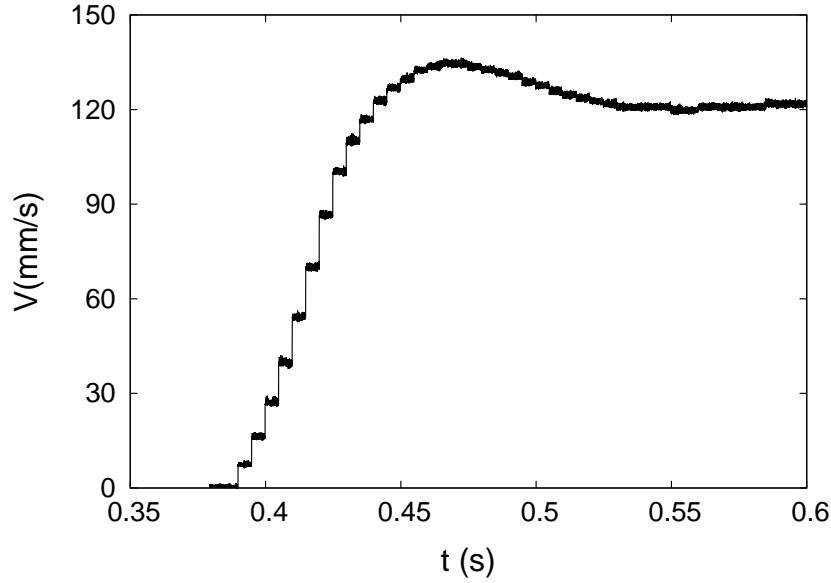


Figure 4.2: Typical velocity of the conducting bar as a function of time.

taken as $t_{adv} = 0.067$ s in our case. Since there is no inherent velocity scale, we choose L/t_{adv} , where L is the width of the bar. Using these scales along with B_0 and $B_0/\mu_0 L$ as the scales for the magnetic field and the current densities respectively, we obtain the non-dimensional form of the induction equation as

$$\frac{\partial \mathbf{b}}{\partial t} = -\nabla \times \left[\frac{\mathbf{j}}{R_m} - \mathbf{v} \times (\mathbf{b}_0 + \mathbf{b}) \right] \quad (4.1)$$

where $R_m = L^2/(\lambda t_{adv})$ and $\mathbf{j} = \nabla \times \mathbf{b}$. Here $\mathbf{v}(t) = v(t)\hat{i}$ is the time dependent uniform bar velocity known a priori from the experiment as for example in Fig. 4.2. The domain bounds are $(0 \leq x \leq l_x)$, $(-0.5 \leq y \leq 0.5)$ and $(-0.5 \leq z \leq 0.5)$. The induction equation is numerically solved using the coupled FD-BEM procedure outlined in the previous chapter. The size of the grid used was 256×64^2 with an equal grid stretch factor $S = 1.5$ in the y - and z -directions and a uniform grid in the x -direction.

4.2.1 Magnetic field of the Halbach array

In order to model the magnetic field distribution \mathbf{b}_0 arising from the Halbach array, it is assumed that each of the six magnets have unidirectional and constant magnetization. Furthermore, it is also assumed that the huge magnetic repulsive forces that are overcome to form the Halbach configuration do not affect the magnetization in the magnets. In such a case, the magnetic field from a single cuboidal magnet can be expressed in a closed analytical form. For example, the magnetic field at a point (x, y, z) outside a magnet of magnetization $M_s \hat{k}$ and with edge coordinates (x_1, x_2) , (y_1, y_2) and

4. Lorentz force transient response

(z_1, z_2) is given by

$$B_0(x, y, z) = \frac{\mu_0 M_s}{4\pi} \sum_{k=1}^{k=2} \sum_{m=1}^{m=2} \left[\begin{array}{c} (-1)^{k+m} \ln [F(x, y, z, x_m, y_1, y_2, z_k)] \\ (-1)^{k+m} \ln [H(x, y, z, x_1, x_2, y_m, z_k)] \\ \sum_{n=1}^{n=2} (-1)^{k+n+m} \tan^{-1} \left[\frac{(x-x_n)(y-y_m)}{(z-z_k)} g(x, y, z, x_n, y_m, z_k) \right] \end{array} \right] \quad (4.2)$$

where the functions F , H and g are given by

$$F(x, y, z, x_m, y_1, y_2, z_k) = \frac{(y - y_1) + \left[(x - x_m)^2 + (y - y_1)^2 (z - z_k)^2 \right]^{1/2}}{(y - y_2) + \left[(x - x_m)^2 + (y - y_2)^2 (z - z_k)^2 \right]^{1/2}}, \quad (4.3)$$

$$H(x, y, z, x_1, x_2, y_m, z_k) = \frac{(x - x_1) + \left[(x - x_1)^2 + (y - y_m)^2 (z - z_k)^2 \right]^{1/2}}{(x - x_2) + \left[(x - x_2)^2 + (y - y_m)^2 (z - z_k)^2 \right]^{1/2}}, \quad (4.4)$$

$$g(x, y, z, x_n, y_m, z_k) = \frac{1}{\left[(x - x_n)^2 + (y - y_m)^2 (z - z_k)^2 \right]^{1/2}}. \quad (4.5)$$

See Furlani [2001] for the derivation of the above the equations. The imposed magnetic field distribution b_0 in the simulation is the superposition of the fields of the six magnets, each of which is evaluated according to the dimensionless versions of equations (4.2) to (4.5), with a suitable transformation when the magnetization is not aligned in the z -direction. The magnetic field distribution inside the bar due to the Halbach array is shown in Fig. 4.3(b). It can be seen that the primary field component B_{0z} reverses its direction (as one moves along the length of the bar) through an X-point.

In order to verify that such an analytical description is close to the field produced in the experiment, we compared the magnetic field density measurements taken at specific locations in the vicinity of the magnet system. In the experiment, a Gauss sensor and a Hall sensor array (with 7 sensors) have been used to obtain the magnetic field data.

Figure 4.4(b) shows the variation of the primary component of the magnetic field B_{0z} at a point midway between the magnets (marked ‘G’ in Fig. 4.4(a)) with the distance of separation between the magnets. A very close agreement between the experiment and the analytical model is observed in this case. In fact, the value of the magnetization M_s was determined as that which leads to this close match of B_{0z} . This is necessary because of insufficient information about M_s of the magnets used in the experiment. Furthermore, Fig. 4.4(c) and Fig. 4.4(d) show respectively the vari-

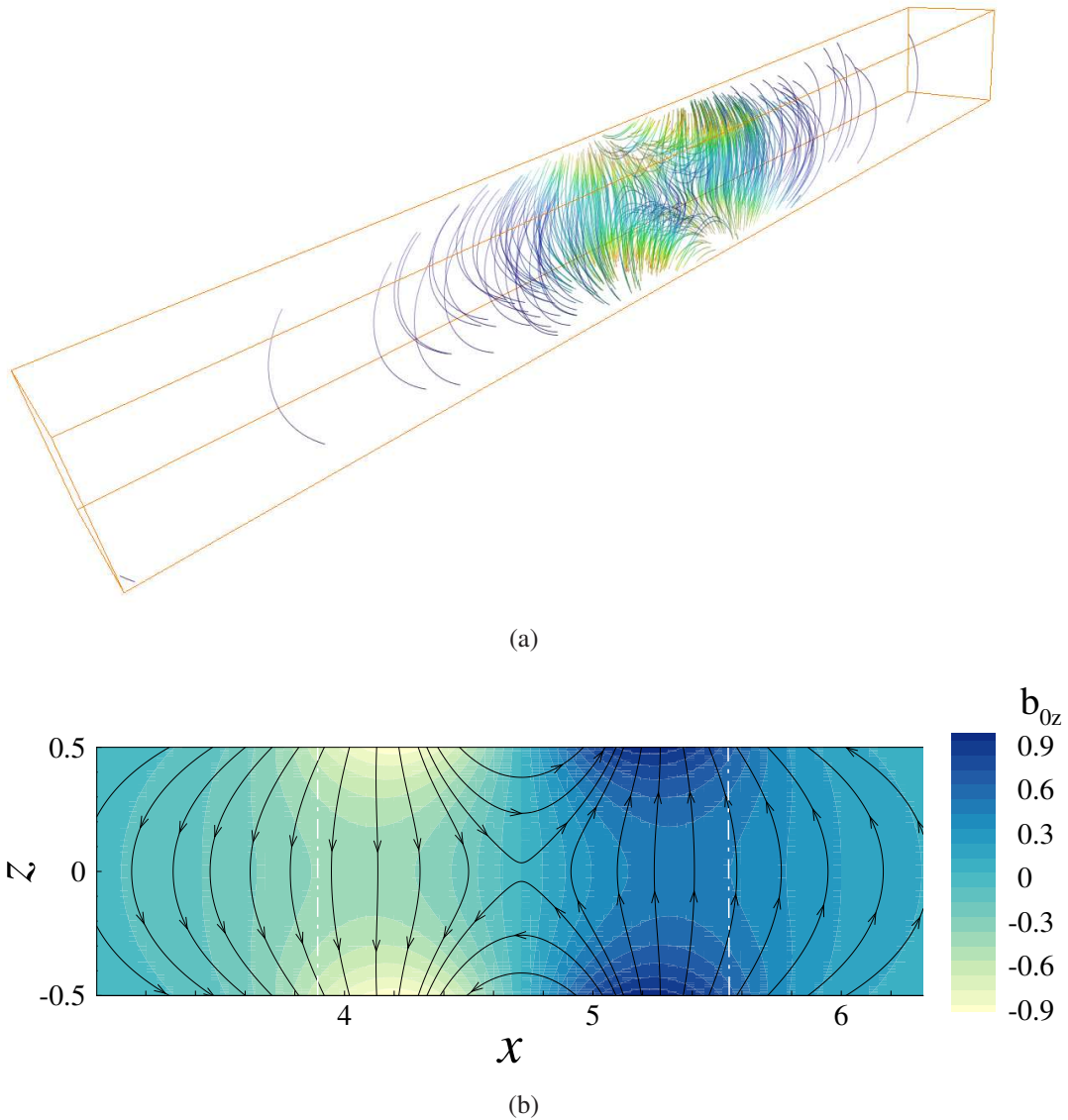


Figure 4.3: Streamlines of the initial magnetic field \mathbf{b}_0 in the bar. a) Three-dimensional, line coloring represents the field magnitude. b) In the xz -plane. The direction of motion is from left to right. Only a part of the bar length is shown. The white dotted lines indicate the extent of the magnets in that direction.

ation of B_{0z} along the lines $X' = -7$ mm (below the bottom level of the magnets) and $Z' = 45$ mm (along the symmetry line). The data were obtained in the experiment by sequentially traversing the Gauss sensor along these paths. In this case too, the agreement between the analytical model and the experiment is good with slight differences observed at certain locations. However, it can be seen from Fig. 4.4(e) that the values of the out-of-plane component B_{0y} along the centerline does not match well. For reasons of symmetry, the analytical model predicts vanishing y -component in those locations contrary to a clear trend seen from the measurements (although the magnitude itself is very low ~ 10 mT). In addition, Fig. 4.4(f) show the comparison of B_{0z} at the fixed lo-

4. Lorentz force transient response

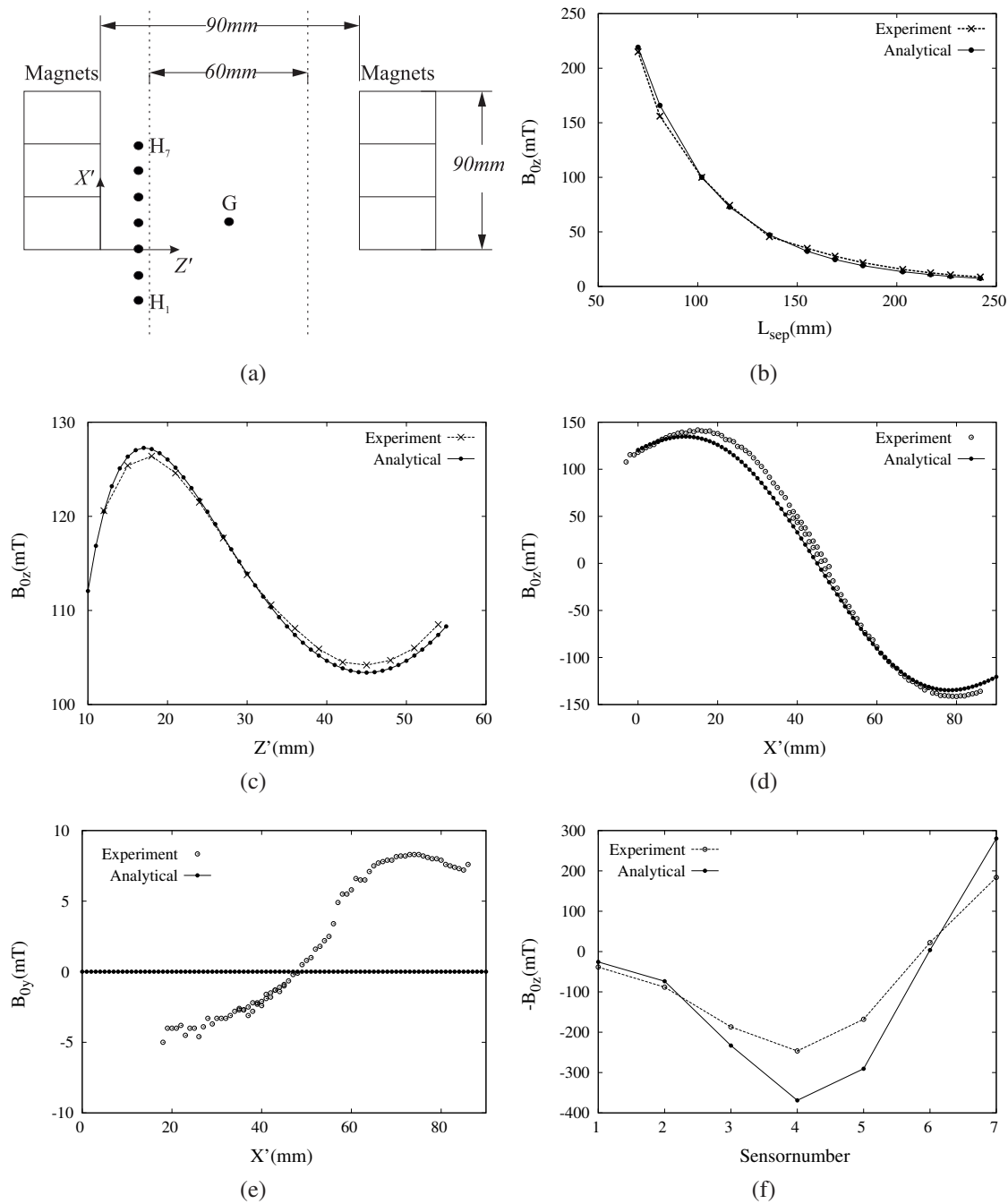


Figure 4.4: a) Schematic showing the coordinate system and the magnetic field sensor locations in the setup. H_1 to H_7 represent the Hall sensor array placed between the rod and the magnet system. Comparison of the imposed magnetic field component B_{0z} b) at the location of the Gauss sensor located midway between the magnets (marked by the black dot labelled 'G' in the schematic), as a function of the separation distance (L_{sep}) between the magnets, c) along the line $X' = -7\text{mm}$ and d) along the line $Z' = 45\text{mm}$. e) B_{0y} along the line $Z' = 45\text{mm}$ and f) B_{0z} at the locations of the Hall sensors. All the plots correspond to the mid-plane $y = 0$.

cations of the seven Hall sensors. It is observed that the analytical model overpredicts significantly at the locations of the sensors H_4 and H_5 , although the agreement is fairly good at the other locations. These differences can be attributed to the shortcomings of

the assumptions of uniform (and unidirectional) magnetization and neglecting the alteration that might occur in the magnetization when the strong magnets are brought together. It must be noted that the differences observed at the sensors H4 and H5 (that are exterior to the bar) are 54% and 73% respectively, indicating that there is a possibility that the differences of the imposed magnetic field might be of the same order of magnitude at other locations inside the material of the bar. In summary, the analytical model describes the Halbach magnetic field very well for the most part, but also shows significant differences at some locations that were examined. With this in mind, we now turn to the results obtained from the simulations.

4.3 Results and comparison with experiments

In order to facilitate comparison with experiments, simulations were done for square cross-section bars of the same cross-sectional area as that of the rods used in the experiments. This would imply that the R_m in the simulations will be slightly lower than that in the experiments of the corresponding configuration. Although several different bar sizes were considered, the primary focus here will be on the configuration with a copper bar of $53.2 \text{ mm} \times 53.26 \text{ mm}$ cross-section (that corresponds to the rod of diameter 60 mm used in the experiments) and a bar-to-magnet surface distance of 15 mm. This will be the case for most part of this section, unless otherwise explicitly stated. Simulations are carried out during the same time window as shown in Fig. 4.2, i.e. from the state of rest until an approximately steady state is reached, with a velocity peak in between.

At first, a qualitative picture of the steady state can be obtained from the streamlines of \mathbf{b} at $R_m = 10$ in the mid-plane (xz -plane) shown in Fig. 4.5. One can see that the field lines are advected (the X-point as well) in the direction of motion of the bar. This is seen to occur through a series of severing and reconnections occurring in the vicinity of the X-point. Specific patterns in which reconnection occurs near the X-point in the case of a 2D flow will be discussed in Chapter 5.

The current density streamlines display a three roll structure as can be seen from Fig. 4.6, which corresponds to $R_m = 3.2$. The current density on the surface has the largest magnitude as displayed by the streamline coloring. In particular, the maximum values of $|j|$ was observed on the four edges of the bar. The corresponding surface streamlines are shown in Fig. 4.7(a), of particular mention being the existence of critical points of current density on the y -faces (green coloured streamlines).

We now move on to the quantitative results concerning the integral streamwise Lorentz force over the domain, which is the quantity of primary interest in this study.

4. Lorentz force transient response

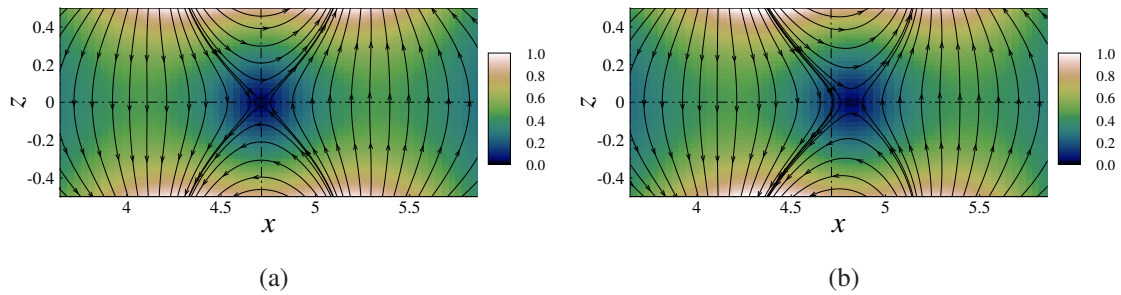


Figure 4.5: a) Field lines of the magnetic field in the xz -midplane near the X-point at a) the initial state $t = 0$ and b) the final steady state when the rod reached a constant velocity, at $R_m = 10$. Contour coloring is by the two-dimensional magnitude $\sqrt{b_{xt}^2 + b_{zt}^2}$ of the total magnetic field.

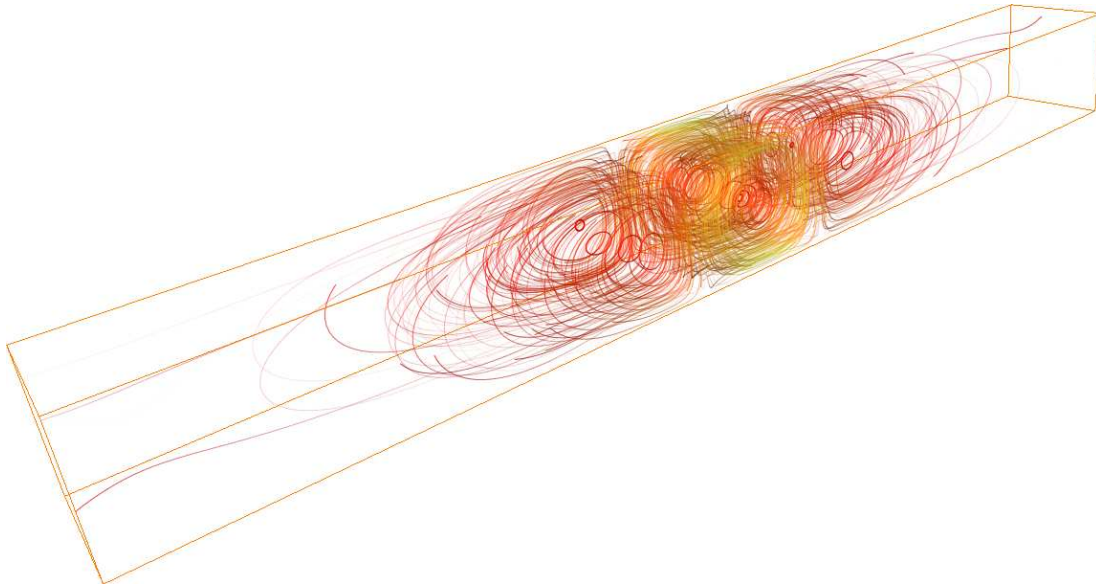


Figure 4.6: Streamlines of the current density in the steady state, at $R_m = 3.2$. Contour coloring is by the magnitude of current density.

This is computed at regular time intervals using

$$F_l = \frac{B_0^2 L^2}{\mu_0} \int [\mathbf{j} \times (\mathbf{b} + \mathbf{b}_0)] dx dy dz. \quad (4.6)$$

In the case of a bar acceleration involving a peak velocity $V_{max} = 136.5 \text{ mm s}^{-1}$, the time response of Lorentz force is shown in Fig. 4.8(a). The velocity of the rod is also plotted here (with a dotted line) for reference. One can observe that the Lorentz force follows a similar profile as the bar velocity, but with a time lag/shift that can be seen from the respective peak values. Qualitatively, this is similar to the curve obtained in the experiment using piezoelectric force sensors. However, the value of the peak Lorentz force is overpredicted in the simulation by a factor of ≈ 3.4 . This can be clearly attributed to two reasons, both related to the geometry of the problem. The

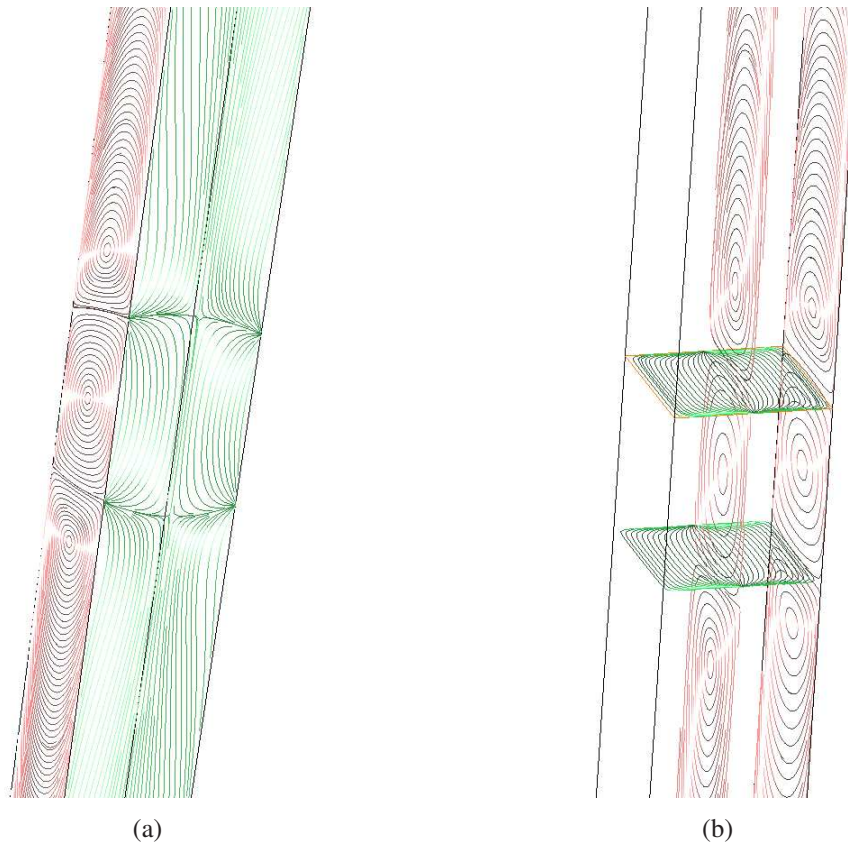


Figure 4.7: Projected streamlines on the a) Boundary faces and b) at specific planes, of the current density j in the steady state at $R_m = 3.2$. Streamlines colored red are on xy -planes.

primary geometric difference is in the magnetic field distribution of the Halbach array, where there were indications (although in the bar exterior) that the model overpredicts the field by a factor of about 73%, which roughly translates to a factor of $1.73^2 \approx 3.0$ in the Lorentz force (since $L_f \sim B_0^2$). The second difference is in the shape of the cross-section. For these reasons, only qualitative comparisons between the experiment and simulations will be discussed. It must also be noted here that the experimental curve shows a slow decay of Lorentz force even in the steady state (which has been attributed to charge leakage effects in the piezoelectric sensors), whereas the simulations predict a flat profile physically consistent with the velocity profile.

Study of the sensitivity of the result to the grid resolution, grid stretching and the bar length considered, indicate that the problem is well resolved beyond doubt. Details of the sensitivity study is given in Appendix C.

Furthermore, simulations were also performed with a wide range of peak velocities occurring within the same time interval. As expected, the peak Lorentz force shows a linear dependence on the peak bar velocity (see Fig. 4.8(b)) and with a different slope as compared to the measured values. Of key interest is the dependence of the peak Lorentz force on R_m . This is done with a fixed configuration and only changing the

4. Lorentz force transient response

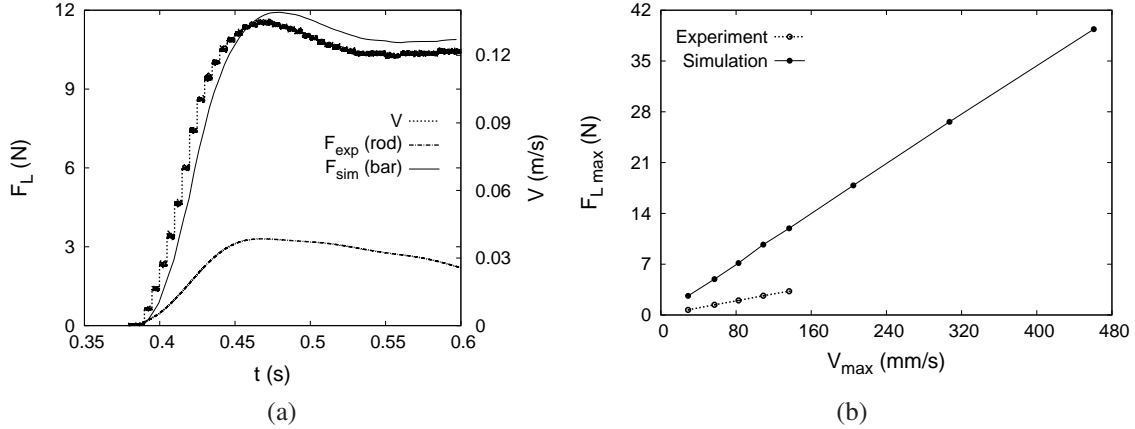


Figure 4.8: a) Lorentz force as a function of time for the copper rod (experiment) and bar (simulation) of the same cross-section. Rod diameter $D = 60$ mm and the bar cross-section is 53.2 mm \times 53.26 mm. Maximum velocity during the acceleration, $V_{max} = 136.5$ mm s $^{-1}$ b) Maximum Lorentz force as a function of V_{max} .

electrical conductivity σ of the bar to values both much lower and higher than that of Copper. A range of magnetic Reynolds numbers $0.5 \leq R_m \leq 50000$ was considered. The dependence is shown in Fig. 4.9. Here, the Lorentz force plotted is normalized by $\sigma V_{max} B_0^2 L^2 l_{mag}$, which is the ideal force that would act on a bar length equal to the length of the magnet array, when a uniform field of magnitude B_0 is imposed.

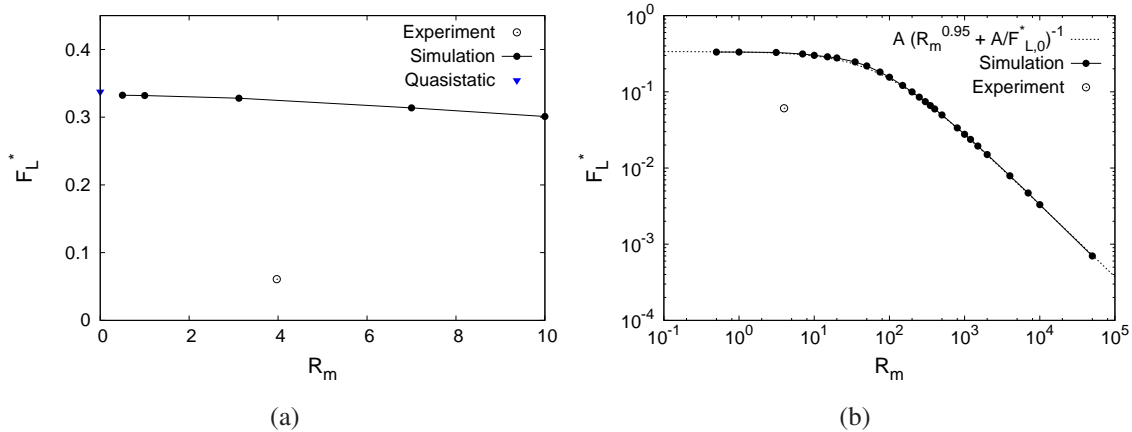


Figure 4.9: Normalized Lorentz force F_L^* as a function of R_m , a) shown only for $R_m \leq 10$ and b) over the entire range of R_m considered. Constant $A = 21$ and $F_{L,0}^* = 0.3376$.

The low range of R_m is relevant to LFV, in which as one can observe from Fig. 4.9(a), the Lorentz force decays very slowly with increasing R_m until about $R_m \approx 10$. In quantitative terms, at $R_m = 10$, the peak Lorentz force is reduced by approximately 12% than it is at $R_m = 0$. Such information is extremely useful in the design and calibration of LFV in transient flow applications. It is also interesting to note that the limiting Lorentz force value obtained for low R_m nicely agrees with the Lorentz force obtained by a simulation performed using the quasistatic formulation (using the electric poten-

tial). This is represented by the blue triangle in Fig. 4.9(a). Further increase in R_m leads to a drastic drop in the Lorentz force in the range approximately $10 \leq R_m \leq 500$ as shown in Fig. 4.9(b). Beyond this, the Lorentz force continues to decay at a rate $\sim R_m^{-1}$ for sufficiently high values of R_m . The behavior in the whole range fits well to the function $F_L^* = A \left(R_m^{0.95} + A/F_{L,0}^* \right)^{-1}$, where $F_{L,0}^*$ is the peak Lorentz force at $R_m = 0$.

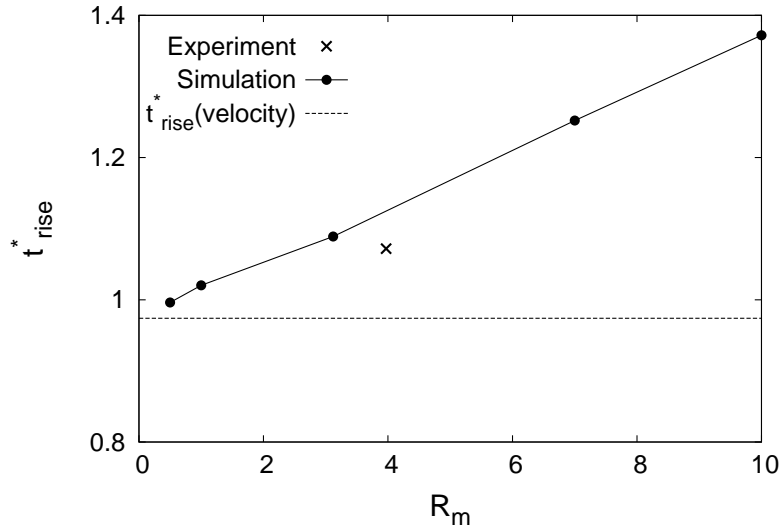


Figure 4.10: Time taken to reach from 2% to 98% of the peak Lorentz force, t_{rise}^* (normalized by the advective time scale), as a function of the magnetic Reynolds number R_m .

Table 4.1: Comparison of t_{rise}^* between experiment and simulation.

Material	D (mm)	R_m	t_{rise}^*		
			Experiment	Simulation	Difference (%)
Copper	40	1.78	0.961	1.016	5.6
Copper	50	2.72	1.006	1.067	6.1
Copper	60	3.97	1.072	1.116	4.1
Aluminium	50	0.94	1.034	1.020	-1.4
Aluminium	60	1.29	1.032	0.986	-4.5
Aluminium	80	2.42	0.968	1.063	9.9

Beside the Lorentz force magnitude, the time lag (as compared to $R_m = 0$) that is expected to occur at finite R_m is important in transient LFV applications. Information regarding this is obtained through the non-dimensional time t_{rise}^* , which is the time in advective units that it takes for the Lorentz force to increase from a value of 2% to 98% of the peak Lorentz force. As can be seen from Fig. 4.10, the time lag increases linearly with R_m . Consistently, at low values of R_m , t_{rise}^* tends to the baseline, which is the time

4. Lorentz force transient response

taken by the velocity itself to rise from 2% to 98% of its peak value. At $R_m = 10$, the time lag is already very significant, being approximately 40% of the time it takes for the corresponding velocity rise. The slight deviation of the curve from linearity is attributed to the not so smooth nature of the acceleration profile, due to which a small ambiguity occurs in determining the exact time instants at which the 2% and 98% Lorentz force values occur. Further, the time lag is seen to be reasonably close to the only measured value in the experiment that corresponds to this configuration.

In the experiments, several measurements of t_{rise}^* were made with slightly different configuration and two different rod materials, namely Copper and Aluminium. These cases were simulated as well and a comparison of the rise time is shown in Table. 4.1. A maximum difference of $\approx 10\%$ was observed between the simulation and experimental values. This supports a reasonable agreement between the experiment and simulations.

Chapter 5

Magnetic flux expulsion and bifurcations in a plane channel flow

This chapter presents the study of magnetic flux expulsion and the associated bifurcation in an MHD plane channel flow configuration, using direct numerical simulations (DNS).

5.1 Introduction

As mentioned in Chapter 3, an interesting feature of MHD flows at high magnetic Reynolds numbers is the expulsion of magnetic flux that typically occurs under the imposition of an electrically conducting fluid flow with closed streamlines. This follows from an analogy with the well known Prandtl-Batchelor theorem (Batchelor [1967]) in classical hydrodynamics. The kinematic problem of magnetic flux expulsion under rotation has been extensively studied during the sixties (see e.g. Parker [1963, 1966]; Weiss [1966]) in the context of astrophysics. That flux expulsion also persists in the dynamic regime was pointed out by Galloway *et al.* [1978] and was followed by further analysis of the dynamic effects of flux ropes in Rayleigh-Bénard magnetoconvection (Proctor & Galloway [1979]).

An important aspect of the dynamic behavior associated with flux expulsion is the ‘runaway’ effect, which can be explained as follows. When magnetic field lines start to get expelled in a region of the flow, there is a decrease in the Lorentz forces that opposes the mean flow leading to an acceleration of the flow in that region. This in turn leads to further expulsion of magnetic flux and subsequently results in a cascading effect of flow acceleration and flux expulsion, wherein dissipative forces like viscosity ultimately balances the driving force, leading to a steady state. This effect can play a significant role in the performance of electromagnetic pumps that are used to pump

liquid metal. Early analytical studies of this phenomenon by Gimblett & Peckover [1979] using rotating cylindrical and spherical solid bodies under an applied normal magnetic field showed an associated Thom cusp catastrophe and hysteresis effect. Such behavior was seen further in the fluid context by Moffatt (Moffatt [1980]).

However, flux expulsion can also happen in flow configurations without closed streamlines, if the imposed magnetic field is non-uniform and periodic in the mean flow direction. A particularly interesting configuration is that of a plane channel flow driven by a mean pressure gradient with an imposed sinusoidal magnetic field that was analysed by Kamkar & Moffatt [1982] which will be denoted as KM82 hereafter. In their study, the interaction of the flow and magnetic fields was described by simplified one-dimensional model equations. Steady state solutions were obtained from which two different flow regimes were identified, namely the Hartmann and Poiseuille regimes and the location of the bifurcation leading to the transition between these two regimes was computed. However, various simplifications were assumed in that study. For example, the non-linear terms (and hence the Reynolds stress terms) in the Navier-Stokes equation and the variations along the streamwise direction were neglected. Although it enables one to obtain quick solutions, the approximate model can lead to significant loss of accuracy and underprediction/overprediction of the jump that occurs during the bifurcation. The focus of this chapter is on 2D direct numerical simulations of the problem similar to KM82 with a twofold purpose. On one hand, it helps one to validate the 1D model predictions at the steady state and quantify the differences arising out of the simplifications of the model. On the other hand, the presence of non-linearities can result in time-dependent solutions for the flow and magnetic fields in both the regimes in the final state.

This chapter is organized as follows: section 5.2 describes the problem setup and the full governing equations along with a brief overview of the KM82 model. This is followed by the details of the numerical procedure in section 5.2.2. In section 5.3, numerical results of the DNS are presented and compared to the predictions of the model, including the effect of various parameters on the characteristics of the bifurcation.

5.2 Problem setup and governing equations

5.2.1 Problem formulation and full governing equations

We consider the two-dimensional incompressible flow of an electrically conducting fluid (e.g. a liquid metal) driven by a mean pressure gradient in a straight rectangular channel. Periodicity is assumed along the streamwise direction x and the wall normal

direction is denoted by z . A magnetic field $\mathbf{B}_0(x, z) = \mathbf{B}(x, z, t = 0)$ (generated by electric current or magnet sources outside the channel) with a prescribed wall normal component $B_{0z} = \cos(kx)$ with a wavenumber k , is imposed on the flow¹. Such a periodic magnetic field can be ideally produced e.g. by magnets distributed on the channel walls with alternating north and south poles in the streamwise direction (see Kamkar & Moffatt [1982]). The action of the flow on the magnetic field generates plane-normal electric current densities $\mathbf{J} = (0, J(x, z), 0)$ in the flow which leads to the generation of a secondary magnetic field and Lorentz forces that affect the flow. The imposed magnetic field which is divergence-free can be expressed as $\mathbf{B}_0 = \nabla \times \mathbf{A}_0$, where $\mathbf{A}_0 = (0, A_0(x, z), 0)$ is the magnetic vector potential. Choosing the scales of half channel height L for the length, the maximum value of the imposed magnetic field B_0 for the magnetic field, B_0L for the vector potential and applying the curl-free condition on \mathbf{B}_0 , we get in the non-dimensional form,

$$\frac{\partial^2 a_0}{\partial x^2} + \frac{\partial^2 a_0}{\partial z^2} = 0, \quad (5.1)$$

with the boundary conditions

$$\frac{\partial a_0}{\partial x} = \cos(\kappa x) \text{ on } z = \pm 1 ; a_0(0, z) = a_0(l_x, z) \quad (5.2)$$

where the symbol $\kappa = kL$ represents the normalized wavenumber, l_x is the non-dimensional streamwise length of the channel and a_0 is the normalized vector potential. Solution of equation (5.1) using separation of variables yields

$$a_0 = \frac{1}{\kappa} \frac{\sin(\kappa x) \cosh(\kappa z)}{\cosh(\kappa)}. \quad (5.3)$$

This leads to the form of the non-dimensional initial (or imposed) magnetic field \mathbf{b}_0 as

$$\mathbf{b}_0 = -\frac{\sin(\kappa x) \sinh(\kappa z)}{\cosh(\kappa)} \mathbf{i} + \frac{\cos(\kappa x) \cosh(\kappa z)}{\cosh(\kappa)} \mathbf{k}, \quad (5.4)$$

the field lines of which are shown in Fig. 5.1. Here \mathbf{i} and \mathbf{k} refer to the unit vectors in the streamwise (x) and wall-normal (z) directions respectively.

The physics of the problem is governed by the Navier-Stokes equation for the momentum balance including the additional source term representing the Lorentz force (body force) produced by the induced electric currents and the induction equation for magnetic field transport along with the constraints of mass conservation (conti-

¹Throughout this chapter, the subscript 0 indicates conditions at time $t = 0$ rather than an ‘‘imposed field’’ and the total magnetic field is denoted by \mathbf{B} or \mathbf{b} without a subscript t .

5. Flux Expulsion

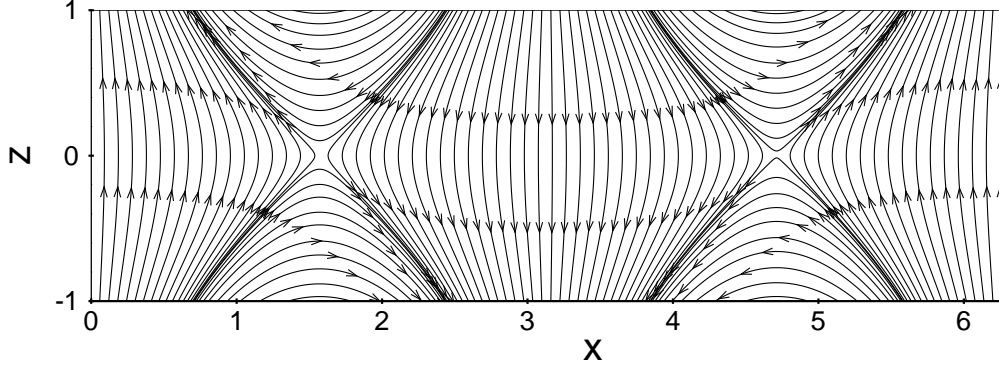


Figure 5.1: Field lines of the imposed magnetic field \mathbf{b}_0 as given by equation (5.4). Two magnetic X-points at $(x = \pi/2, z = 0)$ and $(x = 3\pi/2, z = 0)$ can be observed at the centerline.

nuity) and solenoidality of the magnetic field. The pressure gradient is decomposed as $\nabla P_T = -\rho G \mathbf{i} + \nabla P$, where ∇P_T represents the cumulative pressure gradient and $-\rho G$ the constant mean pressure gradient that is applied in the streamwise direction. Non-dimensionalizing using the scales $\lambda/L^2 k$, $\lambda/L^2 k G$, $\rho G L$ and $\sigma \lambda B_0/L^2 k$ for velocity, time, pressure and the current densities respectively, and denoting all non-dimensional variables by small letters, the system of governing equations can be written as

$$\frac{\partial \mathbf{v}}{\partial t} + \frac{1}{\beta \kappa} (\mathbf{v} \cdot \nabla) \mathbf{v} = 1 - \nabla p + \varepsilon \nabla^2 \mathbf{v} + \frac{1}{Q} (\mathbf{j} \times \mathbf{b}), \quad (5.5)$$

$$\frac{\partial \mathbf{b}}{\partial t} + \frac{1}{\beta \kappa} (\mathbf{v} \cdot \nabla) \mathbf{b} = \frac{1}{\beta \kappa} (\mathbf{b} \cdot \nabla) \mathbf{v} + \frac{1}{\beta} \nabla^2 \mathbf{b}, \quad (5.6)$$

$$\nabla \cdot \mathbf{v} = 0, \quad (5.7)$$

$$\nabla \cdot \mathbf{b} = 0, \quad (5.8)$$

$$\mathbf{j} = \kappa (\nabla \times \mathbf{b}), \quad (5.9)$$

$$u = w = 0, \quad b_z = \cos(\kappa x) \text{ on } z = \pm 1, \quad (5.10)$$

$$\mathbf{v}(0, z) = \mathbf{v}(l_x, z), \quad \mathbf{b}(0, z) = \mathbf{b}(l_x, z) \quad (5.11)$$

with the no-slip and no penetration boundary conditions for the fluid velocity on the walls and periodicity assumed in the streamwise direction. Furthermore, the wall normal component of the magnetic field b_z on the walls remain unchanged (equal to the imposed magnetic field, b_{0z}) and the streamwise component follows from the divergence-free condition (5.8). The parameters involved in the problem are

$$\varepsilon = \frac{\nu \lambda}{L^4 k G}, \quad \beta = \frac{L^4 k G}{\lambda^2}, \quad Q = \frac{\rho L^2 k G}{\sigma \lambda B_0^2}, \quad \kappa = kL \quad (5.12)$$

where ν and ρ represent the kinematic viscosity and the mass density of the fluid respectively. The parameter β represents the magnetic Reynolds number and the parameters ε , Q can be regarded as the inverse of the hydrodynamic Reynolds number and the Stuart numbers respectively. All the fluid properties are assumed to be constant. The coupled evolution of the velocity and magnetic fields is computed by solving the governing equations numerically, a brief summary of which is presented next.

5.2.2 Numerical Procedure

The numerical solution of the system (5.5) to (5.11) is obtained using second order finite differences, on similar lines as the procedure described in chapter 3 but with specific differences. Therefore a brief outline of the key differences and features will be discussed here. The domain is discretized into a rectangular Cartesian grid with uniform grid spacing along the streamwise direction and a non-uniform stretched grid in the wall normal direction in order to resolve the thin Hartmann boundary layers near the walls. A typical grid used in our studies is shown in Fig. 5.2. Here, since we con-

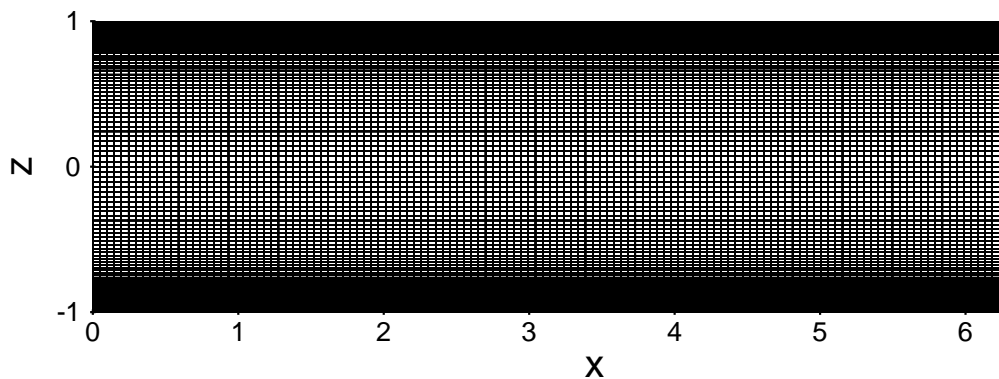


Figure 5.2: Non-uniform structured grid in the xz -plane with 129×129 grid points and $S = 2.2$.

sider a constant imposed streamwise pressure gradient, the volume flux through the channel is not set to a constant value. The explicit scheme is used for the integration of the momentum equation. Other details of the numerical procedure to compute the velocity field remains the same and can be found in chapter 3. However, for the magnetic field, one can see that the conditions on the boundary are specified and hence the boundary integral procedure described in chapter 3 will not be used. The normal component of the magnetic field b_z is computed by using a semi-implicit procedure. The resulting Poisson equation for b_z is computed using FISHPACK (Adams *et al.* [1999]). Subsequently, the streamwise component b_x is reconstructed from b_z using equation (5.8), in order to satisfy the solenoidality of the magnetic field. Alternatively, it is possible to solve for the vector potential A (since the problem is 2D, A has only one

component) and recover the magnetic field components b_x and b_z from A . OpenMP parallelization has been used in performing the computations for the results presented in this chapter.

5.2.3 One-dimensional approximate model of Kamkar and Moffatt (KM82)

In view of the fact that the results of our DNS are compared with the 1D approximate model of KM82, we present a brief overview of their model here. The following assumptions have been made in the model:

- The secondary magnetic field consists of only a single mode (wavenumber) along the streamwise direction, which is taken to be the wavenumber (k) of the applied magnetic field. To this effect, the vector potential A of the magnetic field \mathbf{b} is expanded as

$$A(x, z, t) = B_0 k^{-1} \Re \left[i f(z, t) e^{ikx} \right] \quad (5.13)$$

where \Re represents the real part and $f(z, t)$ is the dimensionless profile function.

- The variation of dynamics in the streamwise direction is neglected and hence the mean (x -averaged) governing equations are considered.
- The velocity fluctuations \mathbf{v}' are small compared to the mean (x -averaged) streamwise velocity U , $|\mathbf{v}'| \ll U$ and hence the Reynolds stress terms in the momentum equation and the fluctuating parts of advection terms in the A -transport are neglected. This assumption is supposed to be valid when $\beta \ll Q^2$.

The assumptions stated above lead to the following mean governing equations for $U(z, t)$ and $f(z, t)$ in the non-dimensional form,

$$\frac{\partial U}{\partial t} = 1 - \frac{1}{2Q} \Re \left[i f \left(\frac{\partial^2}{\partial z^2} - \kappa^2 \right) f^* \right] + \varepsilon \frac{\partial^2 U}{\partial z^2}, \quad (5.14)$$

$$\beta \frac{\partial f}{\partial t} + iUf = \left(\frac{\partial^2}{\partial z^2} - \kappa^2 \right) f \quad (5.15)$$

$$U = 0, \quad f = 1 \quad \text{on } z = \pm 1; \quad (5.16)$$

which correspond to equations (2.33) and (2.38) in KM82, where f^* is the complex conjugate of f . For later comparisons with the DNS results, we solve the above model equations (5.14) to (5.16) by a finite-difference method on a uniform grid.

5.3 Results and comparison

Starting with either an initial laminar velocity profile (with no streamwise variation) or fluid at rest ($v = 0$) and the imposed magnetic field \mathbf{b}_0 , the governing equations are numerically integrated in time to obtain the final equilibrium states. All the computations have been performed for a streamwise domain length of one period, $l_x = 2\pi/\kappa$ on a 129×129 grid. A grid sensitivity study was performed which indicated that further increase in grid resolution does not improve the solution accuracy significantly, within the parameter space studied here. Depending on the velocity profiles of the final states, two regimes of flows are defined (as in KM82), namely the Hartmann regime and the Poiseuille regime.

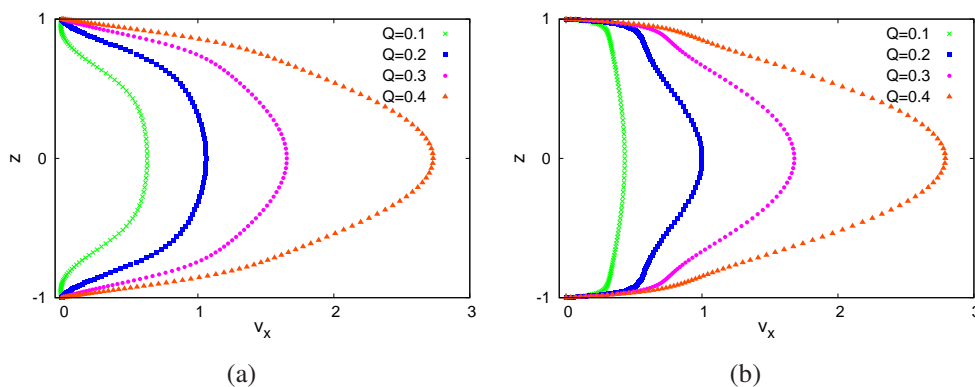


Figure 5.3: Steady state streamwise velocity profiles in the Hartmann regime at (a) $x = \pi/2$ and (b) $x = \pi$. Parameters are $\beta = 1$, $\kappa = 1$ and $\varepsilon = 5 \times 10^{-3}$.

The Hartmann regime is characterized by very steep velocity gradients in the boundary layers as compared to the core region. Pressure gradient in the core is dominantly balanced by Lorentz forces whereas in the boundary layers it is a combination of viscous and Lorentz forces that balances the pressure gradient. Flows at relatively small Q or high interaction parameter belong to this regime. In contrast, the Poiseuille regime typically demonstrates ‘Poiseuille-like’ (parabolic) axial velocity profiles and is dominated by viscosity in the core region. Flows at relatively higher Q belong to the Poiseuille regime. The final equilibrium state of the Hartmann regime is observed to be steady in time unlike the Poiseuille regime where significant velocity fluctuations persist in final state. Transition between the two regimes occurs over a narrow band of Q through a bifurcation that is a manifestation of the runaway effect. We now provide a very brief account of the nature of the solutions in these two regimes.

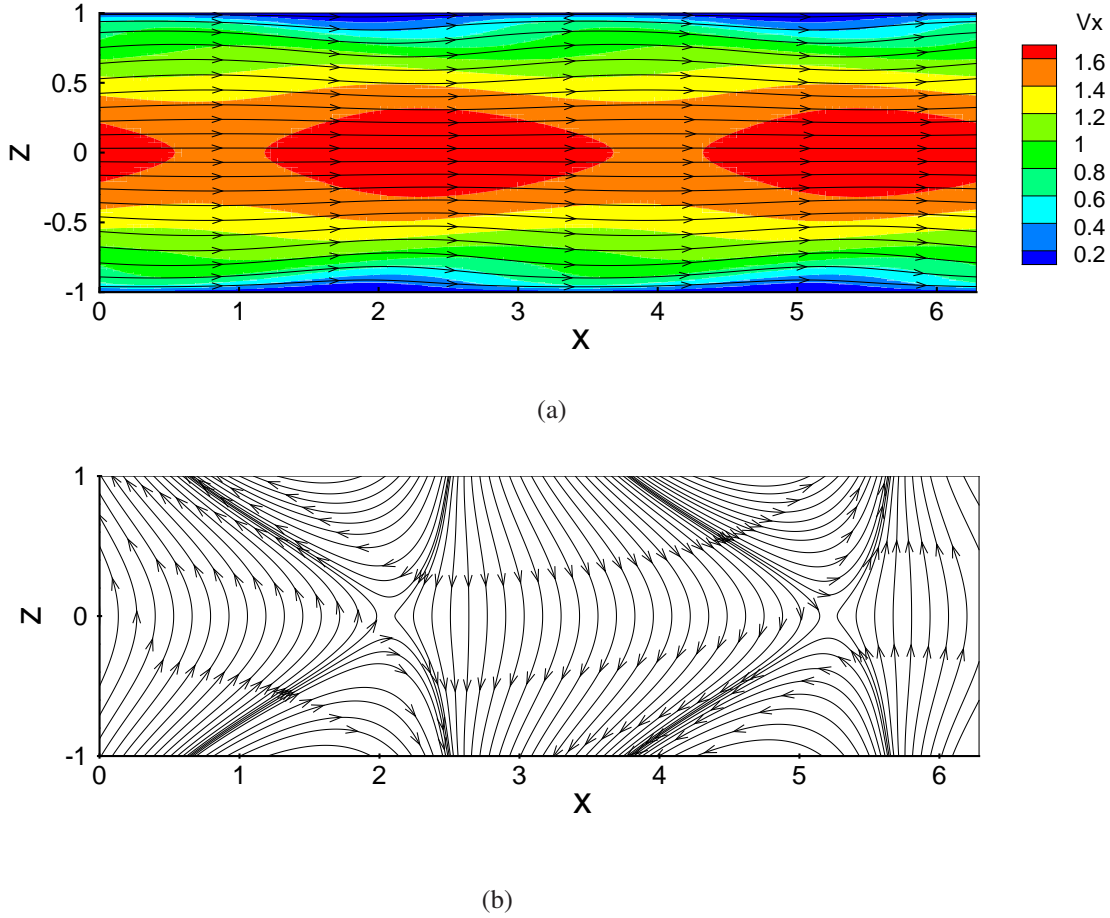


Figure 5.4: Typical streamwise velocity and magnetic field configuration in the Hartmann regime. (a) Contours of streamwise velocity and (b) magnetic field lines in the steady state at $Q = 0.3$, for $\beta = 1$, $\kappa = 1$ and $\varepsilon = 5 \times 10^{-3}$. We observe how the magnetic X-points are slightly shifted by the flow.

5.3.1 Hartmann regime

Typical axial velocity profiles in the Hartmann regime are shown in Fig. 5.3 at two different axial locations of the channel, $x = \frac{\pi}{2}$ and $x = \pi$ and at various values of the parameter Q . These two locations correspond to the streamwise extreme values of the imposed magnetic field b_0 . It can be observed from Fig. 5.3 that higher axial velocities (or flow acceleration from the initial state) are observed with increase in Q and the profiles in the boundary layers at $x = \pi$ look more ‘Hartmann-like’ than at $x = \frac{\pi}{2}$ due to the pronounced effect of the wall normal component b_{0z} . The distribution of axial velocity v_x in the domain as shown in Fig. 5.4(a) (along with the velocity streamlines) clearly indicates the laminar nature of the flow in the Hartmann regime. Advection of the magnetic field can be observed from the corresponding field lines shown in Fig. 5.4(b) that indicate only a slight bending of the field lines. As is clear from the velocity field, no significant events of severing or reconnection of field lines

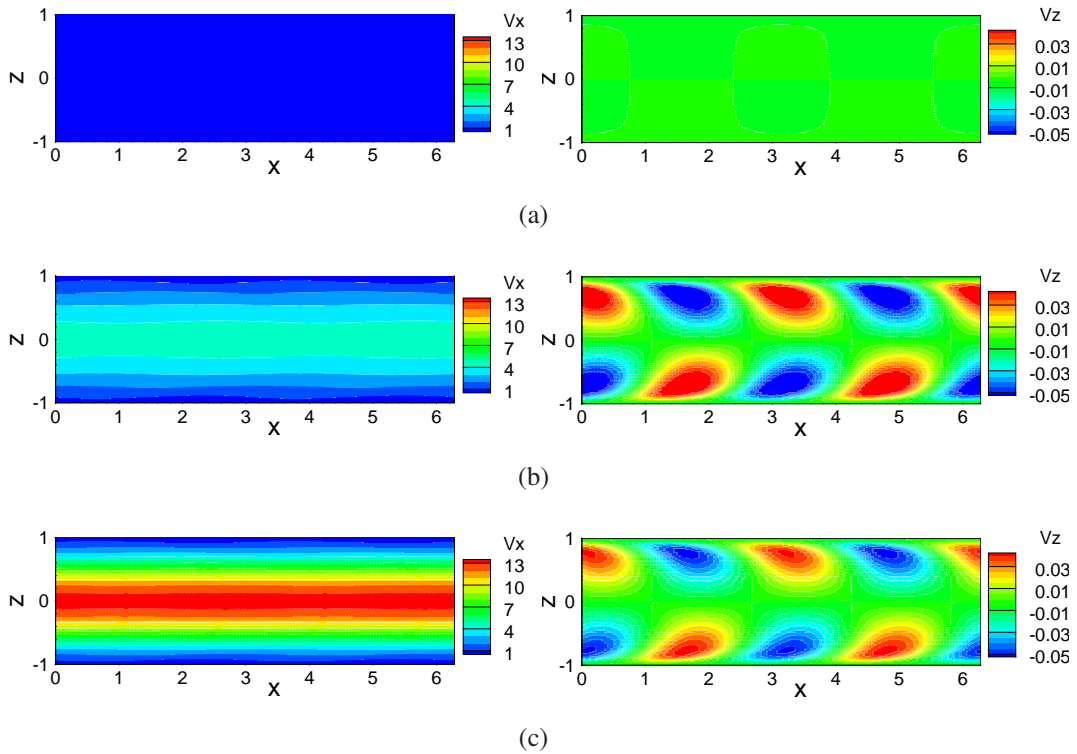


Figure 5.5: Contours for the evolution of velocity field to the Poiseuille-like state as the flow accelerates from rest. (a) $t = 0$, (b) $t = 16.1$, (c) $t = 60.1$. Parameters are $Q = 0.5$, $\beta = 1$, $\kappa = 1$ and $\varepsilon = 5 \times 10^{-3}$. Left column: streamwise velocity v_x . Right column: wall-normal velocity v_z .

are observed in this regime.

5.3.2 Poiseuille regime

The Poiseuille regime is a result of the runaway effect, where there is a significant acceleration of the flow due to considerable bending and severing of field lines and subsequent expulsion of magnetic flux. The streamwise velocity profiles show significant gradients in the wall normal direction and hence look ‘Poiseuille-like’. It is observed that the flow exhibits strongly unsteady behavior even in the final (steady on average) state. Of particular interest is the initial phase of the transient flow that ensues when the flow starts to accelerate from rest, due to the applied mean pressure gradient. The evolution of the velocity field leading to almost complete expulsion of magnetic flux in the core ($z = 0$) in such a case is shown in Fig. 5.5 through snapshots of velocity component contours. It can be seen that the gradual acceleration of the streamwise velocity is accompanied by relatively small wall normal velocity component on both side sides of the core, in a staggered arrangement. At the same time, the normal component of the magnetic field (which leads to streamwise Lorentz force) in the core is gradually destroyed, due to the bending of the vertical field lines (due to advection) as

5. Flux Expulsion

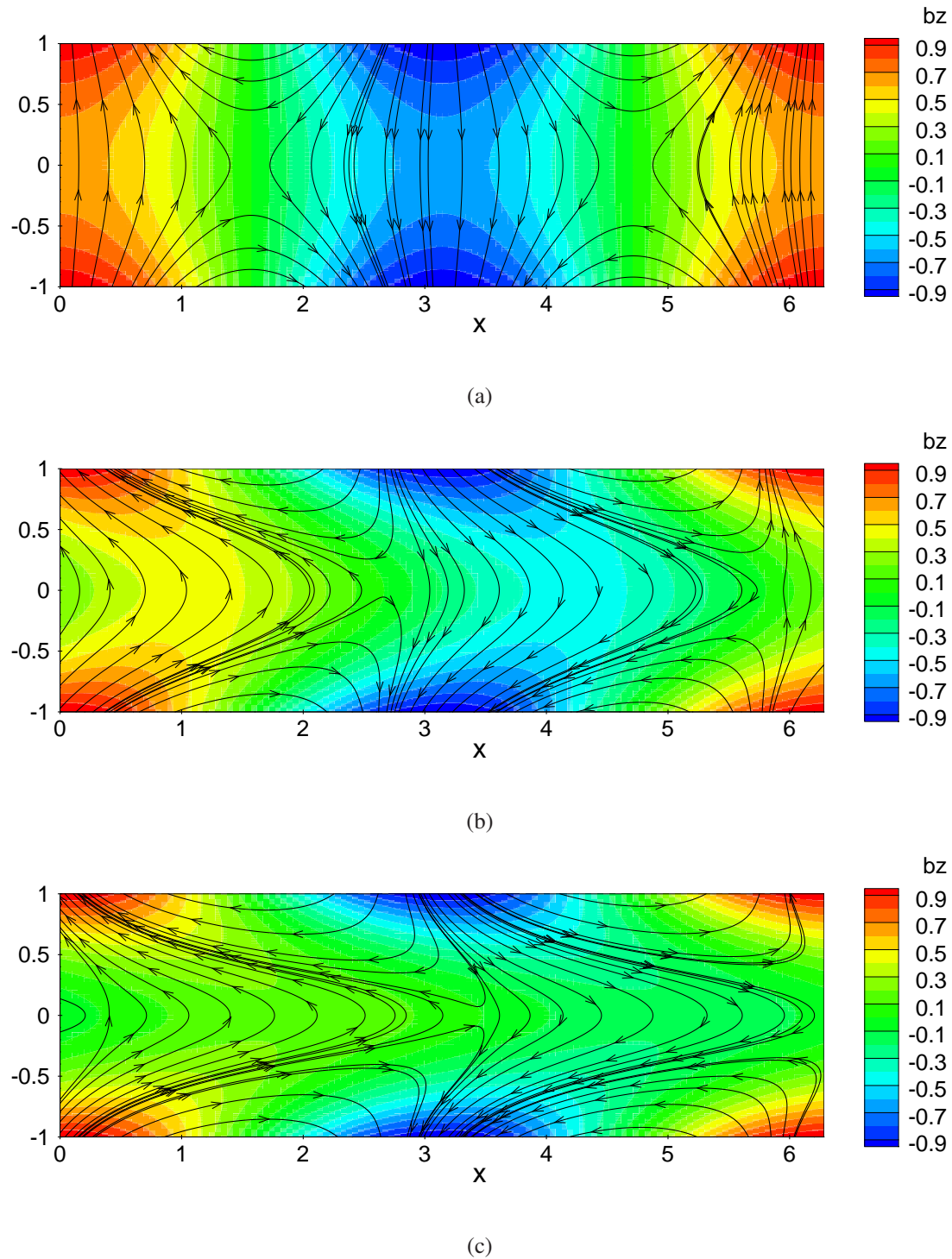


Figure 5.6: Advection and expulsion of magnetic flux as the flow starts to accelerate from rest. (a) $t = 0$, (b) $t = 16.1$, (c) $t = 60.1$. Parameters are $Q = 0.5$, $\beta = 1$, $\kappa = 1$ and $\varepsilon = 5 \times 10^{-3}$. Contours coloured by b_z .

well as the reconnection of the field lines, depending on the streamwise location in the channel. Reconnection here refers to the rearrangement of magnetic field line topology. When two field lines come into contact and locally compress, gradients in the

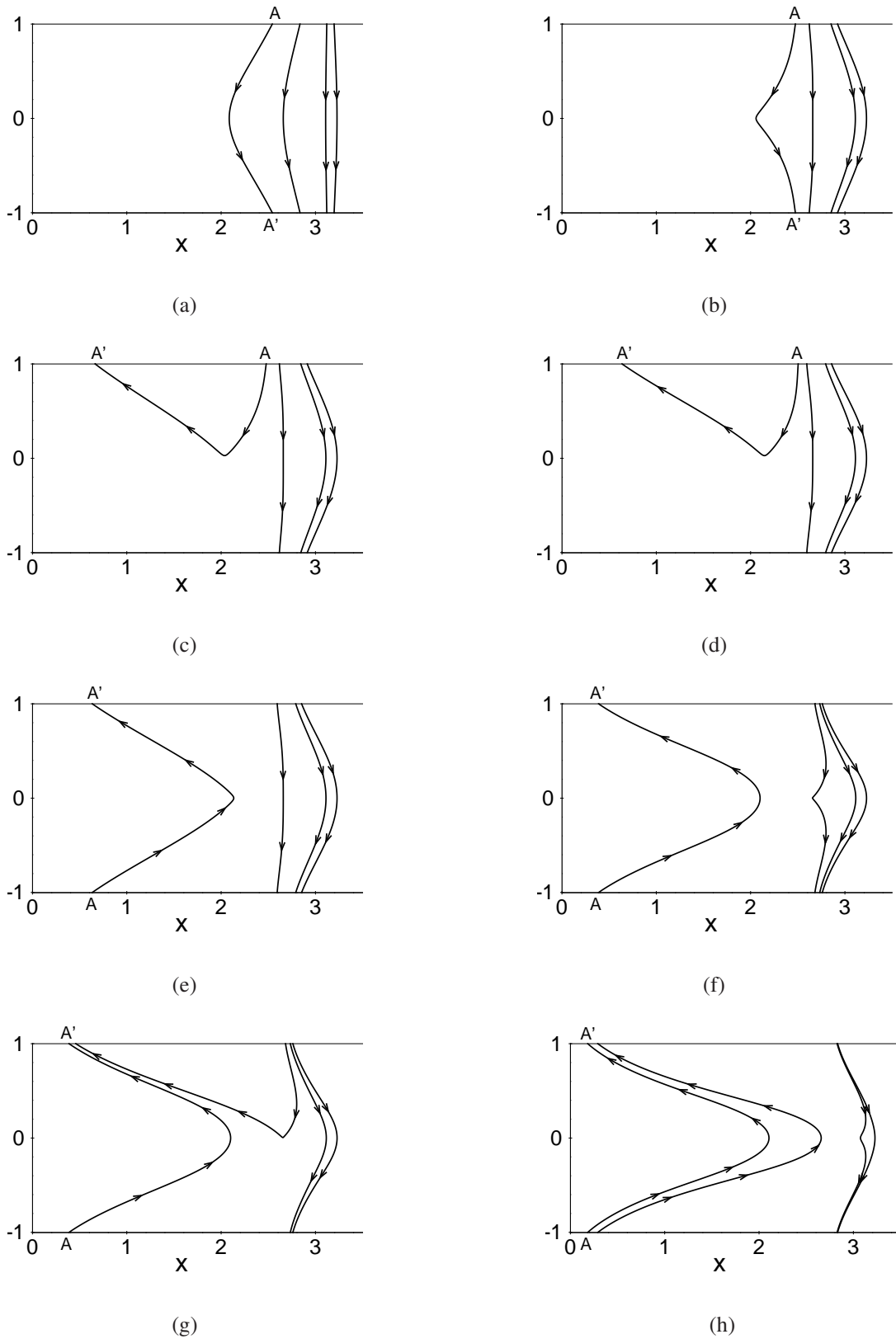


Figure 5.7: Severing and reconnection of magnetic field lines shown in a small section of the channel when the flow accelerates from rest. (a) $t = 0$, (b) $t = 2.0$, (c) $t = 2.1$, (d) $t = 2.9$, (e) $t = 3.0$, (f) $t = 15.4$, (g) $t = 15.5$, (h) $t = 37.0$. Parameters are $Q = 0.5$, $\beta = 1$, $\kappa = 1$ and $\varepsilon = 5 \times 10^{-3}$. Following the line marked AA' shows a characteristic reconnection and stretching pattern that it undergoes leading to the expulsion of magnetic flux in the core.

5. Flux Expulsion

magnetic field becomes large. This leads to significant magnetic diffusion and results in the reconnection of the field lines (Sweet [1956]). Flux expulsion can be observed in Fig. 5.6, where snapshots of the configuration of the magnetic field lines show the eventual decay of magnetic flux in the core and significant shifting (advection) of the X-points, due to reconnection events (the mean flow is from left to right). A specific

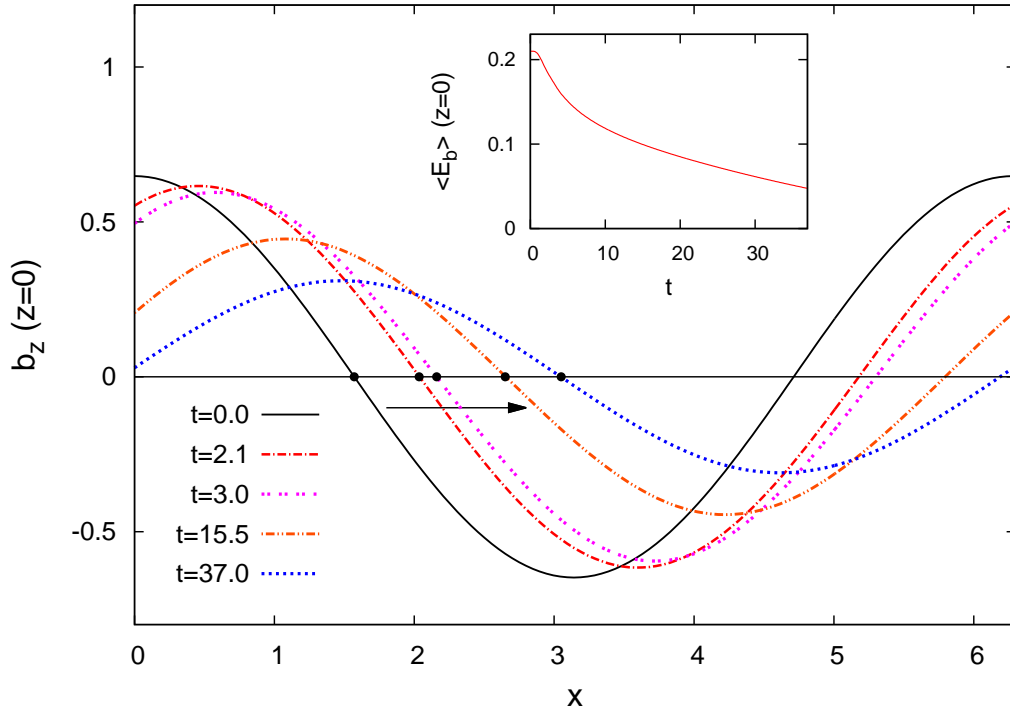


Figure 5.8: Evolution of the wall normal component of the magnetic field (b_z) along the channel centerline $z = 0$ when the flow accelerates from rest (obtained from DNS). Parameters are $\beta = 1$, $Q = 0.5$ and $\varepsilon = 5 \times 10^{-3}$. Inset shows corresponding time decay of the mean magnetic energy on the centerline $\langle E_b \rangle$ at $z = 0$. We mark the magnetic X-points and their steady shift further downstream by reconnection events.

common pattern in the reconnection of the magnetic field lines was observed during the process of dynamic runaway. A field line in the region with a strong negative wall normal component b_z (those that are approximately located at $2.5 < x < \pi$ in Fig. 5.6(a)), undergo a two-fold reconnection process and transform into a field line with positive b_z (except at the core, where it is zero). A typical example of this is shown in more detail in Fig. 5.7, where the field line (marked at the ends by A and A') corresponding to the imposed magnetic field initially develops a sharp 'pinch' at $z = 0$ (Fig. 5.7(b)) before a reconnection event leading to both ends of the line attached to the top wall (Fig. 5.7(c)). After some further stretching, another reconnection event occurs as seen from Fig. 5.7(d) to Fig. 5.7(e) leading to a reversal of the direction of the magnetic field as compared to the initial state. Subsequently the field line is stretched significantly in the flow direction as shown from Fig. 5.7(d) through Fig. 5.7(h) leading to the final

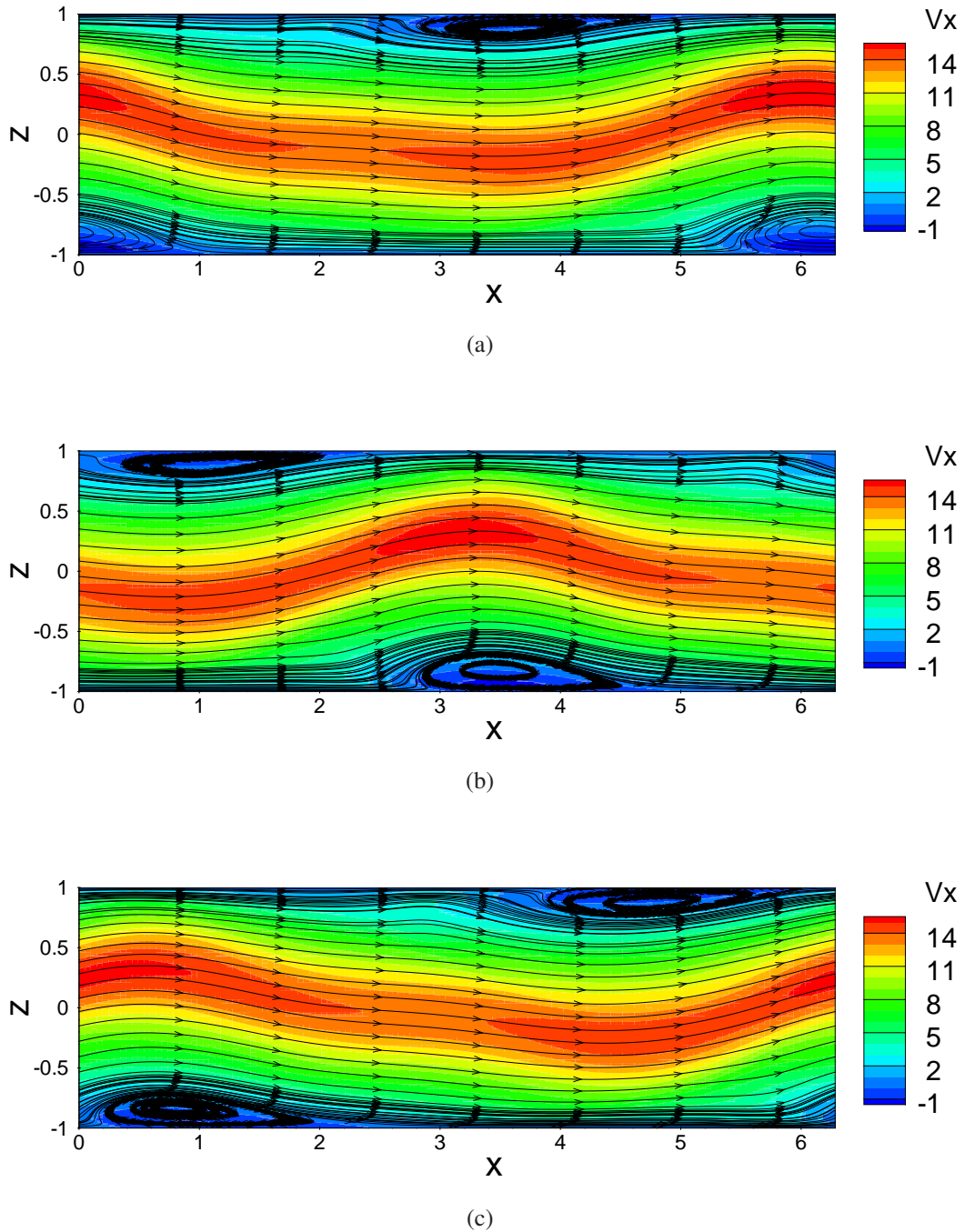


Figure 5.9: Snapshots of streamlines of the velocity field in the final (steady on average) state showing the transport of vortices near the wall. Coloured by contours of v_x . (a) $t = 0.3$, (b) $t = 1.1$, (c) $t = 1.9$. Parameters are $Q = 0.5$, $\beta = 1$, $\kappa = 1$ and $\varepsilon = 5 \times 10^{-3}$.

topology of the line that also results in $b_z = 0$ at $z = 0$. Interestingly, these series of events is seen to occur to every flux line (in the region considered, $2.5 < x < \pi$) in a sequential manner from left to right. This is clearly seen from the pinching and reconstructions occurring to the field line next to AA' seen from Fig. 5.7(f) through Fig. 5.7(h).

The decay of the magnetic flux in the core during this period (from $t = 0$ to $t = 37$) is shown in Fig. 5.8, where the evolution of $b_z(x)$ along the channel centerline is plotted. Advection of X-points in the streamwise direction and the decay of the amplitude of b_z can be clearly observed. This is accompanied by the temporal decay of the mean magnetic energy at the channel centerline which is defined as

$$\langle E_b \rangle = l_x^{-1} \int_0^{l_x} (b_x^2 + b_z^2) dx. \quad (5.17)$$

This decay contributes to the growth of kinetic energy and hence the runaway process.

As mentioned previously, the final state occurring in the Poiseuille regime shows a strongly unsteady behavior, with secondary flow structures which become more frequent at lower viscosities. A typical example is shown in Fig. 5.9, where two large vortex structures are observed, one on either wall and separated in the streamwise direction. These vortices (or recirculation zones) are advected along the mean flow (Figs. 5.9(a) through 5.9(c)), leading to an almost time-periodic behavior of the flow. Absence of chaotic states might be attributed to low Reynolds numbers and short domain length in the problem.

5.3.3 Comparison with the predictions of KM82

We now turn to the comparison of DNS results with the model results of KM82 to investigate the validity of the model in predicting the steady states in both the regimes and also the location of bifurcation that leads to the transition between the two regimes. All the comparisons shown in this subsection correspond to $\varepsilon = 5 \times 10^{-3}$, $\beta = 1$ and $\kappa = 1$ with a channel length $L_x = 2\pi$. Fig. 5.10 shows the mean streamwise velocity profiles in the Hartmann regime compared to the prediction of KM82 at various values of the parameter Q . It can be observed that the model is accurate in this regime in terms of the magnitude of axial velocity although some differences can be seen in the shape of the profiles.

However this is in contrast to the behavior in the Poiseuille regime (see Fig. 5.11), where the model strongly underpredicts the axial velocity v_x and significant differences are observed in the shape of the velocity profiles. These differences can be attributed to the effect of non-linearity which is more pronounced in the Poiseuille regime and the fact that the non-linear terms are neglected in the model equations of KM82. It must be pointed out that in the case of Poiseuille regime, as the final state of the flow is strongly time-dependent, the axial velocity profiles from the DNS are obtained by time and streamwise averaging.

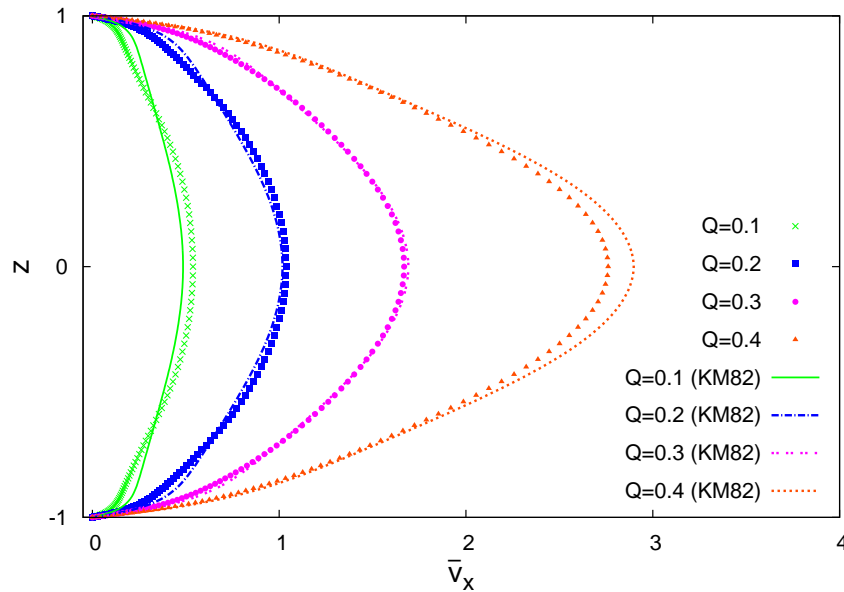


Figure 5.10: Steady state mean streamwise velocity profiles in the Hartmann regime. Parameters are $\beta = 1$, $\kappa = 1$ and $\varepsilon = 5 \times 10^{-3}$.

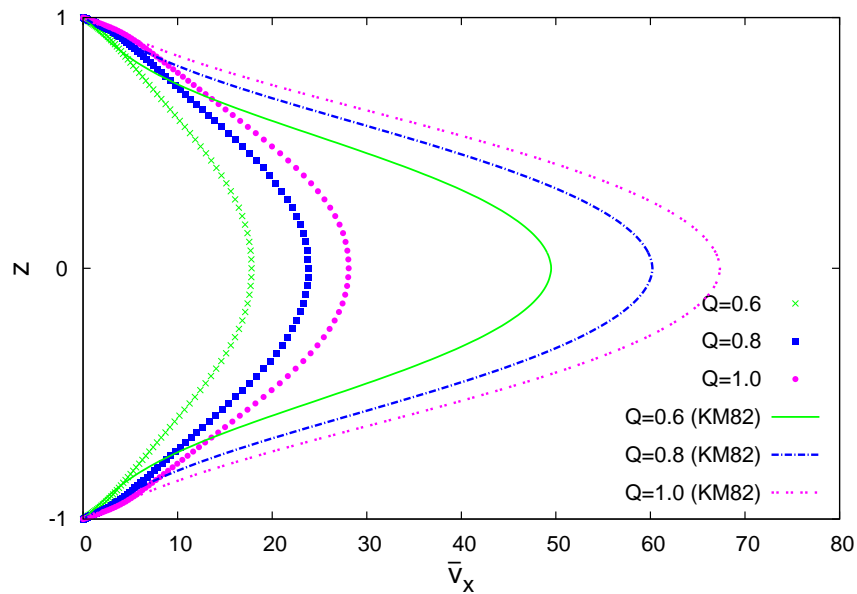


Figure 5.11: Mean streamwise velocity profiles in the Poiseuille regime (streamwise and time averaged). Parameters are $\beta = 1$, $\kappa = 1$ and $\varepsilon = 5 \times 10^{-3}$.

The dependence of the core axial velocity ($U_c = v_x$ at $z = 0$) on Q is shown in Fig. 5.12. The bifurcation from the Hartmann regime to the Poiseuille regime is observed at $Q \sim 0.43$, which is very close to that predicted by KM82 and the shape of the curve is in close match. The fact that non-linearity leads to the differences is confirmed through a simulation that we performed dropping out the non-linear term $(\beta\kappa)^{-1}(\mathbf{v} \cdot \nabla)\mathbf{v}$ in equation (5.5). Figure. 5.12 shows that the curve obtained from

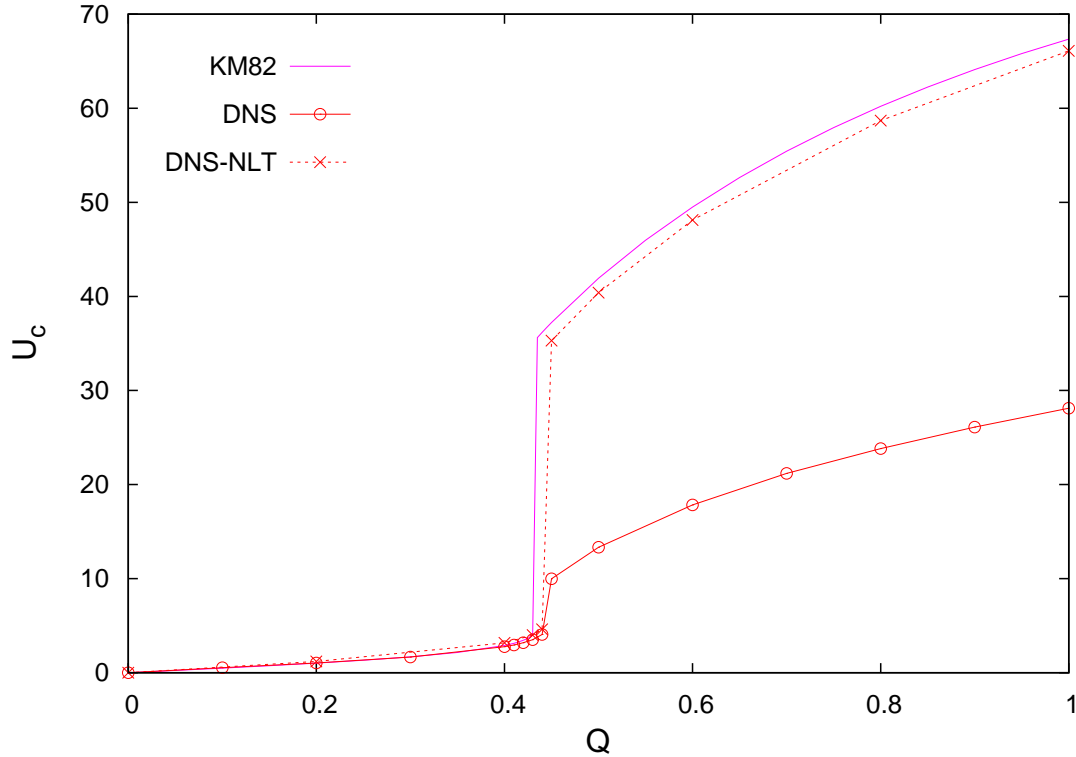


Figure 5.12: Comparison of DNS results with the model predictions for $\varepsilon = 5 \times 10^{-3}$, $\beta = 1$ and $\kappa = 1$. The dotted line (denoted as DNS-NLT) indicates results obtained from DNS by excluding the non-linear term.

DNS without the non-linear term tends very close to that of KM82.

5.3.4 Effect of parameters ε , β and κ

In this subsection, we present the effect of the parameters ε , β and κ on the nature and location of the bifurcation along with the magnitude of core velocity in the final state. Fig. 5.13 shows U_c versus Q at different values of ε . It is clear that at higher values of ε or lower Reynolds numbers, the transition from the Hartmann to Poiseuille regimes does not show a distinct jump but rather occurs in a continuous manner. In the parameter space with a clear bifurcation, the value of Q at which the jump occurs is almost independent of the hydrodynamic Reynolds number (or ε). In addition, when ε is low, a two-valued solution or hysteresis is observed near the bifurcation point (e.g. near $Q \sim 0.43$ for $\varepsilon = 5 \times 10^{-3}$), depending on whether the steady state is approached by increasing Q or decreasing Q . Such a hysteresis effect was also predicted by KM82.

The effect of ε on the core velocity (U_c) is negligible in the Hartmann regime but is strong in the Poiseuille zone. All these observations are akin (qualitatively) to the predictions of KM82. Interestingly, the effect of the magnetic Reynolds number β on the U_c - Q curve is very similar to that of the hydrodynamic Reynolds number, with

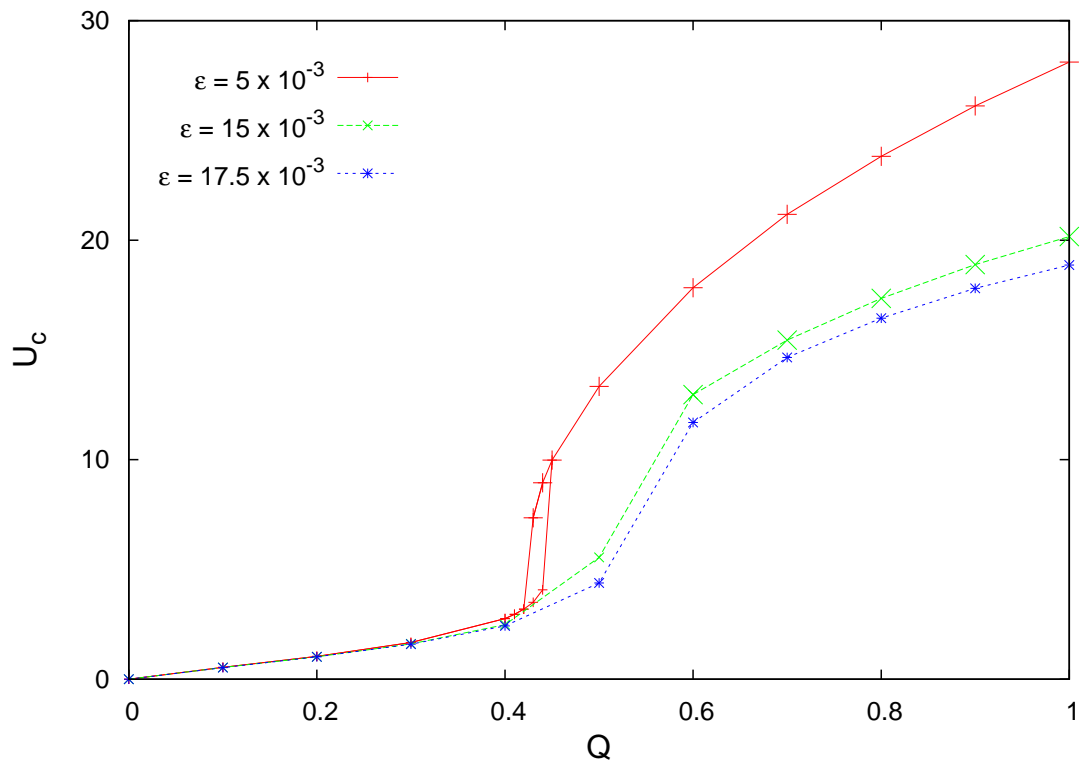


Figure 5.13: Streamwise core velocities U_c as a function of Q obtained from DNS for various values of ε . Dotted lines indicate that no hysteresis is observed. Parameters are $\beta = 1$ and $\kappa = 1$.

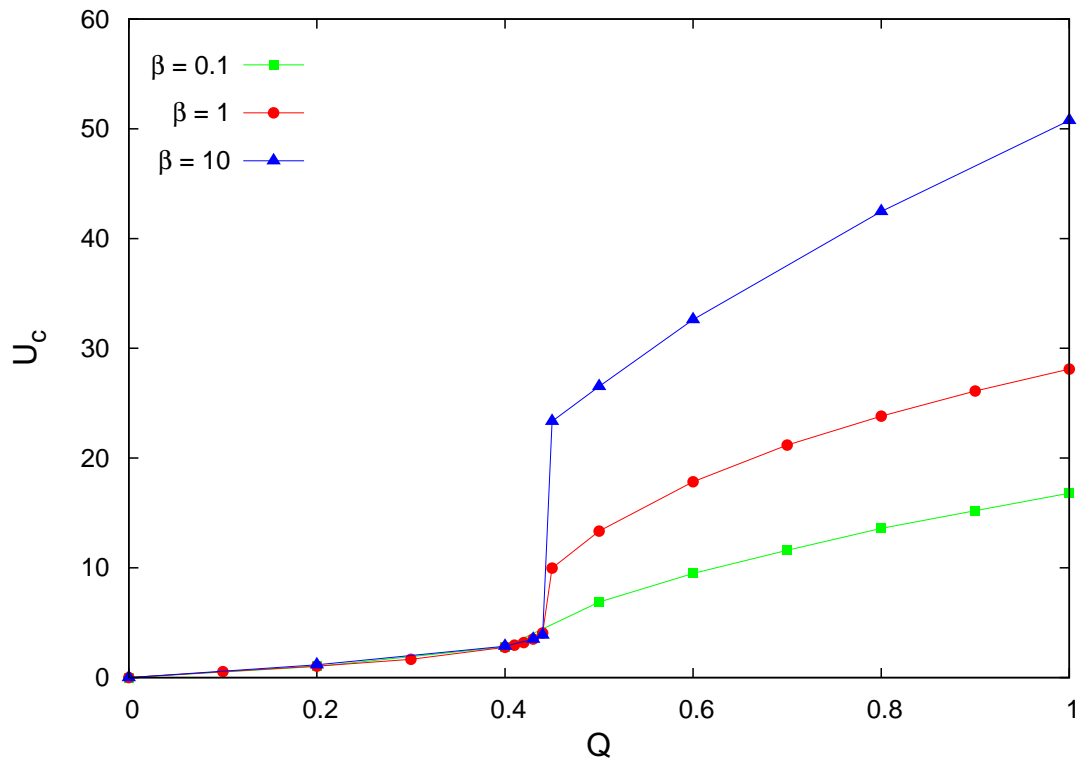


Figure 5.14: Effect of variation of magnetic Reynolds number β in the U_c - Q plane, obtained from DNS. Parameters are $\kappa = 1$ and $\varepsilon = 5 \times 10^{-3}$.

5. Flux Expulsion

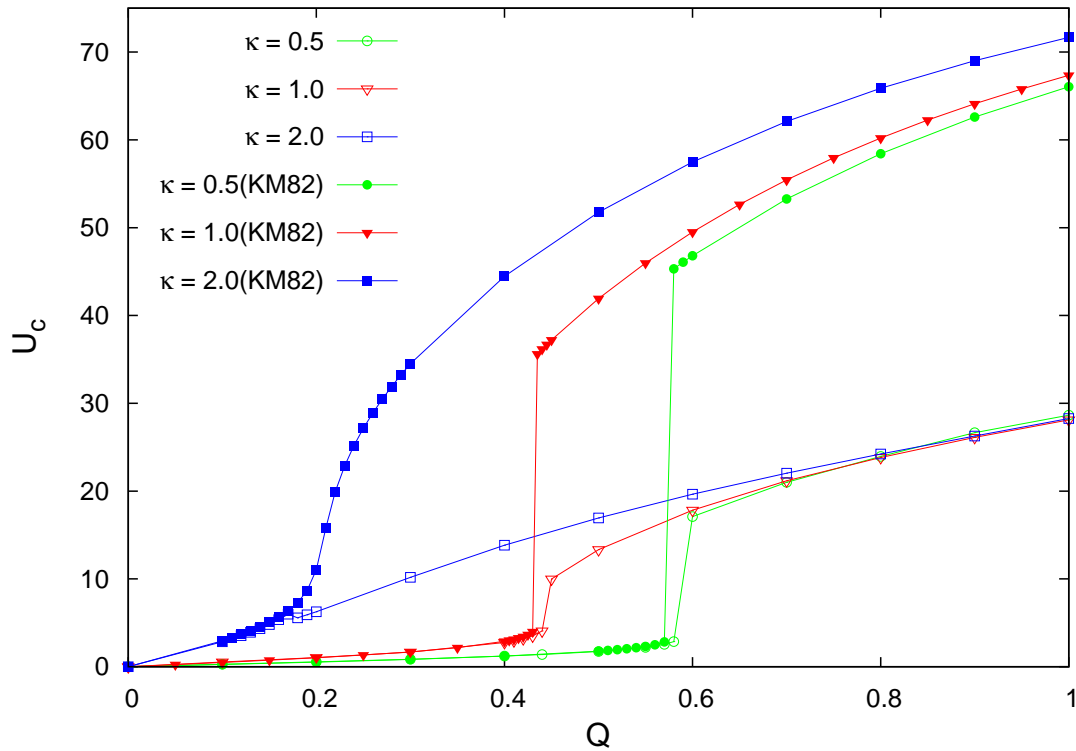


Figure 5.15: Effect of variation of streamwise wavenumber κ of the imposed magnetic field, obtained from DNS and KM82. Parameters are $\beta = 1$ and $\varepsilon = 5 \times 10^{-3}$.

higher levels of flux expulsion and core flow occurring at higher values of β , as can be seen in Fig. 5.14. It is interesting to note that steady state solutions of KM82 are independent of the magnetic Reynolds number due to the association of β with only the non-linear term (which is neglected in the model) in the momentum balance, as can be seen from equations (5.5) and (5.14). Furthermore, the location of the bifurcation to the Poiseuille regime is almost unaffected by variations in ε or β . In contrast, the jump is observed to be very sensitive to the streamwise wavenumber (κ) of the imposed magnetic field b_0 . This is shown in Fig. 5.15, indicating a clear increase in the value of Q at which the bifurcation occurs and also the magnitude of the jump when κ is decreased. This is very similar to the dependence on κ predicted by the inviscid version of KM82 (not shown in the plot), i.e. by using $\varepsilon = 0$ in equation (5.14). In specific, for $\kappa = 0.5$, inviscid KM82 predicts $Q_c \approx 0.55$ as compared to $Q_c \approx 0.59$ from viscous KM82 and $Q_c \approx 0.6$ obtained from DNS with $\beta = 1$ and $\varepsilon = 5 \times 10^{-3}$. At a higher wavenumber ($\kappa = 2$), KM82 in the inviscid limit predicts a jump at a value of $Q_c = 0.15$ whereas the viscous KM82 shows a continuous transition between the two regimes. Interestingly in this case ($\kappa = 2$), DNS shows no clear demarcation between the Hartmann and the Poiseuille regimes, although a very small fall (rather than a jump) in U_c is observed when Q is increased from 0.17 to 0.18 and a corresponding onset of

near wall recirculation zones at $Q = 0.18$.

In this chapter, we presented results of direct numerical simulations of the dynamic runaway effect due to flux expulsion in a plane channel MHD flow. General features of the flow and magnetic fields in the two regimes - the Hartmann and Poiseuille regimes - were studied.

5. Flux Expulsion

Chapter 6

Turbulence in Hartmann duct flow at low and moderate Reynolds numbers

6.1 Turbulence at low Reynolds number

In this section, we study the properties of a turbulent duct flow in the presence of a uniform wall normal magnetic field at moderate magnetic Reynolds numbers $R_m = 50$ and $R_m = 100$ and at a low hydrodynamic Reynolds number $Re = 5000$. We study the effect of R_m on the evolution of turbulence at relatively low Hartmann number as well as on the relaminarization of the flow at Hartmann numbers close to the threshold values. The aim of this study is to obtain a sense of the impact of R_m on turbulent Hartmann duct flow. A comprehensive study of the dependencies on R_m in larger Reynolds number and Stuart number flows will be taken up in the next section. For this purpose, a purely hydrodynamic turbulent duct flow in a domain of size $4\pi \times 2 \times 2$, that has evolved to a statistically steady state, is chosen as the initial state and a uniform magnetic field along the z -direction, $\mathbf{b}_0 = b_0 \hat{k}$ is imposed on the flow. The subsequent evolution of the velocity and magnetic fields are computed on a grid size of $256 \times 192 \times 192$, with an equal grid stretch factor in the y and z directions, $S_y = S_z = 1.8$. It must be noted that, in practice when a magnetic field (generated by external current sources) is applied onto a conducting flow at finite magnetic Reynolds number, the field diffuses at a rate proportional to $\sqrt{\lambda}$, unlike the case of a low R_m flow where the magnetic field diffuses instantly (relative to the time scales relevant to this problem) throughout the conducting medium. However, in order to have an initial state that allows direct comparison with the low R_m case, we assume here that an initial uniform magnetic field is present throughout even in the case of flows with moderate R_m .

6.1.1 Relaminarization threshold

Transition from a laminar flow to a turbulent flow or vice versa and the critical parameters at which this happens in Hartmann duct and channel flows have been of significant interest right from the time Hartmann performed his first experimental studies in 1937 (Hartmann & Lazarus [1937]). One of the reasons for this is the significant impact that transition to turbulence can have on quantities of engineering interest like the skin friction factor. Since then, numerous experiments and several numerical studies have been conducted that lead to a better understanding of transition in Hartmann duct and channel flows at low magnetic Reynolds numbers (see e.g. Kobayashi [2008]; Krasnov *et al.* [2013]; Murgatroyd [1953]; Reed & Lykoudis [1978]). However, the effect of finite magnetic Reynolds number on the suppression of duct flow turbulence by a magnetic field is unknown, which we explore here. To this end, we simulate the evolution of a turbulent duct flow at $Re = 5000$ in the presence of a uniform initial mag-

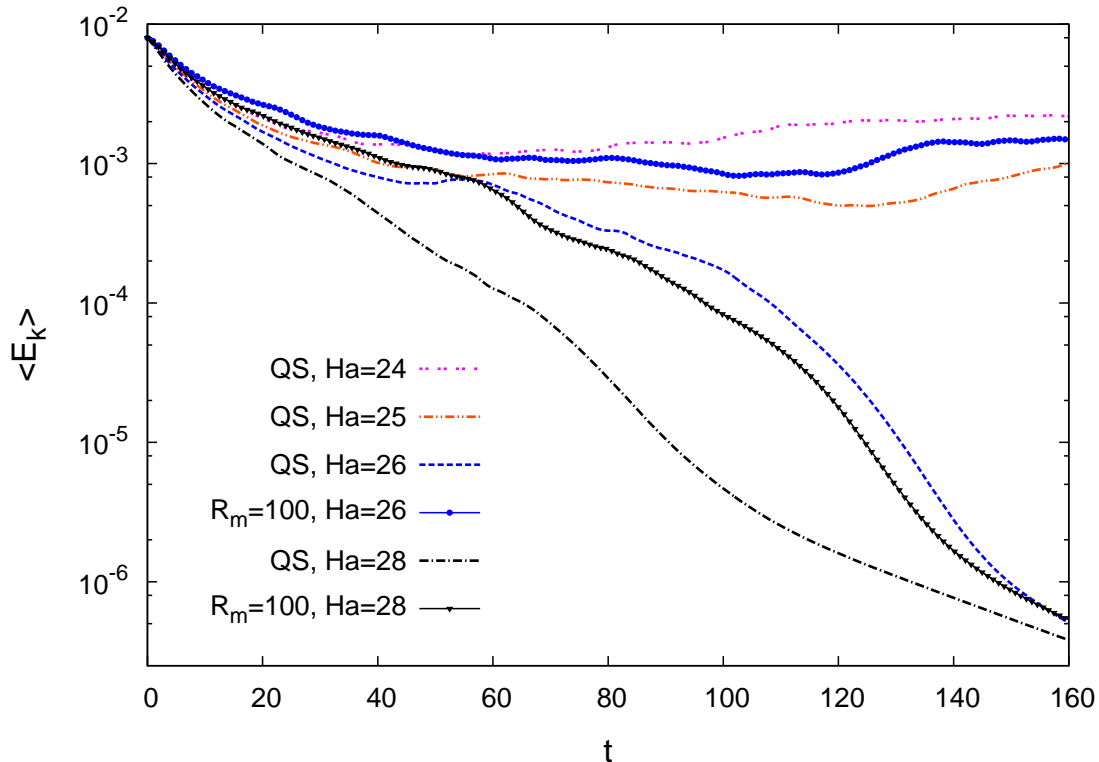


Figure 6.1: Evolution of turbulent kinetic energy $\langle E_k \rangle$ at $Re = 5000$ and Hartmann numbers close to the relaminarization threshold.

netic field at $R_m = 100$ and at Hartmann numbers close to the critical values ($Ha \approx 25$) obtained from quasistatic (QS) DNS ($R_m \ll 1$) studies performed by Krasnov *et al.* [2013]. It is observed from the QS simulations that the flow becomes laminar between $Ha = 25$ and $Ha = 26$, which can be clearly seen in Fig. 6.1 from the near exponential decay of turbulent kinetic energy $\langle E_k \rangle$ to negligible values when $Ha = 26$. Turbulent

kinetic energy is defined in this case as

$$\langle E_k \rangle(t) = \frac{1}{4l_x} \int_0^{l_x} \int_{-1}^1 \int_{-1}^1 \frac{(v_x'^2 + v_y'^2 + v_z'^2)}{2} dx dy dz, \quad (6.1)$$

where the velocity fluctuation $\mathbf{v}' = [v_x', v_y', v_z']$ is defined as

$$\mathbf{v}' = \mathbf{v} - l_x^{-1} \int_0^{l_x} \mathbf{v} dx \quad (6.2)$$

(it must be noted that the definition of velocity fluctuation used here involves subtracting a time dependent mean velocity and does not correspond to a typical Reynolds decomposition. However, it is expected that the present definition is a reasonably good approximation of the fluctuation). Furthermore, the flow is also observed to laminarize for all cases of $Ha > 26$, for example at $Ha = 28$ shown in Fig. 6.1.

However, when $R_m = 100$ the flow remains turbulent at $Ha = 26$, shown by the settling of $\langle E_k \rangle$ in contrast to the QS case. This can also be observed from the instantaneous axial velocity profiles shown in Fig. 6.2(b) and Fig. 6.2(c) where the QS case shows almost complete laminarization at $t = 122$ while the $R_m = 100$ case shows turbulent Shercliff layers. Nevertheless, with a slightly stronger magnetic field ($Ha = 28$), at $R_m = 100$, turbulence is completely suppressed as in the QS case but with a slower rate of decay. This is further evident from Fig. 6.2(d) and Fig. 6.2(e), with the $R_m = 100$ case showing much higher intensity of turbulence in the Shercliff layers at $t = 46$ as compared to the QS case. From these observations, it seems very likely that in the low Re regime, a higher R_m tends to sustain turbulence and hence delays the laminarization threshold to a higher value of Hartmann number. This behavior can be attributed to the independent dynamics of the magnetic field that reduces dissipation and hence delays the energy decay.

6.1.2 Turbulence at lower Hartmann number

In this subsection, we discuss a few features of the evolution of the turbulent flow at $Re = 5000$ and a relatively low Stuart number, corresponding to a Hartmann number $Ha = 15$. This is performed at $R_m = 50$ and $R_m = 100$ along with the quasistatic case. In Fig. 6.3(a), the decay of turbulent kinetic energy with time is shown until $t = 140$. It is observed that the initial phase until around $t = 30$ shows a lower decay rate with higher R_m . However, the flow apparently reaches a statistically steady state earlier in the quasistatic case as compared to the cases with higher R_m , which show a low

6. MHD turbulence

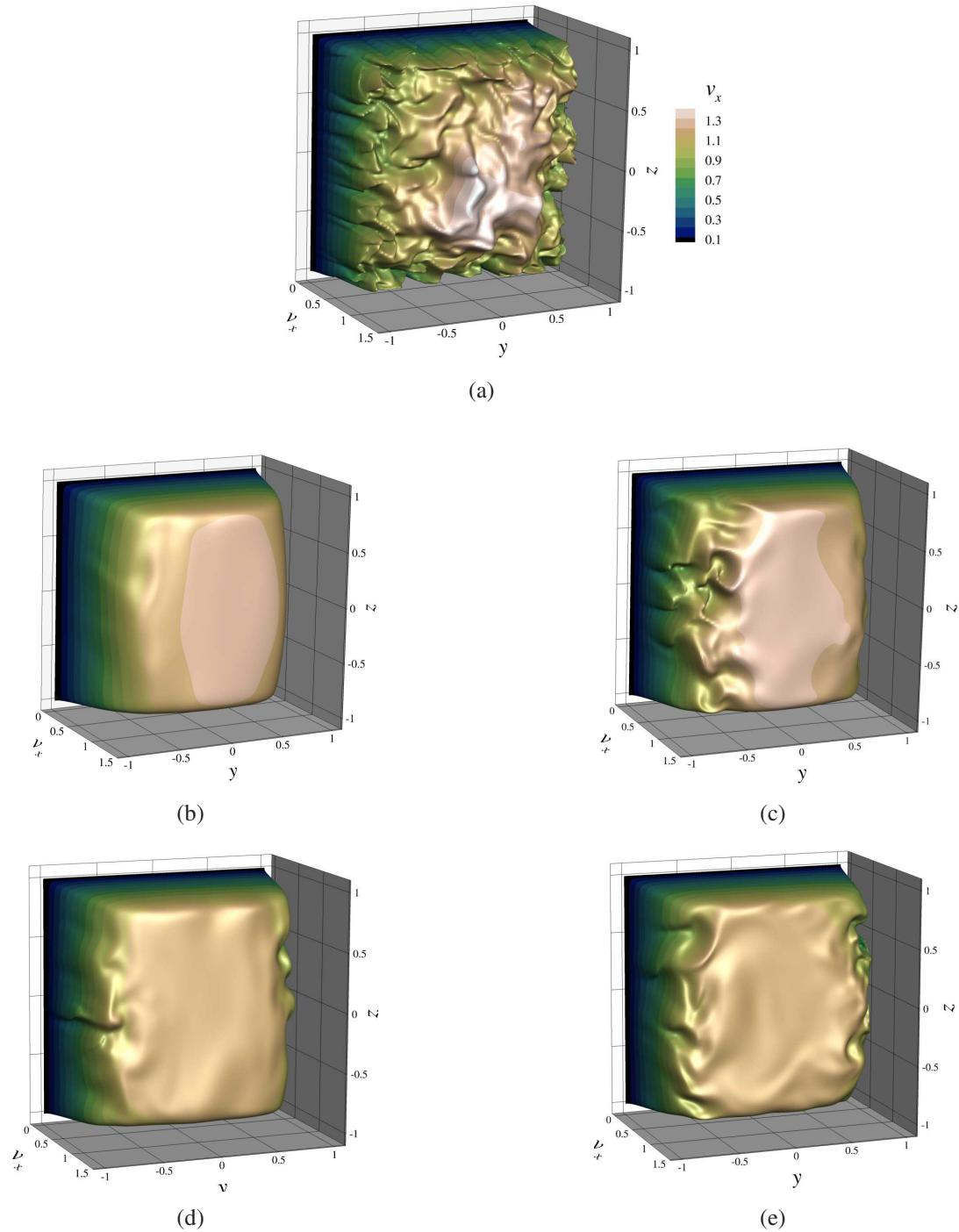


Figure 6.2: Instantaneous axial velocity profiles at $x = l_x/2$. (a) Initial state at $t = 0$ without the magnetic field, (b) $Ha = 26$, $R_m = 0$ at $t = 122$, the flow is almost laminarized, (c) $Ha = 26$, $R_m = 100$ at $t = 122$, the Shercliff layers continue to be turbulent, (d) $Ha = 28$, $R_m = 0$ at $t = 46$, (e) $Ha = 28$, $R_m = 100$ at $t = 46$.

frequency oscillatory behavior after the initial steep transients. This is in line with the findings of Knaepen *et al.* [2004] through DNS at $1 \leq R_m \leq 20$ in a periodic box.

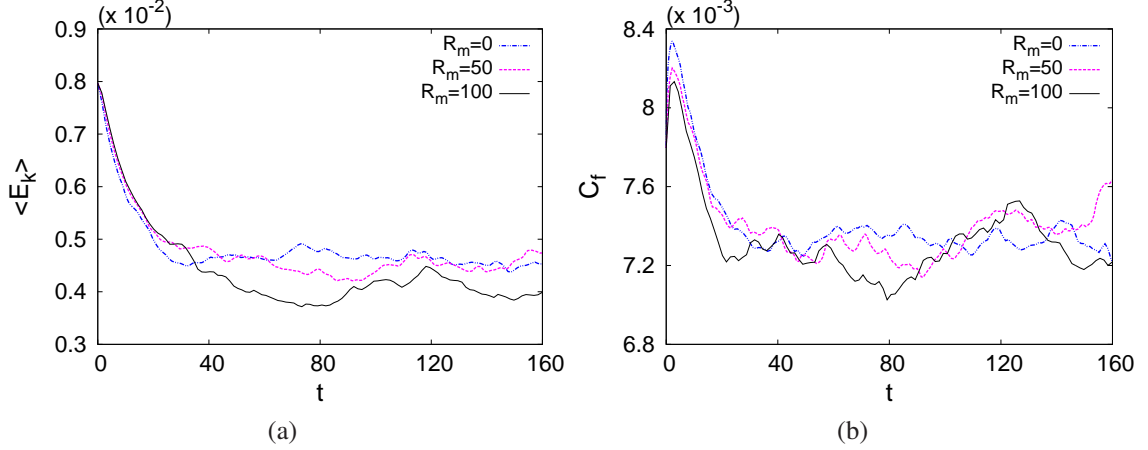


Figure 6.3: Time evolution of (a) turbulent kinetic energy $\langle E_k \rangle$ and (b) skin friction coefficient C_f . Common parameters are $Re = 5000$ and $Ha = 15$.

In addition, the evolved state seems to settle at turbulent energy levels roughly the same, independent of R_m . The reason for this is not fully clear and could be attributed to a low value of Stuart number or to the low variability in the magnetic field allowed due to the uniformity in the imposed magnetic field.

It is known from quasistatic MHD that the Hartmann flow has two opposing effects namely the Hartmann flattening and turbulence suppression effects that determine the evolution of skin friction coefficient under the application of a magnetic field. This can be observed from the corresponding behavior of skin friction coefficient defined as

$$C_f = \frac{1}{4Re} \int_{\Gamma} -\frac{\partial \bar{v}_x}{\partial n} dl, \quad (6.3)$$

(\bar{v}_x being the mean axial velocity and n the wall normal direction) which is shown in Fig. 6.3(b). An initial increase in C_f occurs until around $t = 2.3$ due to the dominance of the Hartmann flattening followed by a decrease in C_f when suppression of turbulence becomes important. Such a qualitative behavior is unaffected by the magnetic Reynolds number, although a slight increase in the magnitude of the peak is observed. Finally, the oscillatory behavior at higher R_m is also seen with C_f as in the case of turbulent kinetic energy.

The effect of R_m on the suppression of turbulence by the magnetic field can be observed from the instantaneous cross-sectional distribution of Reynolds stress tensor component $\langle v_z'^2 \rangle_x$, shown at $t = 80$ in Fig. 6.4. Our first studies indicate clearly that with increasing R_m , the stress component is increasingly suppressed in the core region close to the Hartmann layer.

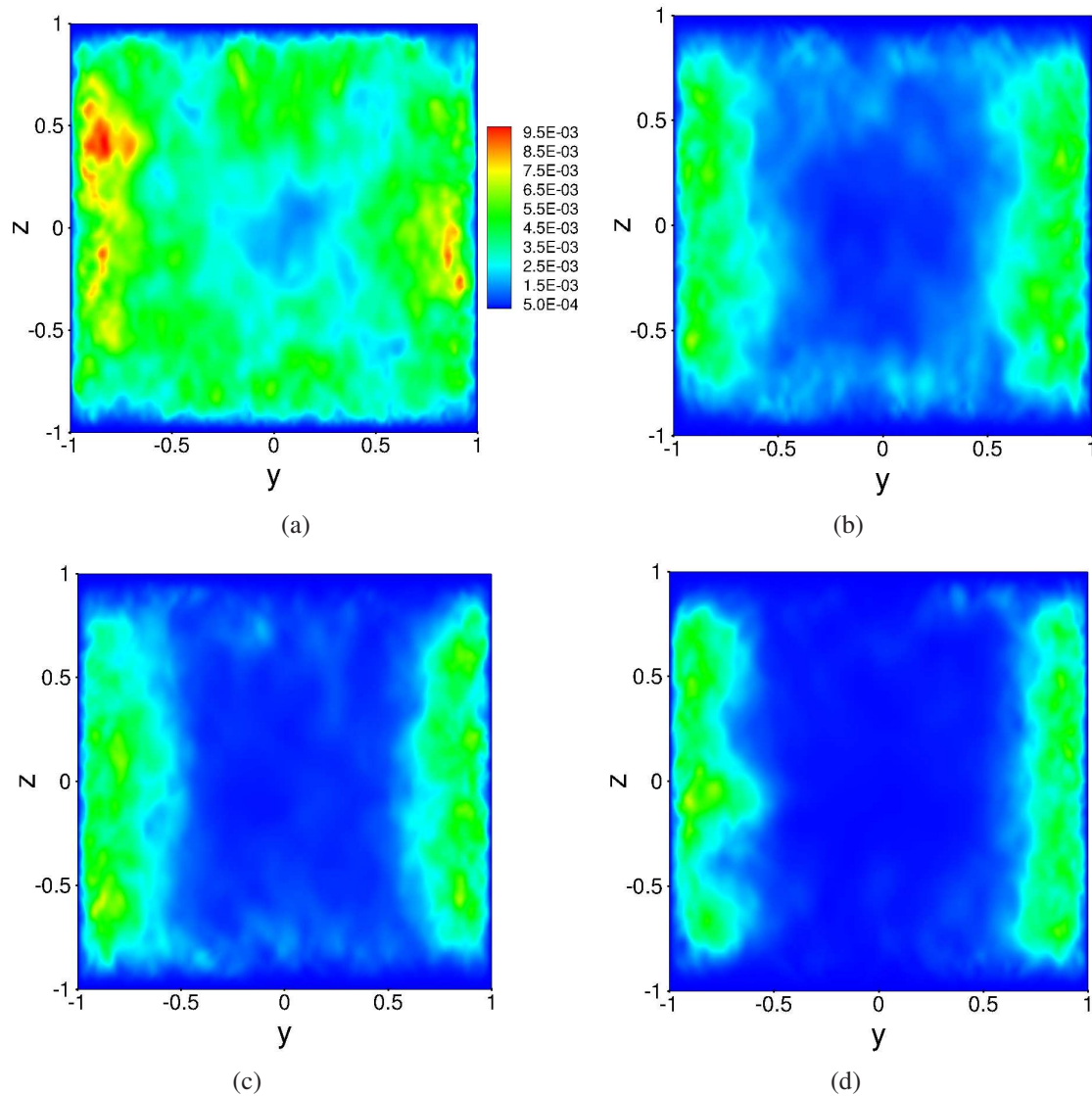


Figure 6.4: Suppression of the Reynolds stress component $\langle v_z'^2 \rangle_x$ due to the applied magnetic field at $t = 80$. (a) Common to all the three cases at $t = 0$; (b) quasistatic case, $R_m = 0$, (c) $R_m = 50$ and (d) $R_m = 100$. Common parameters are $Re = 5000$ and $Ha = 15$.

6.2 Turbulence at moderate Reynolds number

In the previous section, a preliminary investigation was conducted to obtain a sense of the effect of R_m on very low Re turbulence. In this section, we take it a step further by performing a more detailed study of MHD turbulence in a Hartmann duct flow at moderate Re and R_m . In particular, we study the effect of R_m on the statistically steady states obtained when a pure hydrodynamic turbulent flow in a duct is subjected to a uniform magnetic field.

6.2.1 Parameters and grid sensitivity

We choose a Reynolds number $Re = 14500$ and a Hartmann number $Ha = 43.5$ for this purpose. The choice is driven by the availability of results for low R_m (quasistatic) Hartmann duct flow in the form of LES results by Kobayashi [2008]. Hence, wherever possible we shall make a comparison between our DNS at $R_m = 0$ and LES results by Kobayashi (this will be done with the DNS results without filtering). It must be noted that in this parameter space ($R = Re/Ha \approx 333$), turbulence in the duct at low R_m is limited to the side layers, whereas the Hartmann layers and the core region are laminar. This is confirmed from the results of Kobayashi [2008]. Here, two different moderate values of $R_m = 400$ and $R_m = 2000$ have been chosen along with baseline quasistatic case $R_m = 0$. Further, the duct cross-section is chosen of size 2×2 and the streamwise length is either 4π or 2π . The shorter length has been used in some simulations in order to reduce the computational overhead, which is very high for DNS at moderate R_m . The reason for this will be apparent shortly. The grid resolution in the cross-section was taken to be 192×192 with an equal stretch factor of $S = 2.0$. The streamwise grid resolution is $N_x = 1024$ when the duct length is 4π and $N_x = 512$ when the duct length is 2π . These resolutions were chosen through grid independence tests that were performed using quasistatic DNS for both the streamwise and cross-sectional resolutions separately. This is shown in Fig. 6.5(a) and Fig. 6.5(b), that shows the convergence of the statistically steady skin friction coefficient as the grid resolution is increased beyond a certain level. That the shorter streamwise duct length $l_x = 2\pi$

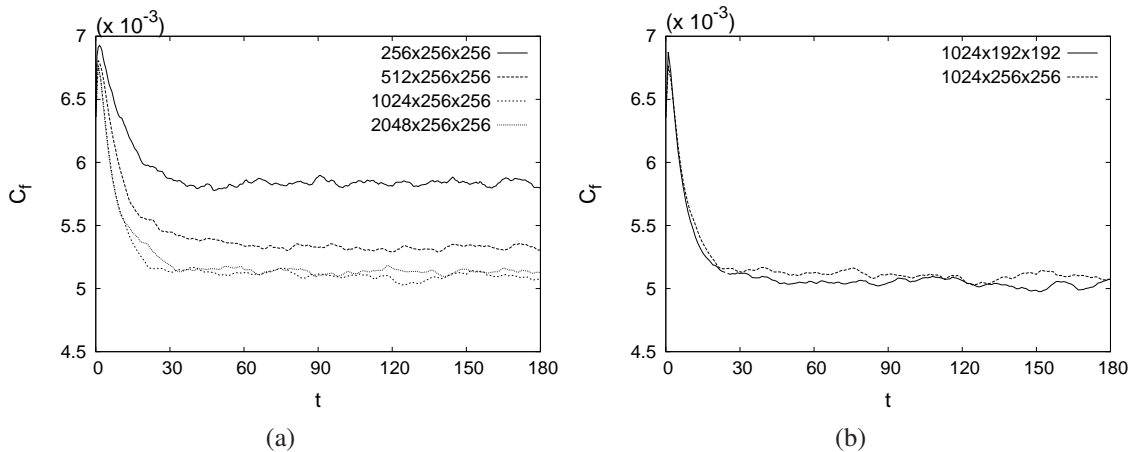


Figure 6.5: Sensitivity of the statistically steady skin friction coefficient with a) streamwise grid resolution and b) cross-sectional grid resolution. Domain size: $4\pi \times 2 \times 2$. Parameters are $R_m = 0$, $Re = 14500$ and $Ha = 43.5$.

is already sufficient is confirmed from the clear decay of the two-point correlations (along the streamwise direction) of the velocity component fluctuations. This is shown in Fig. 6.6. The correlation coefficient $C(x')$ is defined for the velocity component v_i

as

$$C(x') = \frac{1}{T} \int_0^T \left(\frac{1}{l_x/2} \int_0^{l_x/2} v_i(x) v_i(x+x') dx \right) dt. \quad (6.4)$$

In our case, the time averaging has been done over 2500 snapshots that are spaced at 0.1 convective time units. One can observe that the velocity fluctuations are completely decorrelated within a distance of π .

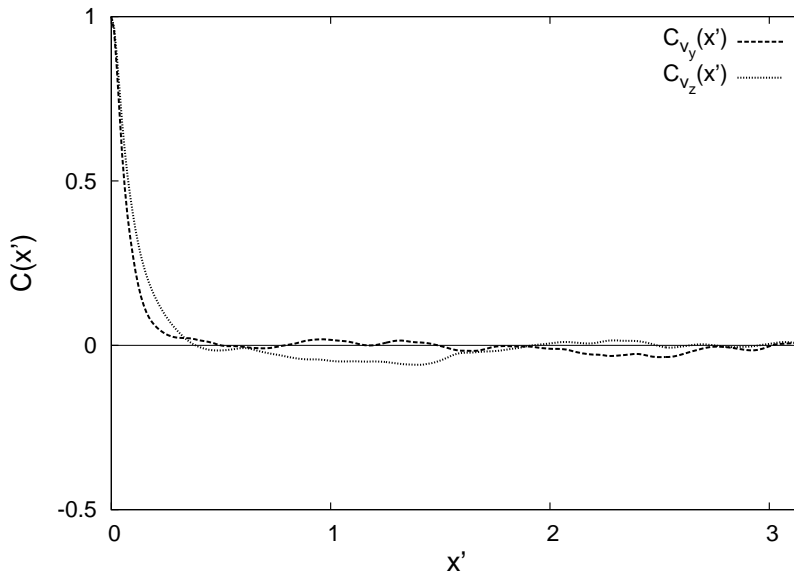


Figure 6.6: Two-point correlations of the cross stream velocity fluctuations at the location $(y,z) = (0.7, 0.0)$ in the Shercliff layer as a function of the streamwise separation. The domain length $l_x = 2\pi$. Parameters are $R_m = 0$, $Re = 14500$ and $Ha = 43.5$.

6.2.2 Flow structure at different values of R_m

We first look into the possible change in the turbulent flow structure that might arise when R_m is increased. From the basic studies performed at low Re in the previous section, one could expect that when R_m is increased, the flow might show some turbulent behavior at locations where it is initially laminar. This is indeed the case and can be observed from the instantaneous contours of axial velocity v_x at a cross-section shown in Fig. 6.7. These are obtained when the flow has reached a statistically steady state. One can see that the flow in the core region is almost laminar when $R_m = 0$, whereas the flow at $R_m = 400$ and $R_m = 2000$ displays a distinctly visible large scale turbulence in the core. Visualization of the time evolution of these contours (that are not shown here) showed that at $R_m = 2000$ structure of the turbulent state in the core region is more complicated since it varies significantly with time than it is in the case

of $R_m = 400$.

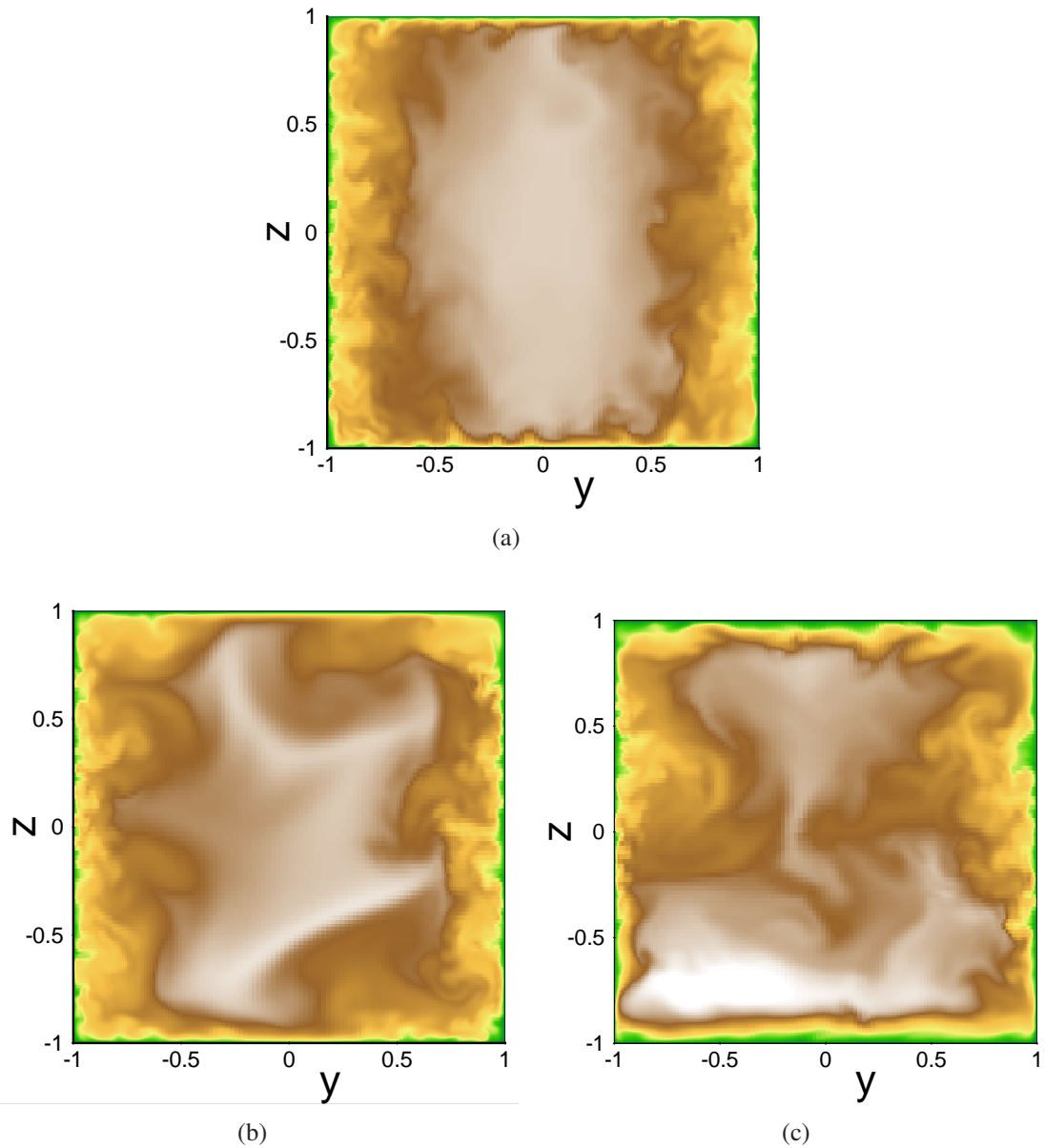


Figure 6.7: Instantaneous contours of streamwise velocity at the cross-section $x = l_x/2$ for a) $R_m = 0$, b) $R_m = 400$ and c) $R_m = 2000$. Contour coloring : light end, white ($v_x = 1.3$) and dark end, green ($v_x = 0$). Common parameters: $Re = 14500$ and $Ha = 43.5$.

6.2.3 Integral characteristics

The evolution of turbulent kinetic energy for the three different values of R_m is shown in Fig. 6.8(a). Similar to the situation with low Re , we see that with higher R_m , the time (in convective units) that the flow takes to reach the statistically steady state is much higher. For example, it took about 600 convective units of runtime in order to get convergent statistics for the simulation with $R_m = 400$ as compared to

6. MHD turbulence

about 200 convective time units for $R_m = 0$. Hence the computational overhead for the moderate R_m DNS runs is higher. Further, we also see the large amplitude and wavelength oscillatory behavior of the turbulent kinetic energy in the final states of the moderate R_m turbulent flow. The difference in the level of turbulent kinetic energy at moderate R_m is slightly higher than that at $R_m = 0$ and also does not show a clear trend. This is seen from the approximately same energy levels at which the curves of $R_m = 400$ and $R_m = 2000$ settle to. During the same time, an increase in the magnetic

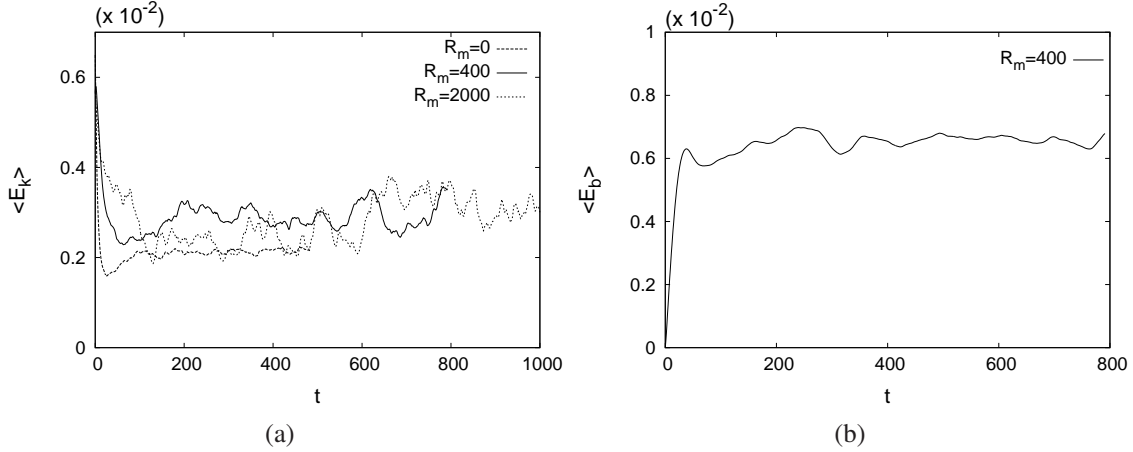


Figure 6.8: Time evolution of domain averaged a) Turbulent kinetic energy and b) Magnetic energy. Common parameters: $Re = 14500$ and $Ha = 43.5$.

energy is observed as in Fig. 6.8(b). Here the domain averaged magnetic energy is defined as

$$\langle E_b \rangle(t) = \frac{Ha^2}{4l_x Re R_m} \int_0^{l_x} \int_{-1}^1 \int_{-1}^1 \frac{(b_x^2 + b_y^2 + b_z^2)}{2} dx dy dz, \quad (6.5)$$

where we consider only the energy of the secondary magnetic field \mathbf{b} in the domain.

We now turn to the non-dimensional wall shear stresses or the skin-friction coefficients. At first, we compare the results of skin-friction coefficients from the present DNS to the LES results of Kobayashi. This is shown in the table below. Here the

Table 6.1: Comparison of skin-frictions coefficients at $R_m = 0$ between the LES results of Kobayashi and the present results from quasistatic DNS.

	LES (Kobayashi)	DNS (present study)
$C_f \times 10^3$	5.30	5.03
$C_{f,Sh} \times 10^3$	4.20	3.66
$C_{f,Ha} \times 10^3$	6.40	6.40

coefficients $C_{f,Sh}$ and $C_{f,Ha}$ are the skin-friction factors that are computed considering

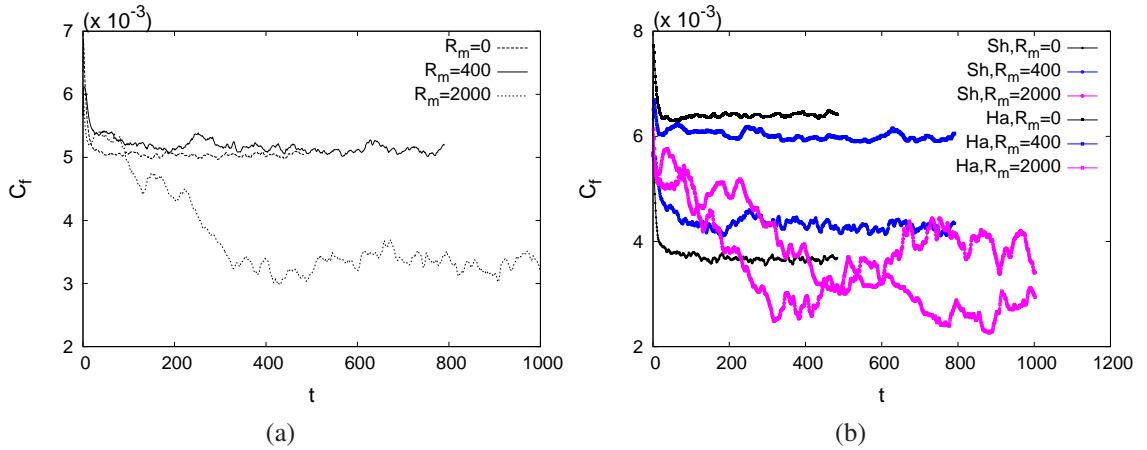


Figure 6.9: Evolution of the skin friction coefficient at different values of R_m , taking into account a) all the four walls of the duct, and b) only one pair of walls (either Shercliff or Hartmann walls) at a time.

only one set of walls (either Hartmann or Shercliff walls) at a time as

$$C_{f,Sh} = \frac{1}{Re} \int_{-1}^1 \left(\left. \frac{\partial \langle u \rangle_{x,t}}{\partial y} \right|_{y=-1} - \left. \frac{\partial \langle u \rangle_{x,t}}{\partial y} \right|_{y=1} \right) dz, \quad (6.6)$$

$$C_{f,Ha} = \frac{1}{Re} \int_{-1}^1 \left(\left. \frac{\partial \langle u \rangle_{x,t}}{\partial z} \right|_{z=-1} - \left. \frac{\partial \langle u \rangle_{x,t}}{\partial z} \right|_{z=1} \right) dy \quad (6.7)$$

and hence satisfy the relation $C_f = (C_{f,Sh} + C_{f,Ha})/2$. One can see a close match for $C_{f,Ha}$ due to the fact that the Hartmann layers are laminar in this case. However, LES slightly overpredicts $C_{f,Sh}$ as compared to the DNS. Furthermore, the effect of R_m on C_f is similar as in the case of turbulent kinetic energy, in the sense that there exists no clear trend with increase in R_m . It can be observed from Fig. 6.9(a) that C_f settles to a significantly lower value when $R_m = 2000$, whereas the value is much higher and approximately the same for $R_m = 0$ and $R_m = 400$. Taking a closer look, one can see that the reason for this behavior is actually due to two different effects occurring respectively at the Hartmann and Shercliff walls. This is shown in Fig. 6.9(b). There is a clear trend of decreasing $C_{f,Ha}$ with increase in R_m while $C_{f,Sh}$ roughly remains independent of R_m . In other words, this implies that the Hartmann flattening effect is reduced with increasing R_m , but the intensity of turbulence near the Shercliff walls does not change much.

6.2.4 Mean flow quantities, Reynolds stresses and turbulence intensities

The effect of R_m on the mean flow is shown through the axial velocity profiles in Fig. 6.10. These are obtained by performing both streamwise and time averaging. Interestingly, when $R_m = 400$, the mean velocity profile along the spanwise direction is significantly higher as compared to the quasistatic case, except in the region close to the center of the duct. However, along the wall normal direction, the effect of R_m on the mean velocity profile is not so significant in the Hartmann layers and near the centre of the duct, but the velocity is slightly lower at $R_m = 400$ in the region in between. In other words, along the spanwise (y -) direction, the velocity profile of $R_m = 400$ is much flatter than the quasistatic case, whereas it is the opposite trend along the wall-normal (z -) direction. That the effect on the mean flow is more significant in the spanwise direction is also confirmed by the profiles of u^+ with distance from the boundary in wall units (y^+ and z^+). Here, the distance in wall units is defined as

$$y^+ = (y + 1)Re_\tau, \quad z^+ = (z + 1)Re_\tau, \quad (6.8)$$

where, $Re_\tau = 0.5Re\sqrt{C_{f,Sh} + C_{f,Ha}}$ represents the wall-friction Reynolds number. The velocity u^+ is obtained by normalizing the mean velocity $\langle u \rangle_{x,t}$ by Re_τ/Re .

In all the cases, the results of LES show a very close agreement to our DNS results at $R_m = 0$. The reason for the higher mean velocity along $z = 0$ at $R_m = 400$ will be apparent from the Reynolds stress profile shown in Fig. 6.11. Here the primary Reynolds stress component $-\langle u'v' \rangle_{x,t}$ (streamwise and time averaged) is plotted along the spanwise direction. The mostly lower values of Reynolds stress in the case of $R_m = 400$ is clearly seen to lead to corresponding higher values of the mean axial velocity. A slight asymmetry about $y = 0$ can be observed for the $R_m = 400$ curve. Convergence to a fully symmetric curve requires an extremely long time averaging window, which was not possible to achieve due to constraints of computational resources.

The intensity of turbulence itself is seen to be systematically higher in the case of $R_m = 400$. The RMS profiles of the axial velocity fluctuations is shown in Fig. 6.12(a) and Fig. 6.12(b). In fact, the intensity is seen to be higher by a significant factor in the profile along the z -direction. This picture is very much consistent with the earlier observation from axial velocity contours of large scale turbulence being induced in the core region in the case of moderate R_m . However, for a small region near the edge of the Hartmann layer, the intensity is lower in the case of $R_m = 400$. The exact reason for this is yet unclear.

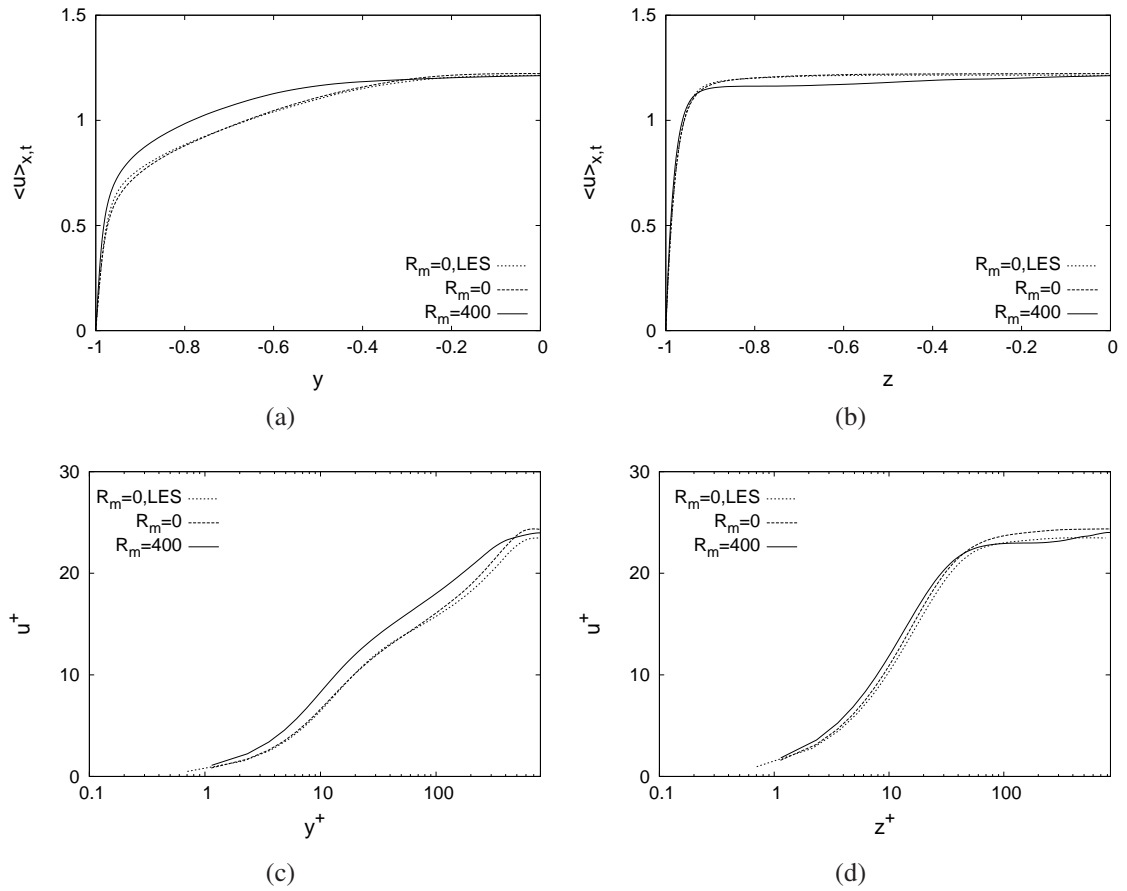


Figure 6.10: Mean velocity profiles along the a) spanwise direction at $z = 0$ and b) wall normal direction at $y = 0$. Mean velocity profiles in wall units along the c) spanwise direction at $z = 0$ and d) wall normal direction at $y = 0$. Common parameters are $Re = 14500$ and $Ha = 43.5$.

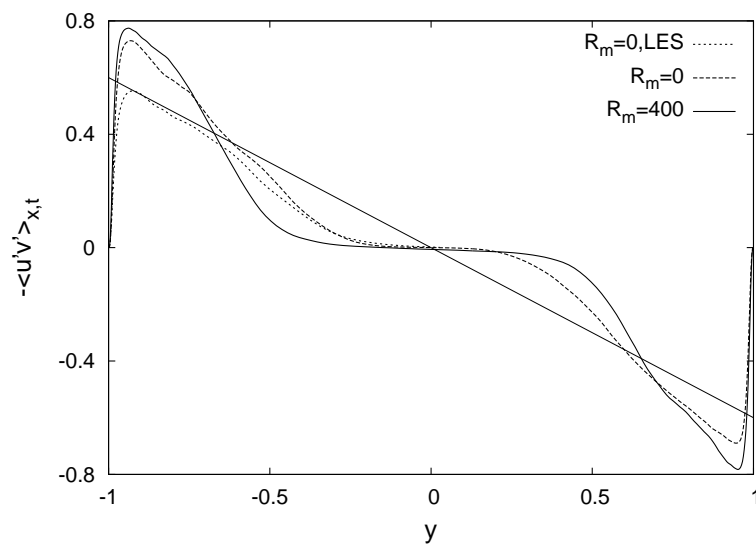


Figure 6.11: Profile of Reynolds stress component $-\langle u'v' \rangle_{x,t}$ along the spanwise direction at $z = 0$. Common parameters are $Re = 14500$ and $Ha = 43.5$.

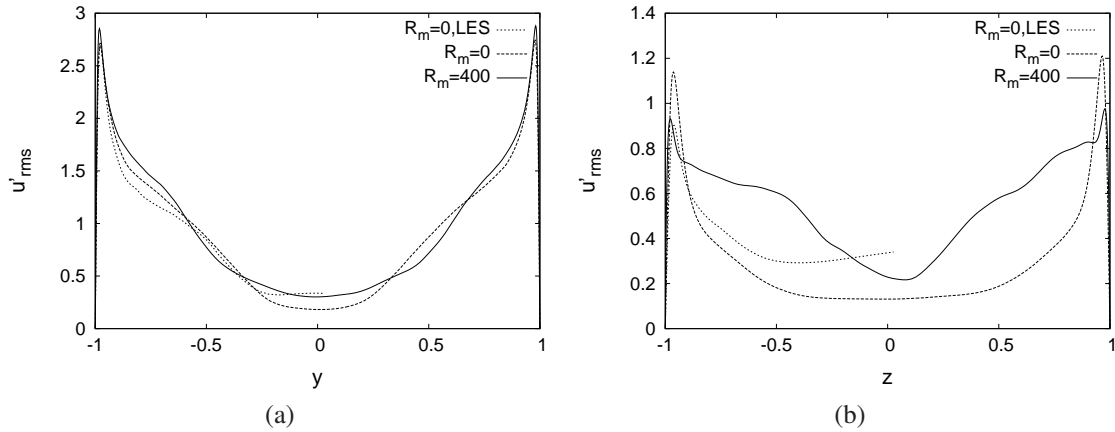


Figure 6.12: Profiles of streamwise turbulent fluctuation intensity a) along the spanwise direction at $z = 0$ and b) along the wall normal direction at $y = 0$. Common parameters are $Re = 14500$ and $Ha = 43.5$. Profiles that extend to only one half of the range of the horizontal scale are from Kobayashi [2008].

6.2.5 Anisotropy

We close this chapter with a brief look into the effect of R_m on the anisotropy of the turbulent flow. It is well known from quasistatic MHD that a magnetic field tends to diffuse vorticity along the field lines. This is because of the fact that Lorentz force decelerates only the velocity components perpendicular to the magnetic field and in addition, the magnitude of the force is proportional to the local velocity of the fluid. From studies of MHD turbulence at low R_m in periodic boxes, it has been shown that the joule dissipation of turbulent kinetic energy is given by $N|\hat{v}(\hat{k}, t)|^2 \cos^2 \theta$, where $\hat{v}(\hat{k}, t)$ is the Fourier coefficient of the velocity field for wavenumber vector \hat{k} and θ is the angle between \hat{k} and the applied magnetic field \mathbf{b}_0 (Schumann [1976]). This means that gradients of cross-field velocity components along the field lines decay and hence one would find that the vorticity does not tend to change along the field lines. This manifests as a source of anisotropy in the structure of turbulence and has been a parameter of key interest in the study of MHD turbulence. An extreme scenario of this aspect is the so-called two-dimensionality in MHD turbulence, wherein for a sufficiently strong magnetic field, the vorticity is seen to be completely aligned with the magnetic field lines (Moffatt [1967]). By anisotropy, here we mean in specific the structural anisotropy, that occurs as a consequence of differences in length scales with direction. Anisotropy itself is indeed not a new feature in turbulence, but has been a key ingredient of shear flows. It has been observed in the case of wall bounded flows such as in channels and ducts, that the flow exhibits long streaky structures that are elongated in the direction of mean flow. This is commonly known as anisotropy induced by mean shear. On the other hand, anisotropy induced by a uniform magnetic field and its relative magnitude (and effects) in the backdrop of mean shear induced

anisotropy, has been studied extensively in the case of Hartmann channel and duct flows at low R_m . Our aim here is to investigate, how anisotropy is affected by the presence of an actively evolving magnetic field (as is the case at moderate R_m) as compared to the quasistatic case.

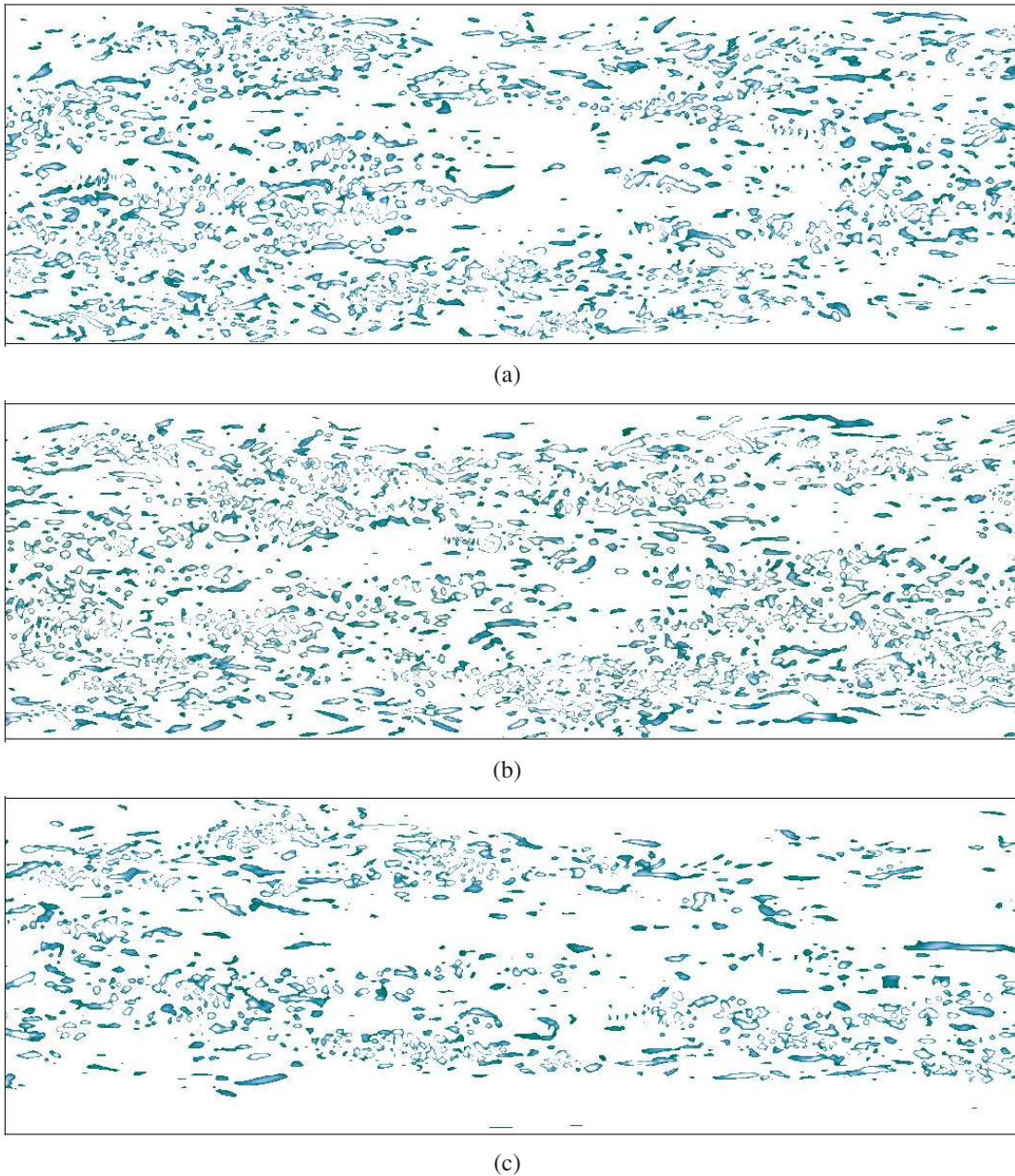


Figure 6.13: Contours of λ_2 in the $x-z$ plane. a) $R_m = 0$, b) $R_m = 400$ and c) $R_m = 2000$ at the spanwise location $y = -0.95$ which is close to the wall. Contour coloring: $\lambda_2 = -3$ (light end) and $\lambda_2 = -15$ (dark end). Common parameters are $Re = 14500$ and $Ha = 43.5$.

There are several measures of quantifying anisotropy in a turbulent flow. However, here we seek only a qualitative picture by looking at the instantaneous vortical structures in the flow.

This is shown in Fig. 6.13 by the contours of negative λ_2 at the plane $y = -0.95$, which is located close to and parallel to the side walls in the Shercliff layer. Here, λ_2 is the second largest eigen value of the tensor $\mathbf{S}^2 + \mathbf{\Omega}^2$, where the tensors \mathbf{S} and $\mathbf{\Omega}$ are defined as

$$S_{ij} = \frac{1}{2} \left(\frac{\partial u_i}{\partial x_j} + \frac{\partial u_j}{\partial x_i} \right), \quad \Omega_{ij} = \frac{1}{2} \left(\frac{\partial u_i}{\partial x_j} - \frac{\partial u_j}{\partial x_i} \right). \quad (6.9)$$

With increase in R_m , one can observe that the structures are only slightly more elongated in the streamwise direction without any clear indication of an increased dominance of mean shear induced anisotropy. Furthermore, at $R_m = 2000$, intense vortices become much rarer, especially in the near-wall region as can be observed from Fig. 6.13(c). Observations here can only be confirmed through quantitative measures of anisotropy which is currently being studied and is not reported here.

Chapter 7

Summary and Outlook

In this work, a coupled finite-difference/boundary element computational procedure was developed to enable direct numerical simulations of finite R_m phenomena in MHD duct flows. The method is a useful tool to perform direct numerical simulations of MHD turbulence with uniform magnetic fields as well as localized magnetic fields that have been of recent interest. The procedure was subsequently used to analyse three specific problems and a number of interesting results were obtained. A summary of the significant results and outcome of this work is as follows:

1. At first, it is shown that DNS of turbulent magnetohydrodynamic duct flows at moderate Re and R_m can be performed in a practical manner with the currently available resources. A coupled finite-difference/boundary element procedure is proposed for the magnetic induction equation and is implemented into a numerical code. The procedure is thoroughly verified in the limiting case of low R_m . Given the non-existence of standard solvers for a system of two Poisson equations and a Fredholm integral equation, the explicit scheme is found to be favourable in most cases, to perform DNS. The often used pseudo-vacuum magnetic boundary conditions were found to accurately describe the current density field \mathbf{j} in the limit of low R_m , although the magnetic fields show significant differences with those computed with the fully consistent boundary conditions. The results are published in Bandaru *et al.* [2016].
2. The transient response of Lorentz force in the case of a strongly accelerating conducting bar in the presence of a localized magnetic field was analysed. The Lorentz force shows a time lag as compared to the velocity and the rise time is seen to be a linear function of R_m , apart from showing a close agreement with the experiment. The peak Lorentz force as a function of R_m shows an asymptotic behavior near low values ($R_m \sim 1$) and an R_m^{-1} dependence for sufficiently high

values of R_m .

3. The phenomenon of dynamic runaway due to magnetic flux expulsion in a two-dimensional channel MHD flow was explored. The existence of two distinct regimes - the Hartmann and Poiseuille regimes that are separated by a bifurcation was confirmed. The existing one-dimensional analytical model is found to accurately describe the Hartmann regime and the location of the bifurcation but significantly overpredicts the core velocities in the Poiseuille regime, due to the neglect of non-linearity. The Poiseuille regime is seen to be strongly unsteady similar to that of travelling waves, but does not show spatial irregularity for the parameters explored here. The location of the bifurcation is found to be independent of the hydrodynamic and magnetic Reynolds numbers, but however is strongly affected by the wavenumber of the imposed magnetic field as lower streamwise wavenumber (κ) leads to bifurcation to the Poiseuille regime at much higher values of the inverse Stuart number Q and vice versa. In contrast to the model, the magnetic Reynolds number has a substantial effect on the U_c - Q curve (U_c is the core axial velocity), that is similar to the effect of the hydrodynamic Reynolds number. These results were published in Bandaru *et al.* [2015b].
4. At moderate magnetic Reynolds numbers and low hydrodynamic Reynolds numbers, turbulence in a Hartmann duct flow sustains until a higher Hartmann number without relaminarizing, as compared to the flow at low R_m (Bandaru *et al.* [2016]).
5. At moderate hydrodynamic and magnetic Reynolds numbers, large scale turbulence is induced at moderate R_m and the effect increases with R_m . Skin-friction coefficient due to the Hartmann walls show a systematical decrease with increase in R_m , whereas that due to the Shercliff walls remains roughly the same. Between the core and the Shercliff layers, Reynolds stresses decrease with increase in R_m , leading to larger mean velocities (and flatter velocity profiles) in that region.

There are several avenues for future research building upon the present work. The effect of moderate R_m on turbulence in the Hartmann duct flow can be better understood from the nature of energy exchange between the magnetic field and turbulence and the energy spectra. These and other studies are already in progress by the author and T. Boeck. Our present focus has been on fluids with relatively high magnetic Prandtl numbers $Pr_m \sim 10^{-2}$, as compared to typical liquid metals with $Pr_m \sim 10^{-6}$ that would correspond to a very high Re when R_m becomes finite. Modeling flows with realistic magnetic Prandtl numbers would be feasible with the use of large eddy simu-

lations (LES) that requires subgrid-scale turbulence modeling coupled with the boundary integral procedure. Furthermore, extending the numerical procedure to incorporate non-periodic inlet-outlet boundary conditions in the streamwise direction will be useful in enabling shorter duct lengths for DNS. The effect of an inhomogenous localized field on duct turbulence will also be of significant interest, as it is expected to show strong differences from the quasistatic case.

Related to the dynamic runaway studies in the channel flow, it is expected that transition to turbulence ensues when the flow bifurcates to the Poiseuille state. In our studies, two-dimensionality of the problem did not allow distinct chaotic states to manifest, and hence we observed only strongly transient states. Hence it is desirable to extend this study to a three-dimensional duct flow with magnetic field imposed from externally placed magnet systems, with full-consistent magnetic boundary conditions. Such a study is planned to be performed in the near future.

7. Summary and Outlook

Appendix A

Uniqueness of the current density field when $j_n = 0$

The current density field is observed to be independent of the exact form of the magnetic boundary conditions which satisfy $j_n = 0$, to which we provide a simple proof. Considering two numerical realizations of computing the secondary magnetic field \mathbf{b} from the QST formulation with a given velocity field \mathbf{v} , we denote the solutions obtained as \mathbf{b}_1 and \mathbf{b}_2 . As an example, one of the cases can correspond to the integral boundary conditions shown in this paper and the other case can correspond to the pseudo-vacuum boundary conditions. Both boundary conditions ensure that the wall normal current vanishes, $j_n = 0$. The difference between the two solutions is denoted by $\mathbf{d}_b = \mathbf{b}_2 - \mathbf{b}_1$. It follows from equation (3.59) that

$$\nabla^2 \mathbf{d}_b = 0 \quad \text{or} \quad \nabla(\nabla \cdot \mathbf{d}_b) - \nabla \times (\nabla \times \mathbf{d}_b) = 0. \quad (\text{A.1})$$

Since both the solutions \mathbf{b}_1 and \mathbf{b}_2 are solenoidal, $\nabla \times (\nabla \times \mathbf{d}_b) = 0$ and we can introduce a scalar potential ϕ as $\nabla \times \mathbf{d}_b = -\nabla \phi$. Taking the divergence, we obtain

$$\nabla^2 \phi = 0. \quad (\text{A.2})$$

Moreover, $\nabla \phi = -\nabla \times \mathbf{d}_b = -\nabla \times (\mathbf{b}_2 - \mathbf{b}_1) = \mathbf{j}_1 - \mathbf{j}_2$. Therefore, it follows that $\frac{\partial \phi}{\partial n} = j_{n1} - j_{n2} = 0$ on the boundary. Equation (A.2) with the Neumann condition gives $\phi = \text{constant}$ and hence $\mathbf{j}_1 = \mathbf{j}_2$. This explains why the solution for \mathbf{j} obtained from the pseudo-vacuum boundary conditions is in agreement with that obtained using the rigorous boundary integral procedure.

Appendix B

Effective wavenumbers for Fast Fourier transformation

The system considered here is periodic in the x -direction and hence FFT is applied in that direction. This enables efficient parallelization through the solution of the elliptic Poisson equations for velocity (\mathbf{v}), pressure (p) and the mean streamwise magnetic field (\bar{b}_x) using the Fishpack 2D solver. In addition, parallelization of the coupled BEM procedure with non-local boundary conditions becomes much easier without inter-processor communication. However, the streamwise derivatives computed in the Fourier space are not equivalent to the derivatives approximated using finite differences. Equivalence can be attained by the use of effective wavenumbers α_{k1} and α_{k2} that correspond to the first and second x -derivatives respectively as

$$\alpha_{k1} = \frac{\sin(\alpha\delta x)}{\delta x}, \quad \alpha_{k2} = \frac{\sin(\alpha\frac{1}{2}\delta x)}{\frac{1}{2}\delta x}. \quad (\text{B.1})$$

Ferziger & Perić [2002]. These relations are obtained by substituting the function $e^{i\alpha_k x}$ into the central finite-difference stencils for the first and second derivatives, respectively. It must be mentioned that in our procedure, α_{k1} is applied only in reconstructing the streamwise component \hat{b}_{xk} from \hat{b}_{yk} and \hat{b}_{zk} from the divergence-free condition using

$$\hat{b}_{xk} = \frac{-1}{i\alpha_{k1}} \left(\frac{\partial \hat{b}_{yk}}{\partial y} + \frac{\partial \hat{b}_{zk}}{\partial z} \right), \quad k \neq 0 \quad (\text{B.2})$$

and α_{k2} is used for the rest of the procedure.

Appendix C

Sensitivity of Lorentz force time response

The aim of this study is to ensure that the results of Lorentz force response obtained from the simulations of the accelerating bar problem are insensitive to the grid parameters and the chosen length l_x of the domain. Figure C.1(a) shows the transient response of the integral Lorentz force in the bar with various non-dimensional lengths considered.

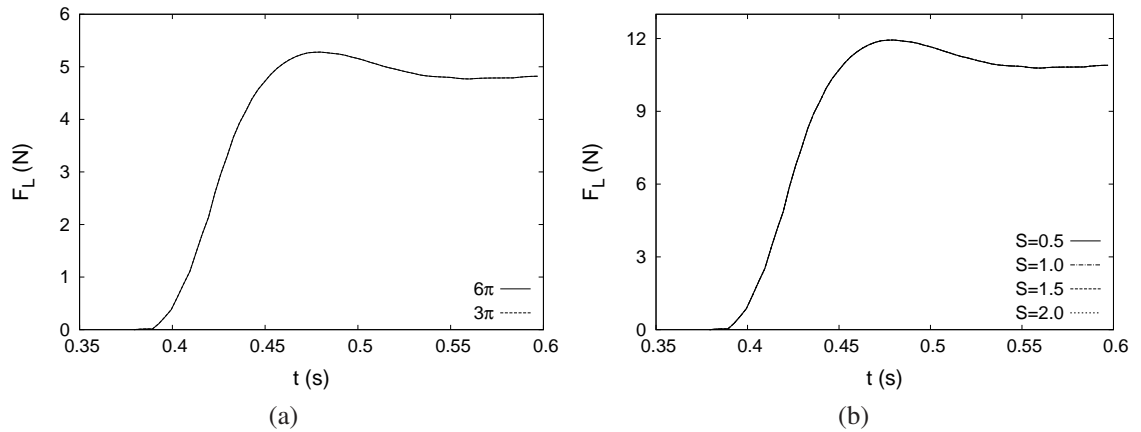


Figure C.1: Sensitivity of the Lorentz force response to the a) length of the bar l_x in the simulation. $l_x = 6\pi$ corresponds to the actual length of the rod in the experiment. b) grid stretch factor S .

The actual length of the bar in the experiment was $L_{x,exp} = 1$ m, which translates to a non-dimensional value of $l_{x,exp} = 18.8 \approx 6\pi$. It can be seen that already with a length $l_x = 2\pi$, convergent results are obtained and hence all the simulations are performed by modeling a length of 3π instead of the full length of the bar. This also justifies the usage of periodic boundary conditions in the streamwise direction. Furthermore, Figs. C.1(b), C.2(a) and C.2(b) show clearly that the grid size of 256×64^2 and grid stretch factor $S = 1.5$ that we use, provides sufficient resolution required for

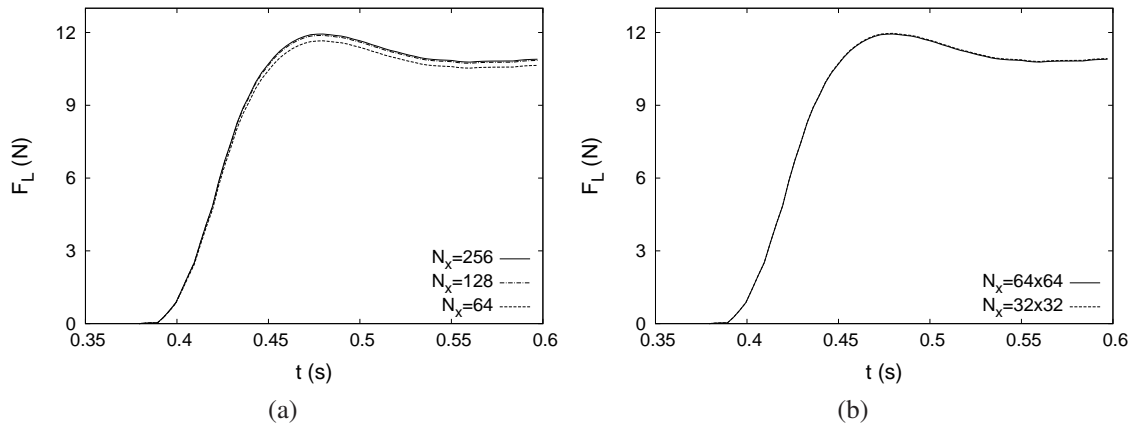


Figure C.2: Sensitivity of the Lorentz force response to the a) grid resolution in the x -direction (direction of motion) and b) grid resolution in the cross-section.

this problem.

Author Publications

BANDARU, V., BOECK, T., KRASNOV, D. & SCHUMACHER, J. 2016 A hybrid finite difference-boundary element procedure for the simulation of turbulent MHD duct flow at finite magnetic Reynolds number. *J. Comp. Phys.* **304**, 320–339.

BANDARU, V., KOLCHINSKAYA, A., PADBERG-GEHLE, K. & SCHUMACHER, J. 2015*a* Role of critical points of the skin friction field in formation of plumes in thermal convection. *Phys. Rev. E* **92**, 043006.

BANDARU, V., PRACHT, J., BOECK, T. & SCHUMACHER, J. 2015*b* Simulation of flux expulsion and associated dynamics in a two-dimensional magnetohydrodynamic channel flow. *Theor. Comput. Fluid Dyn.* **29**, 263–276.

REFERENCES

References

- ABRAMOWITZ, M. & STEGUN, I. 1964 *Handbook of Mathematical Functions*. Dover.
- ADAMS, J.C., SWARZTRAUBER, P. & SWEET, R. 1999 Efficient fortran subprograms for the solution of separable elliptic partial differential equations. <https://www2.cisl.ucar.edu/resources/legacy/fishpack>.
- ALFVÉN, H. 1942 Existence of electromagnetic-hydrodynamic waves. *Nature* **150**, 405–406.
- BATCHELOR, G.K. 1967 *An introduction to fluid dynamics*. Cambridge University Press.
- BOECK, T. 2010 Coherent structures, instabilities, and turbulence in interfacial and magnetohydrodynamic flows. Habilitation thesis, TU Ilmenau.
- BOECK, T., KRASNOV, D. & E., ZIENICKE 2007 Numerical study of turbulent magnetohydrodynamic channel flow. *J. Fluid. Mech.* **572**, 179–188.
- BOSSAVIT, A. 1991 The computation of eddy-currents, in dimension 3, by using mixed finite elements and boundary elements in association. *Math. Comput. Modelling* **15(3-5)**, 33–42.
- BOSSAVIT, A. & VÉRITÉ, J.C. 1982 A Mixed FEM-BIEM method to solve 3D eddy-current problems. *IEEE Trans. Mag.* **18(2)**, 431–436.
- BRANDENBURG, A., NORDLUND, A., STEIN, R.F. & TORKESSON, U. 1995 Dynamo generated turbulence and large scale magnetic fields in a Keplerian shear flow. *Astrophys. J.* **446**, 741–754.
- BREBBIA, C. & WALKER, S. 1978 *The Boundary Element Method for Engineers*. Pentech Press.
- BRONSHTEIN, I. N. & SEMENDYAYEV, K. A. 1997 *Handbook of Mathematics, 3rd ed.*. New York: Springer-Verlag.

REFERENCES

- BROULLIETTE, E.C. & LYKOURDIS, P.S. 1967 Magneto-fluid-mechanic channel flow. i. Experiment. *Phys. Fluids* **10**, 995–1001.
- CHAUDHARY, R., VANKA, S.P. & THOMAS, B.G. 2010 Direct numerical simulations of magnetic field effects on turbulent flow in a square duct. *Phys. Fluids* **22**, 075102.
- CHRISTENSEN, U.R., AUBERT, J., CARDIN, P., DORMY, E., GIBBONS, S., GLATZMAIER, G.A., GROTE, E., HONKURA, H., JONES, C., KONO, M., MATSUSHIMA, M., SAKURABA, A., TAKAHASHI, F., TILGNER, A., WICHT, J. & ZHANG, K. 2001 A numerical dynamo benchmark. *Phys. Earth Planet. Int.* **128**, 25–34.
- CHRISTIANSEN, S. 1971 Numerical solution of an integral equation with a logarithmic kernel. *BIT* **11**, 276–287.
- CRAWFORD, C.H. & KARNIADAKIS, G.E. 1997 Reynolds stress analysis of EMHD-controlled wall turbulence. Part 1. Streamwise forcing. *Phys. Fluids* **10(8)**, 788–806.
- DAVIDSON, P.A. 1999 Magnetohydrodynamics in materials processing. *Annu. Rev. Fluid Mech.* **31**, 273–300.
- DAVIDSON, P.A. 2001 *An introduction to Magnetohydrodynamics*. Cambridge University Press.
- FERZIGER, J.H. & PERIĆ, M. 2002 *Computational methods for fluid dynamics*. Springer.
- FURLANI, E.P. 2001 *Permanent magnets and Electromechanical devices*. Academic Press.
- GAILITIS, A., LIELAUSIS, O., PLATACIS, E., GERBETH, G. & STEFANI, F. 2004 Riga dynamo experiment and its theoretical background. *Phys. Plasmas* **11**, 2838–2843.
- GALLOWAY, D.J., PROCTOR, M.R.E. & WEISS, N.O. 1978 Magnetic flux ropes and convection. *J. Fluid Mech.* **87**, 243–261.
- GARDNER, R.A. & LYKOURDIS, P.S. 1971 Magneto-fluid-mechanic pipe flow in a transverse magnetic field. Part 1. Isothermal flow. *J. Fluid. Mech.* **47**, 737–764.
- GIESECKE, A., STEFANI, F. & GERBETH, G. 2008 Kinematic simulation of dynamo action by a hybrid boundary-element/finite-volume method. *Magnetohydrodynamics* **44**, 237–252.

- GIMBLETT, C.G. & PECKOVER, R.S. 1979 On the mutual interaction between rotation and magnetic fields for axisymmetric bodies. *Proc. R. Soc. Lond.* **A 368**, 75–97.
- GUERMOND, J.L., LAGUERRE, R., LÉORAT, J. & NORE, C. 2007 An interior penalty Galerkin method for the MHD equations in heterogeneous domains. *J. Comp. Phys.* **221**, 349–369.
- GUERMOND, J.L., LAGUERRE, R., LÉORAT, J. & NORE, C. 2009 Nonlinear magnetohydrodynamics in axisymmetric heterogeneous domains using a Fourier/finite element technique and an interior penalty method. *J. Comp. Phys.* **228**, 2739–2757.
- GUERMOND, J.L., LÉORAT, J. & NORE, C. 2003 A new Finite Element Method for magneto-dynamical problems: Two-dimensional results. *Eur. J. Mech. B/Fluids* **22**, 555–579.
- HAMBA, F. & TSUCHIYA, M. 2010 Cross-helicity dynamo effect in magnetohydrodynamic turbulent channel flow. *Phys. Plasmas* **17**, 012301.
- HARTMANN, J. & LAZARUS, F. 1937 Hg-dynamics II: experimental investigations on the flow of mercury in a homogeneous magnetic field. *K. Dan. Vidensk. Selsk. Mat.* **15 (7)**, 1–45.
- HEINICKE, C. 2013 Spatially resolved measurements in a liquid metal flow with lorentz force velocimetry. *Exp. Fluids* **54(6)**, 1–8.
- HERNÁNDEZ, D., SCHLEICHERT, J., KARCHER, C., FRÖHLICH, T., WONDRAK, T. & TIMMEL, K. 2015 Local lorentz force velocimetry using a multicomponent force and torque sensor. *Manuscript under consideration for Meas. Sci. Technol.* .
- HUBBARD, A. & BRANDENBURG, A. 2010 Magnetic helicity fluxes in an α^2 dynamo embedded in a halo. *Geophys. Astrophys. Fluid Dyn.* **104**, 577–590.
- HUNT, J.C.R. 1965 Magnetohydrodynamic flow in rectangular ducts. *J. Fluid. Mech.* **21**, 577–599.
- HURLBURT, N.E. & TOOMRE, J. 1988 Magnetic fields interacting with non-linear compressible convection. *Astrophys. J.* **327**, 920–932.
- ISKAKOV, A.B., DESCOMBES, S. & DORMY, E. 2004 An integro-differential formulation for magnetic induction in bounded domains: Boundary element - finite volume method. *J. Comp. Phys.* **197**, 540–554.

REFERENCES

- ISKAKOV, A. & DORMY, E. 2005 On magnetic boundary conditions for non-spectral dynamo simulations. *Geophy. Astrophy. Fluid Dyn.* **99-6**, 481–492.
- KAMKAR, H. & MOFFATT, H.K. 1982 A dynamic runaway effect associated with flux expulsion in magnetohydrodynamic channel flow. *J. Fluid Mech.* **90**, 107–122.
- KENJEREŠ, S. & HANJALIĆ, K. 2007 Numerical simulation of a turbulent magnetic dynamo. *Phys. Rev. Lett.* **98**, 104501.
- KENJEREŠ, S., HANJALIĆ, K. & RENAUDIER, S. 2006 Coupled fluid-flow and magnetic-field simulation of the Riga dynamo experiment. *Phys. Plasmas* **13**, 122308.
- KNAEPEN, B., KASSINOS, S. & CARATI, D. 2004 MHD turbulence at moderate magnetic Reynolds number. *J. Fluid Mech.* **513**, 199–220.
- KOBAYASHI, H. 2008 Large eddy simulation of magnetohydrodynamic turbulent duct flows. *Phys. Fluids* **20**, 015102.
- KRASNOV, D., THESS, A., BOECK, T., ZHAO, Y. & ZIKANOV, O. 2013 Patterned turbulence in liquid metal flow: Computational reconstruction of the Hartmann experiment. *Phys. Rev. Lett.* **110**, 084501.
- KRASNOV, D., ZIKANOV, O. & BOECK, T. 2011 Comparative study of finite difference approaches in simulation of magnetohydrodynamic turbulence at low magnetic Reynolds number. *Comp. Fluids* **50**, 46–59.
- KRASNOV, D., ZIKANOV, O., SCHUMACHER, J. & BOECK, T. 2008 Magnetohydrodynamic turbulence in a channel with spanwise magnetic field. *Phys. Fluids* **20**, 095105.
- LANGLOIS, W.E. 1985 Buoyancy-driven flows in crystal-growth melts. *Annu. Rev. Fluid Mech.* **17**, 191–215.
- LARMOR, J. 1919 How could a rotating body such as the sun become a magnet ? *Rep. Brit. Assoc. Adv. Sci.* pp. 159–160.
- LEE, D. & CHOI, H. 2001 Magnetohydrodynamic turbulent flow in a channel at low magnetic Reynolds number. *J. Fluid. Mech.* **439**, 367–394.
- LIM, J., CHOI, H. & KIM, J. 1998 Control of streamwise vortices with uniform magnetic fluxes. *Phys. Fluids* **9**, 1997–2005.

- MEIR, A.J. & SCHMIDT, P.G. 1994 A velocity current formulation for stationary MHD flow. *Appl. Math. Comput.* **65(1-3)**, 95–109.
- MEIR, A.J. & SCHMIDT, P.G. 1996 Variational methods for stationary MHD flow under natural interface conditions. *Nonlinear Anal.* **26(4)**, 659–689.
- MEIR, A.J. & SCHMIDT, P.G. 1999 Analysis and numerical approximation of a stationary MHD flow problem with non-ideal boundary. *SIAM J. Numer. Anal.* **36(4)**, 1304–1332.
- MOFFATT, H.K. 1967 On the suppression of turbulence by a uniform magnetic field. *J. Fluid Mech.* **28**, 571–592.
- MOFFATT, H.K. 1980 Rotation of a liquid metal under the action of a rotating magnetic field. *MHD Flows and Turbulence (ed. H. Branover A. Yakhot)*, Israel Universities Press. pp. 45–62.
- MÜLLER, U. & BÜLLER, L. 2001 *Magnetohydrodynamics in channels and containers..* Springer.
- MURGATROYD, W. 1953 Experiments on magnetohydrodynamic channel flow. *Phil. Mag.* **44**, 1348–1354.
- NORE, C., LÉORAT, J., GUERMOND, J.L. & LUDDENS, F. 2011 Nonlinear dynamo action in a precessing cylindrical container. *Phys. Rev. E* **84**, 016317.
- OUGHTON, S., PRIEST, E.R. & MATTHAEUS, W.H. 1994 The influence of a mean magnetic field on three-dimensional magnetohydrodynamic turbulence. *J. Fluid Mech.* **280**, 95–117.
- PARKER, E.N. 1963 Kinematical hydromagnetic theory and its applications to the low solar photosphere. *Astrophys. J.* **138**, 552–575.
- PARKER, R.L. 1966 Reconnexion of lines of force in rotating spheres and cylinders. *Proc. R. Soc. Lond.* **291**, 60–72.
- PRIDE, J., BUCHENAU, D. & GERBETH, G. 2011 Single-magnet rotary flow meter for liquid metals. *J. Appl. Phys.* **110(3)**, 034512.
- PROCTOR, M.R.E. & GALLOWAY, D.J. 1979 The dynamic effect of flux ropes on Rayleigh-Bénard convection. *J. Fluid Mech.* **90**, 273–287.

REFERENCES

- RÄDLER, K.-H., APSTEIN, E., RHEINHARDT, M. & SCHÜLER, M. 1998 The Karlsruhe dynamo experiment - a mean-field approach. *Stud. Geophys. Geod.* **42**, 224–231.
- RÄDLER, K.-H., RHEINHARDT, M., APSTEIN, E. & FUCHS, H. 2002 On the mean-field theory of the Karlsruhe dynamo experiment. *Nonl. Proc. Geophys.* **9**, 171–178.
- REED, C.B. & LYKOURIS, P.S. 1978 The effect of a transverse magnetic field on shear turbulence. *J. Fluid. Mech.* **89**, 147–171.
- RITCHIE, W. 1832 Experimental research in voltaic electricity and electro-magnetism. *Phil. Trans. R. Soc. Lond.* **122**, 279–298.
- ROBERTS, P.H. 1967 *An Introduction to Magnetohydrodynamics*. New York: Elsevier.
- RÜDIGER, G. & ZHANG, Y. 2001 MHD instability in differentially-rotating cylindrical flows. *Astron. Astrophys.* **378**, 302–308.
- SCHMIDT, PAUL G. 1999 A Galerkin method for time-dependent MHD flow with non-ideal boundaries. *Commun. Appl. Anal.* **3(3)**, 383–398.
- SCHUMANN, U. 1976 Numerical simulation of the transition from three- to two-dimensional turbulence under a uniform magnetic field. *J. Fluid Mech.* **74**, 31–58.
- SHATROV, V. & GERBETH, G. 2010 Marginal turbulent magnetohydrodynamic flow in a square duct. *Phys. Fluids* **22**, 084101.
- SHERCLIFF, J.A. 1965 *A textbook of Magnetohydrodynamics*. Pergamon Press.
- SHERCLIFF, J. A. 1953 Steady motion of conducting fluids in pipes under transverse magnetic fields. *Mathematical Proceedings of the Cambridge Philosophical Society* **49**, 136–144.
- SMOLENTSEV, S., CUEVAS, S. & BELTRÁN, A. 2010 Induced electric current based formulation in computations of low magnetic Reynolds number magnetohydrodynamic flows. *J. Comput. Phys.* **229**, 1558–1572.
- SOKOLOV, I., KOLESNIKOV, Y. & THESS, A. 2014 Experimental investigation of the transient phase of the Lorentz force response to the time-dependent velocity at finite magnetic Reynolds number. *Meas. Sci. Technol.* **25** (12), 125304.
- STAKGOLD, I. 2000 *Boundary Value Problems of Mathematical Physics, Vol.2*. SIAM, Philadelphia.

- STEFANI, F., GERBETH, G. & GAILITIS, A. 1999 Velocity profile optimization for the Riga dynamo experiment, in transfer phenomena in magnetohydrodynamic and electroconducting flows, edited by A. Alemany, Ph. Marty and J.-P. Thibault. *Kluwer: Dordrecht* **13**, 31–44.
- STEFANI, F., GERBETH, G. & RÄDLER, K.-H. 2000 Steady dynamos in finite domains: An integral equation approach. *Astron. Nachr.* **321**, 65–73.
- STEFANI, F., GUNDRUM, T. & GERBETH, G. 2004 Contactless inductive flow tomography. *Phys. Rev. E* **70**, 056306.
- STEFANI, F., XU, M., GERBETH, G. & WONDRAK, T. 2013 Integral equations in MHD: Theory and application. *Geophys. Astrophys. Fluid Dyn.* **107**, 58–72.
- SWEET, P.A. 1956 *Proceedings of the International Astronomical Union Symposium on Electromagnetic phenomena in Cosmical physics, Stockholm* .
- THESS, A., VOTYAKOV, E.V. & KOLESNIKOV, Y. 2006 Lorentz force velocimetry. *Phys. Rev. Lett.* **96**, 164501.
- TÓTH, G. 2000 The $\nabla \cdot B = 0$ constraint in shock-capturing magnetohydrodynamics codes. *J. Comp. Phys.* **161**, 605–652.
- WEISS, N.O. 1966 The expulsion of magnetic flux by eddies. *Proc. R. Soc. Lond.* **A293**, 310–328.
- WILLIAMS, W.E. 1963 Magnetohydrodynamic flow in a rectangular tube at high Hartmann number. *J. Fluid. Mech.* **16**, 262–268.
- XU, M., STEFANI, F. & GERBETH, G. 2004 Integral equation approach to time-dependent kinematic dynamos in finite domains. *Phys. Rev. E* **70**, 056305.
- XU, M., STEFANI, F. & GERBETH, G. 2008 The integral equation approach to kinematic dynamo theory and its application to dynamo experiments in cylindrical geometry. *J. Comp. Phys.* **227**, 8130–8144.

Erklärung

Ich versichere, dass ich die vorliegende Arbeit ohne unzulässige Hilfe Dritter und ohne Benutzung anderer als der angegebenen Hilfsmittel angefertigt habe. Die aus anderen Quellen direkt oder indirekt übernommenen Daten und Konzepte sind unter Angabe der Quelle gekennzeichnet. Bei der Auswahl und Auswertung folgenden Materials haben mir die nachstehend aufgeführten Personen in der jeweils beschriebenen Weise unentgeltlich geholfen:

1. Die fachliche Betreuung der Arbeit erfolgte durch Priv.-Doz. Dr. Thomas Boeck und Prof. Dr. Jörg Schumacher.
2. Experimentelle Daten aus Kapitel 4 zum Vergleich mit eigenen Berechnungen habe ich von Igor Sokolov (TU Ilmenau) erhalten.
3. Einige Datenpunkte in den Abbildungen 5.12, 5.13 und 5.14 aus Kapitel 5 wurden von Herrn Julian Pracht (TU Ilmenau) im Rahmen seiner Masterarbeit berechnet.
4. LES Daten aus Kapitel 6 zum Vergleich mit eigenen Berechnungen habe ich von Dr. Hiromichi Kobayashi (Keio University, Japan) erhalten.

Weitere Personen waren an der inhaltlich-materiellen Erstellung der vorliegenden Arbeit nicht beteiligt. Insbesondere habe ich hierfür nicht die entgeltliche Hilfe von Vermittlungs bzw. Beratungsdiensten (Promotionsberater oder anderer Personen) in Anspruch genommen. Niemand hat von mir unmittelbar oder mittelbar geldwerte Leistungen für Arbeiten erhalten, die im Zusammenhang mit dem Inhalt der vorgelegten Dissertation stehen. Die Arbeit wurde bisher weder im In- noch im Ausland in gleicher oder ähnlicher Form einer Prüfungsbehörde vorgelegt. Ich bin darauf hingewiesen worden, dass die Unrichtigkeit der vorstehenden Erklärung als Täuschungsversuch bewertet wird und gemäß §7 Abs.10 der Promotionsordnung den Abbruch des Promotionsverfahrens zur Folge hat.

Acknowledgments

I am grateful to my supervisors Dr. Thomas Boeck and Prof. Jörg Schumacher for the support and advice extended by them during the course of this work at TU Ilmenau. I thoroughly enjoyed working with them and have learnt a lot from them about the fascinating subjects of magnetohydrodynamics and turbulence during this time. Thomas has been very friendly and approachable throughout, which I liked very much. Jörg's timely advice and kind encouragement was extremely beneficial. Especially his willingness to teach turbulence lectures partly in english is highly appreciated. I would also like to thank Dr. Dmitry Krasnov for the various interesting discussions and suggestions on the computational aspects of fluid dynamics. Fruitful discussions with Dr. André Giesecke from Helmholtz-Zentrum Dresden-Rossendorf (HZDR) are also gratefully acknowledged. I also thank Prof. Bernard Knaepen for hosting me at the Institute of Plasma Physics, University of Brussels and offering useful advice on my work.

Furthermore, I also like to thank my colleagues in the Institute for Thermodynamics and Fluid mechanics at TU Ilmenau for a very friendly working atmosphere. In particular, I wish to thank Dr. Mohammed Emran, Paul Götzfried, Natalia Dubovikova, Mikhail Ovsyannikov and Prof. Yuri Kolesnikov for their caring advice.

This work was funded by the Deutsche Forschungsgemeinschaft (DFG), Germany within the Research Training Group 1567. Computer resources were provided by the computing center of TU Ilmenau and by the Jülich Supercomputing Center (JSC), Germany.